OUKA
The University of Osaka
Institutional Knowledge Archive

Title	Developing DNA origami-based experimental systems for structural and functional analyses of super-complexes
Author(s)	福本, 紘大
Citation	大阪大学, 2023, 博士論文
Version Type	VoR
URL	https://doi.org/10.18910/92184
rights	
Note	

The University of Osaka Institutional Knowledge Archive : OUKA

https://ir.library.osaka-u.ac.jp/

The University of Osaka

Doctoral Thesis

Developing DNA origami-based experimental systems for structural and functional analyses of super-complexes

Kodai Fukumoto

Department of Biological Sciences
Graduate School of Science
Osaka University

February 2023

Contents

Abbreviations **3**

Abstract **4**

General Introduction **6**

Part I. Improvement of DON–POI assembly and analysis of collective motility **10**

I-1. Introduction 10

I-2. Materials and Methods 12

I-3. Results 22

I-4. Discussion 61

Part II. DON-based purification system for cryo-EM analysis **71**

II-1. Introduction 71

II-2. Materials and Methods 72

II-3. Results 79

II-4. Discussion 104

General Discussion and Conclusions **107**

Acknowledgements **109**

References **110**

Supplementary Tables **118**

Abbreviations

A647, Alexa Fluor 647
ATP, adenosine triphosphate
BG, O^6-benzylgianine
CBB, Coomassie Brilliant Blue
CH, chlorohexane
cryo-EM, cryo-electron microscopy
CDF, cumulative distribution function
Cy3, Cyanine 3
Cy5, Cyanine 5
DNA, deoxyribonucleic acid
DON, DNA origami nanostructure
E. coli, *Escherichia coli*
EDTA, ethylenediaminetetraacetic acid
EMSA, electrophoretic mobility shift assay
dB, dual biotin
FSC, Fourier shell correlation
HB, helix bundle
LB, Luria-Bertani
MT, microtubule
NHS, N-Hydroxysuccinimide
PAGE, polyacrylamide gel electrophoresis
PCR, polymerase chain reaction
PEG, polyethylene glycol
PF, protofilament
pI, isoelectric point
PIPES, piperazine-N,N'-bis(2-ethanesulfonic acid)
POI(s), protein(s) of interest
PDB, Protein Data Bank
ROI, region of interest
RT, room temperature
SA, streptavidin
SDG, sucrose density gradient
SDS, sodium dodecyl sulfate
SPA, single-particle analysis
ssDNA, single-stranded DNA
TIRF, total internal reflection fluorescence
TBE, Tris-Borate-EDTA
Tris, tris(hydroxymethyl)aminomethane
UV, ultraviolet

Abstract

Higher-order protein complexes play important roles in regulating a wide variety of biological reactions in cells. These super-complexes are 5–100 nm in size and show structural and functional heterogeneity. Despite their importance, performing structural and functional analyses of these complexes remains challenging owing to a lack of technology suitable for evaluating mesoscale heterogeneous samples. Thus, technology to obtain homogeneous target samples has been sought. DNA origami nanotechnology is a versatile method which create mesoscale scaffolds, allowing the integration of bio-molecules in a spatially well-defined manner, enabling the capture and reconstruction of mesoscale super-complexes. In particular, DNA origami nanostructures (DONs) can be used as tools to evaluate the effects of the spatial layouts (e.g., intermolecular distances) of proteins of interest (POIs). Despite the advantage of DONs, their application to structural and functional analyses is still developing, and several technical challenges remain. In this thesis, experimental systems used to examine the structures and functions of POIs integrated on a DON are established.

Specific analysis of DON–POI complexes is performed after POI assembly onto a DON and purification of the complexes. Both unreacted free POIs and incomplete complexes that partially lack POIs blur the interpretation of the experimental data, requiring homogenous and well-purified samples. Efficient assembly of POI onto a DON helps the entire and homogeneous formation of desired complexes and can reduce unwanted effects of free unincorporated POIs. Here, positively charged peptide sequence fused to self-ligating tag proteins, such as $SNAP_f$-tag and HaloTag, is proposed to accelerate the speed of assembly of a model protein, kinesin, on a DON. Due to the improvement in assembly speed, the complexes were achieved with a high yield and less excess POI. For a biological aspect of kinesin motor protein, whether the layout of kinesins on a cargo affects the motile function, and if so, in what manner, is elusive.

Therefore, the effect of kinesin layout on a DON was evaluated. Single-molecule imaging data showed that spatial proximity of kinesins decreased their processivity, whereas the two-dimensional arrangement of kinesins with similar densities had little effect on their motility. These results shows that the experimental system provides a framework to study the effect of motor layout on collective motility.

Structural analysis using cryo-electron microscopy (cryo-EM) is also a powerful platform to determine the architectures of super-complexes and to understand their functions from a molecular level; however, this method is limited by the time-consuming procedure of the purification of individual components and by difficulty in reconstructing complexes of interest. DONs can provide ideal carriers to capture and purify POIs via a multivalent-affinity interaction using defined layouts of multiple binder modules. However, DON-based purification of native POIs from cell lysates and high-resolution structural analyses of these purified POIs have not yet been reported. In this study, a DON carrier was used to capture a model macromolecule, the ribosome, in bacterial lysate using avidin-biotin interactions. The DON–POI complexes were separated from other components in the cell lysate via sucrose density gradient centrifugation. Cryo-EM single-particle analysis successfully reconstructed three-dimensional structures of the 70S ribosome, showing a possible application of DONs as carriers in POI purification. These studies highlight a potential of DNA origami nanotechnology for structural and functional analyses of higher-order protein complexes.

General Introduction

Mesoscale Biology

Protein is one of the major components of cells. Higher-order protein assembly enables accurate and complicated regulation of biological reactions, such as gene expression, intracellular metabolism, cargo transport and intercellular interaction (Ally et al., 2009; Goodsell et al., 2020; Wilson and Gitai, 2013; Wolberger, 2021). These protein complexes are formed over the range of 5−100 nm, which qualifies as mesoscale. Structural and functional analyses of protein complexes are important to elucidate the molecular mechanism underlying their functions. However, research in this field is characterized by some technological challenges. For instance, when performing structural analysis studies, the diffraction limit of a classical optical microscope blurs images of the structures. Structural analyses based on nuclear magnetic resonance or X-ray crystallography are also challenging for huge and heterogeneous structures. Functional analysis is also hindered by the heterogeneity of protein complexes and lack of an experimental system to analyze the functions of individual molecules inside the complexes. Because of these limitations, examining mesoscale biological reactions has been exceedingly difficult.

For structural analysis, electron microscopy (EM) is a powerful tool used to visualize biological structures. Resent advancements in cryo-EM (Schultz, 1988) and electron cryotomography (Gan and Jensen, 2012) have enabled structural determination with a very high, sometimes atomic, resolution. For other approaches, intermolecular interactions and complex structures can be analyzed by several methods based on the reactions of proximal molecules, such as biotin identification (Roux et al., 2012) and Hi-C (Lieberman-Aiden et al., 2009). Biotin identification provides information corresponding to protein–protein interactions

using promiscuous biotin ligase fused to a POI, but it cannot show detailed distances and structures. Hi-C, on which nuclear DNA is digested, ligated, and sequenced to determine chromatin conformation, is based on next-generation sequencing and is mostly limited to DNA analysis. For the functional analysis of complexes and the individual molecules composing complexes, super-resolution microscopy enables the specific imaging of POIs using a genetically-labeled fluorescence-tag approach. Nonetheless, there is a trade-off between the spatial- and temporal resolutions, and thus the dynamics of mesoscale reactions have been remained elusive. Moreover, all of these technologies are a "measurement" approach, where the native structure and function are measured by specific methods. A "manipulation" approach, where the effects of system perturbation are examined by manipulating certain key factors of the system, is much more difficult to perform. In addition to classical genetical and biochemical approaches, systems to manipulate mesoscale biological structures can help understand molecular mechanisms underlying complicated biological functions.

DNA origami nanotechnology

DNA nanotechnology is an approach that can operate on mesoscale structures. This technology was pioneered by Nadrian C. Seeman (1982) in order to support POI crystallization (Seeman, 1982). Self-assembly of DNA molecules forms huge DNA nanostructures, and POIs are integrated through the modified DNA molecules incorporated in these nanostructures (Seeman, 2003). DNA origami is a versatile method developed by Paul W. K. Rothemund (2006), enabling the accurate structural design of DNA nanostructures (Rothemund, 2006). In this method, a single-stranded DNA (ssDNA) scaffold with approximately 8,000 nucleotides is folded with hundreds of oligonucleotides, each with 20–70 nucleotides called staples. This nanotechnology allows the formation of complicated 3D structures with a high thermal strength

(Castro et al., 2011). Importantly, arbitrary binder modules, such as ssDNA and biotin, can be located on surfaces of DONs through modified staples with a spatially-defined manner. This allows the assembly of POIs at specific sites on DONs through oligonucleotide hybridization (Niemeyer, 2010), biotin-avidin interaction (Yan et al., 2003), and binding between a tag-protein and its ligand (Saccà et al., 2010).

Due to these properties, DNA origami and other DNA nanotechnologies have been used to evaluate biological processes. One interesting application is the analysis of an enzyme cascade reaction, where multiple POIs corresponding to a particular cascade reaction are incorporated on the same DNA scaffold (Fu et al., 2012; Klein et al., 2019; Wilner et al., 2009). In the experimental system, the effect of intermolecular distance between POIs has been elucidated (Fu et al., 2012). DONs are also used as a scaffold to reconstruct desired oligomeric complexes, such as motile complexes incorporated with motor proteins (Abdellatef et al., 2022; Derr et al., 2012; Hariadi et al., 2015, 2016; Ibusuki et al., 2020; Krementsova et al., 2017; Matsuda et al., 2019). Moreover, DONs with multiple types of aptamers have been used to capture POIs with multi-affinity, and to evaluate the suitable intermolecular distance between binder modules (Rinker et al., 2008). These studies support the idea that DNA origami is an ideal scaffold for POI integration, with a defined layout and the ability to reconstitute mesoscale super-complexes to analyze biological structures and/or functions.

Goal of this thesis

Despite these advancements in recent years, the application of DNA origami nanotechnology to structural and functional analyses of mesoscale biological issues is still developing, and several technical challenges have remained. In this thesis, experimental systems to address these technical problems are introduced, enabling the structural and functional analyses of POIs. In

part I, a major challenge for using DONs, the low yield of DON–POI complexes, is overcome by introducing a new peptide sequence. The established POI-assembly system is applied to the functional analysis of a motor protein and then evaluated to establish how the intermolecular layout of motor proteins affects the motility. In part II, an experimental system to capture a POI in a bacterial lysate via a DON carrier. The experimental platform allows the purification of POIs from cell lysate using a DON and cryo-EM observation. From these results, a potential of DNA origami nanotechnology for structural and functional analyses of mesoscale biological issues is proposed.

Part I. Improvement of DON−POI assembly and analysis of collective motility

I-1. Introduction

DONs provide ideal scaffolds to evaluate the effects of POI assembly and the intermolecular layouts of POIs. Specific analysis of DON-integrated POIs requires efficient assembly and purification of DON–POI complexes. Most methods for functional analysis of POIs, including biochemistry and classical fluorescent imaging, does not have enough spatial resolution to distinguish the complexes of interest from other elements, such as free unreacted POIs and incomplete complexes that partially lack POIs at some of the designed binding sites, thereby reinforcing the importance of homogeneous purified samples. The efficient integration of POIs on DONs can reduce the POI required for assembly, and can increase yields of completely-integrated complexes (Nguyen et al., 2017; Saccà et al., 2010), reducing the effect of unreacted POIs and incomplete complexes. Therefore, efficiency of POI assembly is critical to understanding the functions of DON-integrated POIs. A major approach for POI assembly is the oligonucleotide hybridization method, where ssDNA-conjugated POIs are hybridized to ssDNA handles protruding from DONs (Niemeyer, 2010). Nonetheless, short hybridization reduces the yield of POI-integrated DONs, whereas long hybridization makes the precise evaluation of the intermolecular distance challenging, especially for short distances. In addition, the activity of POIs could be affected by chemical modification with a ssDNA handle. Another method is avidin–biotin interaction (Yan et al., 2003); however, POI–DON complexes could be dissociated during purification, decreasing the final yield of complete POI–DON complexes, particularly for multiple POI integration. On the other hand, direct binding between self-ligating tag proteins (such as SNAP-tag) and ligand-attached DONs ensures covalent binding of POIs onto DONs

with minimal blurring effects (e.g., the size of SNAP-tag is only 2-3 nm and smaller than the bulky dsDNA linker of hybridization method) (Kröll et al., 2022; Saccà et al., 2010). Despite the advantage of the direct attachment method, the low yield of the integration is an obstacle, chiefly in negatively charged proteins (Saccà et al., 2010). This reduced integration may be due to electric repulsion between negatively charged surfaces of DONs and POIs. The importance of electric charge is supported by studies by Niemeyer's group; SNAP-tagged POIs [isoelectric point (pI), 6.0] can be assembled with a high yield than POIs with a negatively charged HaloTag (pI, 4.9) (Saccà et al., 2010); replacement to positively charged amino acid residues in self-ligating tag proteins increased the yields of DON–POI complexes (Koßmann et al., 2016; Kröll et al., 2021).

In this chapter, the use of conventional kinesin (kinesin-1, thereafter kinesin) as a model protein, to explore a novel peptide tag to improve POI assembly onto DONs, is described. Kinesin is a negatively charged motor protein that moves along microtubule cytoskeletal trucks and plays an important role in intracellular cargo transport in eukaryotic cells (Hirokawa et al., 2010; Vale, 2003). Many of intracellular cargos are transported by teams of motor proteins (Hendricks et al., 2010; Shubeita et al., 2008; Welte et al., 1998). These transport complexes have been mimicked using DONs as scaffolds for motor assembly and evaluated to understand the roles of the number (Derr et al., 2012; Torisawa et al., 2014), intermolecular spacing (Ibusuki et al., 2020) of motors, and linker stiffness (Hariadi et al., 2015) on collective motility. However, the low efficiency of the motor assembly onto DONs causes difficulty in controlling the accurate stoichiometry of integrated motors (Miyazono, 2017). This technical challenge results in heterogeneity in motor numbers, which also influences motility, blurring interpretations of the experimental data. Thus, it is difficult to ascertain whether the layout of the exact number of motors affects the motility.

Here, the limitation was overcome by developing a positively charged peptide sequence fused to self-ligating tag proteins. This study shows that the peptide sequence accelerated the assembly of POIs onto a rod-shaped DON. In later sections of this part, I show single-molecule imaging experiments using DON-based transport complexes, along with the evaluation of the effects of kinesin layouts on collective motility, are presented.

I-2. Materials and Methods

Materials

Plasmids containing a cysteine-light human ubiquitous kinesin-1, $SNAP_f$-tag or HaloTag were provided by Prof. Hisashi Tadakuma (Miyazono et al., 2010). Constructs with 493 and 351 residues of kinesin-1 were used as a dimeric and monomeric proteins, respectively. Axonemes were prepared using high-salt wash method (kindly gift of Prof. Hisashi Tadakuma; Miyazono et al., 2010).

DNA cloning

Poly-lysine was introduced by polymerase chain reaction (PCR; KOD Plus NEO, TOYOBO) using primers listed in Supplementary Table 1. The generated fragments were digested by BamH I and Xho I (Takara) and inserted into the original plasmids. The constructed plasmids were transformed into DH5α (TOYOBO). Clones were selected by colony PCR (Ex Taq polymerase, Takara). The selected clones were cultured in Luria-Bertani (LB) medium and the plasmids were prepared using QIAprep Spin Miniprep Kit (QIAGEN). The sequences were confirmed by restriction digestion and DNA sequencing (Supplementary Table 2).

Protein purification and labeling

Proteins were expressed at 18°C and purified by Ni-NTA chromatography (QIAGEN), as previously described (Miyazono et al., 2010), and by ion exchange chromatography (Cytiva) with some modifications. Briefly, dimeric proteins were purified using HiTrap-Q with buffer (200) [200 mM NaCl with 25 mM piperazine-N,N'-bis(2-ethanesulfonic acid) (PIPES), pH 6.8, 2 mM $MgCl_2$, 1 mM EGTA, 100 μM ATP, 500 μM DTT; the numbers in parentheses show the NaCl concentration] for diluting and washing and eluted at ~0.45 M NaCl. Monomeric kinesin-$SNAP_f$-0K was purified using HiTrap-SP with buffer (100) for diluting and washing and eluted at ~0.25 M NaCl. Monomeric kinesin-$SNAP_f$-10K was purified using HiTrap-SP with buffer (150) for diluting and buffer (200) for washing and eluted at ~0.5 M NaCl. After purification, proteins were dialyzed against buffer C (25 mM PIPES, pH 7.0, 250 mM NaCl, 1 mM EGTA, 2 mM $MgCl_2$, and 50 μM ATP).

For binding assays, the dialyzed proteins were fluorescently labeled for 60 min at 4°C with Cy3-NHS (Cytiva) at a kinesin subunit/dye molar ratio of 1:10. For transport assays, the dialyzed dimeric kinesin-$SNAP_f$-10K was reacted for 160 min at 4°C with SNAP-Surface Alexa Fluor 647 (New England Biolabs) at a $SNAP_f$/O^6-benzylgianine (BG) molar ratio of 4:3 (partially labeled), or kinesin-$SNAP_f$-10K monomer was reacted for 60 min at 4°C with Cy5-NHS (Cytiva) at an $SNAP_f$/NHS molar ratio of 1:8. The unreacted dyes were removed by His SpinTrap (Cytiva) and the eluted proteins were dialyzed against buffer C. The protein concentration was determined by Bradford assays or sodium dodecyl sulfate (SDS)-polyacrylamide gel electrophoresis (PAGE) with Coomassie Brilliant Blue (CBB; Takara) using BSA as a standard. Cy3 concentration was determined by measuring absorbance using the molar extinction coefficient of Cy3 at 550 nm (150,000 M^{-1} cm^{-1}). After the addition of 10% sucrose, the dialyzed proteins were frozen in liquid nitrogen and stored at −80°C.

Conjugation of ligands to oligonucleotide

Amino-modified oligonucleotides were purchased from Integrated DNA Technologies. Conjugation of ligands for $SNAP_f$-tag and HaloTag was performed as previously described (Masubuchi et al., 2018). Briefly, the amino-modified oligonucleotides were incubated with BG-GLA-NHS (New England Biolabs) or HaloTag Succinimidyl Ester (O4) Ligand (Promega). Unreacted reagents were removed using a QIAquick nucleotide removal kit (QIAGEN). For the confirmation of ligands, samples were first mixed with monomeric kinesin-$SNAP_f$ or dimeric kinesin-Halo protein, and confirmed using urea PAGE. Ligand-conjugated oligonucleotides were stored at -30°C and used with other staples.

Binding assay

A honeycomb-type, 30-helix bundle (30HB) DNA origami rod was designed by Dr. Hisashi Tadakuma using caDNAno (Maya Plug-in; Fig. 1; Supplementary Tables 3 and 4). Single-stranded M13mp18 DNA (40 nM, tilibit nanosystems) and 260 nM of each staple (6.5-fold excess) were mixed in Barrel Buffer and heated at 85°C for 5 min and annealed at 47.5°C for 4 h. Purified 30HB rods were provided by Dr. Hisashi Tadakuma. Briefly, monomeric 30HB rods were purified gel electrophoresis (Douglas et al., 2009) and concentrated by polyethylene glycol (PEG) precipitation (Stahl et al., 2014). The molar concentration was determined by NANODROP 1000 (Thermo Scientific) with an approximate molecular mass of 9.4 MDa. The purified 30HB rods were frozen in liquid nitrogen and stored at −80°C.

The 30HB rods were mixed with kinesin in 5 mM tris(hydroxymethyl)aminomethane (Tris)-borate (pH 7.6), 4 mM PIPES (pH 7.0), 1–4 mg/mL casein, 80 mM KCl, 20 mM $Mg(OAc)_2$, 1 mM ethylenediaminetetraacetic acid (EDTA), 50 μM ATP, and 1 mM

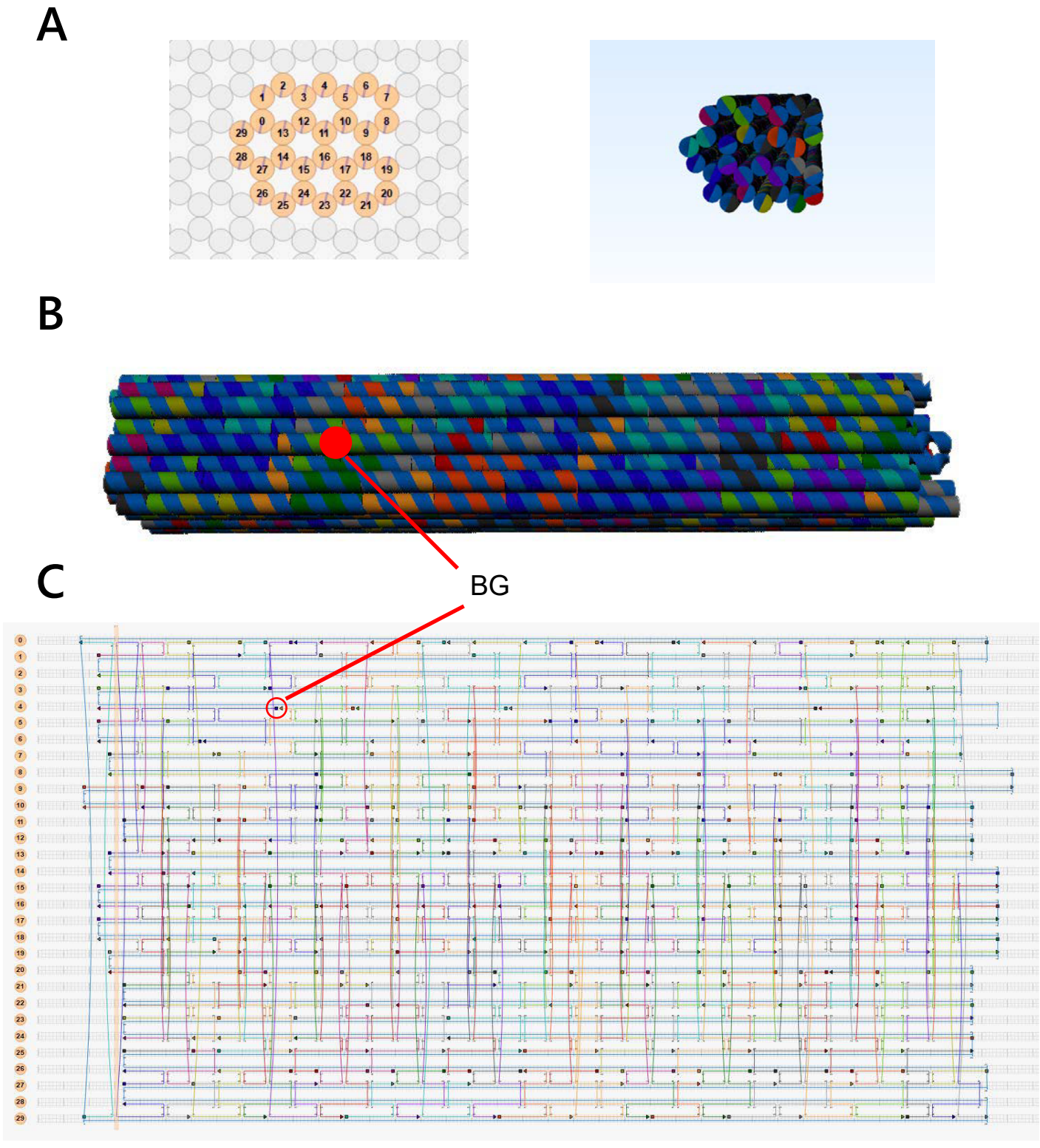

Fig. 1 | Structure and layout of the 30HB rod

(A) Cross section image of caDNAno (left) and Maya (right). (B) Bottom view shows the position of BG (red circle). (C) Strand diagram of the 30HB rod rendered using caDNAno. Each row denotes a helix of double-stranded DNA. Each gray square-lattice unit denotes a nucleotide. The scaffold DNA is folded with hundreds of staples (shown in colorful lines; squares and arrowheads denote 5' and 3' ends, respectively). This information was kindly provided by Prof. Hisashi Tadakuma.

dithiothreitol (DTT) and incubated at room temperature (RT). The reaction was stopped by immediately performing electrophoresis or by adding 20 μM BG-conjugated oligonucleotide. Kinesin concentrations were adjusted to ensure the reaction time to be long enough for operation (more than seconds). Agarose gel electrophoresis was performed using 0.7% agarose (Bio-Rad, Cat. #1613101, Control BRD00117) and 0.5× TBE (Medicago and nacalai tesque) supplemented with 12 mM $MgCl_2$ with or without 0.1% SDS (Sommese et al., 2016) for 1 h at 100 V. Dye-labeled DNA and kinesin were detected using a Typhoon FLA 9500 scanner (Cytiva).

Rates of binding between 30HB rods and kinesins were estimated using ImageJ (Schneider et al., 2012) graphical user interface and custom Python scripts. In mobility shift assays, the binding ratio R was calculated as follows:

$$R = 1 - \frac{D}{D_0} \qquad \text{(Equation 1)}$$

where D is the signal from the unbound 30HB rod of each lane and D_0 is the signal from unbound DNA without proteins. In the case of an increase in Cy3 optical density, R was calculated as follows:

$$R = \gamma \times \frac{D - D_0}{D_{\max} - D_0} \qquad \text{(Equation 2)}$$

where D is the Cy3 signal co-localized on the 30HB rod of each lane, D_0 is the signal of the 30HB rod without kinesin, $D_{\max}$ is the Cy3 signal of the positive control (PC), and γ is the maximum binding ratio. Each time-course plot was fitted using a Python script with single exponential functions:

$$R = \beta \times (1 - e^{-at[kinesin]}) \qquad \text{(Equation 3)}$$

where β is the amplitude and a is the rate of binding between the 30HB rod and kinesin at the kinesin concentration ([kinesin]). To determine the kinesin assembly speed (on-rate: k_{on}), the

binding rate was plotted against kinesin concentration and fitted with a linear least-squares function ($a = k_{on}$ [kinesin]).

SNAP$_f$ folding analysis

Dimeric kinesin-SNAP$_f$s were incubated for 1.5 h at RT with a BG-conjugated oligonucleotide prepared as below at a SNAP$_f$/BG molar ratio of 1:4. The reactions were subjected to SDS-PAGE, followed by staining with CBB. Peptides were detected using a Typhoon FLA 9500 scanner (Cytiva). Images were quantified using ImageJ (Schneider et al., 2012).

The BG-conjugated oligonucleotide [BG-TTTTTTTCTGGAGCAAACAAGAGAAGGAGACAGTCAAATACAGTTGATTCCCA] was prepared as described in the section "Conjugation of ligands to oligonucleotide," with a modification of the purification process. During experiments, the remaining unreacted BG that was used in excess amount for oligonucleotide modification, impeded the binding between kinesin-SNAP$_f$s and BG-conjugated oligonucleotides. Therefore, unreacted BG-GLA-NHS was carefully removed in three steps using QIAquick nucleotide removal kit (QIAGEN), MicroSpin S-200 HR column (Cytiva), and then QIAquick nucleotide removal kit again. Mobility shift assay showed that the three-step purification process improved the binding ratio of kinesin-SNAP$_f$s to BG-conjugated oligonucleotide.

Assembly of transport complexes for single-molecule imaging

Square lattice-type and 28-helix bundle (28HB) DNA origami rods were designed using caDNAno (Fig. 2; Supplementary Tables 5 and 6) and prepared by Dr. Hisashi Tadakuma. Briefly, 40 nM single-stranded P8064 DNA (tilibit nanosystems) and 275 nM of each staple (7-fold excess) were mixed in Barrel Buffer, heated at 85°C for 5 min and annealed at 52.5°C for 4

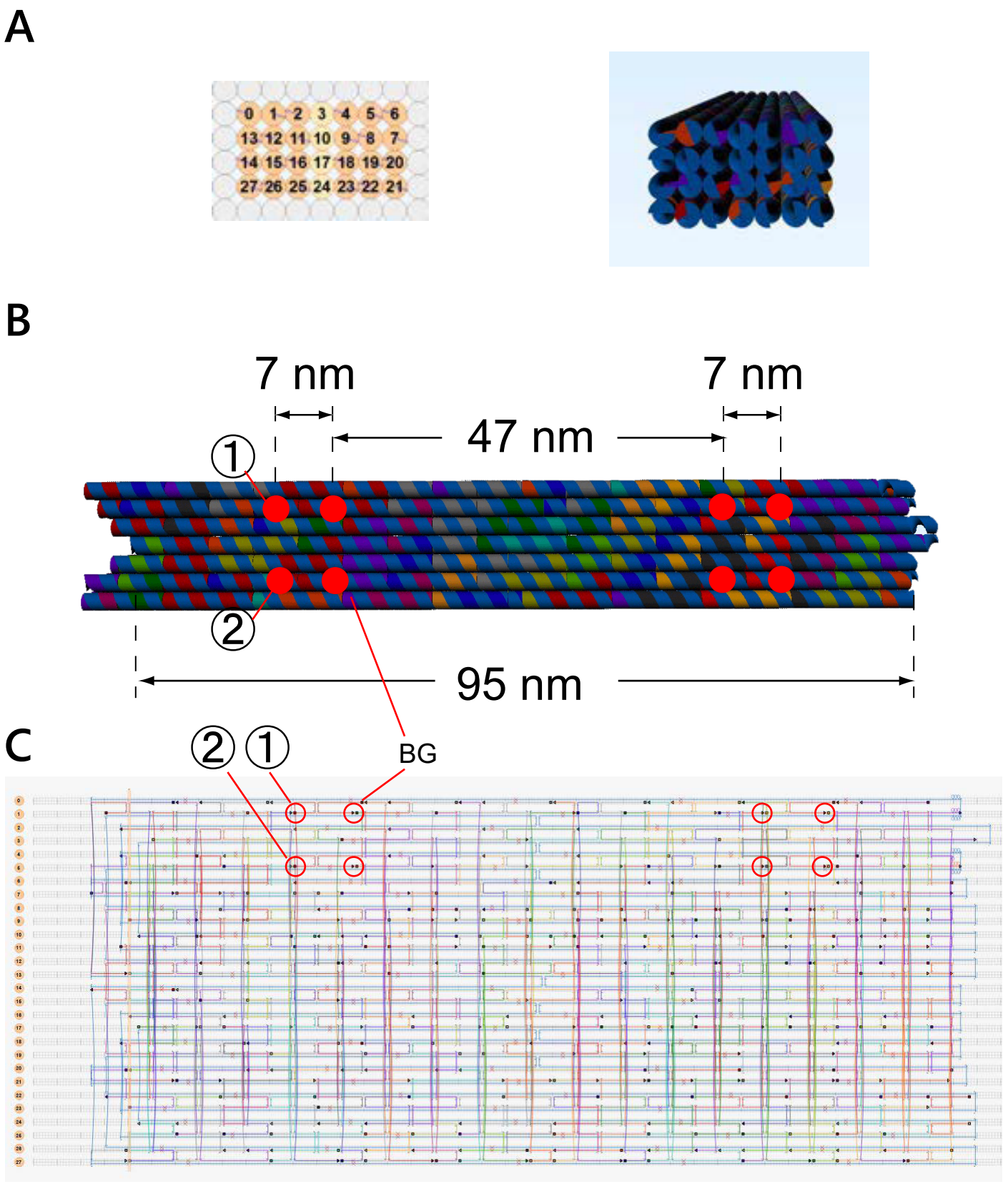

Fig. 2 | Structure and layout of the 28HB rod

(A) Cross section image of caDNAno (left) and Maya (right). (B) Bottom view shows the position of BG (red circle). The indicated numbers of the BG sites are explained in the Results section. (C) Strand diagram of the 28HB rod rendered using caDNAno, shown as in Fig. 1. This information was kindly provided by Prof. Hisashi Tadakuma.

h. The folded 28HB rods were purified with the same method as for 30HB rods.

Dimeric kinesin-$SNAP_f$-10K partially labeled with BG-Alexa Fluor 647 (A647) was mixed with 28HB rod at a BG/$SNAP_f$ molar ratio of 1:10 in 22 mM PIPES (pH 7.0), 0.8 mg/mL casein, 220 mM NaCl, 12 mM $MgCl_2$, 0.9 mM EGTA, 43 μM ATP, and 1 mM DTT, incubated for 5 h at RT and purified multiple times using MicroSpin S-300 or S-400 HR columns (Cytiva) equilibrated with 25 mM PIPES (pH 7.0), 0.8 mg/mL casein, 250 mM NaCl, 12 mM $MgCl_2$, 1 mM EGTA, 50 μM ATP, and 1 mM DTT. Eluates were frozen in liquid nitrogen and stored at -80°C after adding 10% sucrose.

Single-molecule imaging

Flow cells were prepared using quartz glass and were used after PEG-coating as previously reported (Aoki et al., 2013) with some modifications. Briefly, flow cells were constructed between a quartz glass slide and a coverslip, cleaned using KOH, by placing a polyethylene spacer of 40 μm thickness. The flow cells were coated with 1 mg/mL methoxy-poly(ethylene-glycol)-block-poly(L-lysine hydrochloride) (mPEG5K-bPLKF10; Alamanda Polymers) in BRB12 buffer for 0.5–6 h. After washing with 40 μL BRB12 buffer, axonemes were injected into the cells and adsorbed for more than 15 min at RT. Prior to sample infusion, the cell was washed and equilibrated with 40 μL of BRB12(X) buffer (BRB12 buffer supplemented with sodium chloride at the concentration described in each figure). The concentration of sodium chloride was optimized based on the aim of each experiment since a trade-off between the experimental efficiency and accuracy of estimation existed. Fluorescence imaging was initiated after infusing fluorescently labeled kinesins (12–250 pM) or 28HB rod–kinesin complexes (30–200 pM) in motility buffer [1 mg/mL casein, 4.5 mg/mL glucose, 50 U/mL glucose oxidase, 50 U/mL catalase, 2 mM Trolox, 0.5% 2-mercaptoethanol, and 1 mM ATP in BRB12(X) buffer].

Images were captured within 25 min after sample preparation to eliminate the effects of ATP consumption.

Movements of kinesins were captured using a total internal reflection fluorescence (TIRF) microscope installed by Prof. Hisashi Tadakuma. Briefly, an inverted-type microscope (IX70; Olympus) with an 150x objective lens (Olympus, UVpo N; 150x, 1.4 NA) was equipped with a He-Ne laser (633 nm for Cy5 and Alexa Fluor 647; 10 mW; 05-LHP-991; Melles Griot) and diode laser (532 nm for Cy3; 100 mM; Sapphire SF 532-100CW CDRH; Coherent Inc.) (Miyazono et al., 2010). Fluorescence images were separated using Dual-View (Teledyne Photometrics) with filters of Chroma 635DCXR and Semrock, FF01-572/28-25. Signals were captured using an electron-multiplying CCD camera (iXon+, DU897C-CS0-#BV, Andor Technologies) and the software of Andor SOLIS for Imaging (Solis v.4.22.30007.0; SDK v.2.94.30007.0). Images were obtained with a gain of 200 and frame rates of 3-5 fps. Room temperature was adjusted to 23±1°C. Pixel values of the images were confirmed within the linear range of the sensor and were not saturated.

Analysis of single-molecule imaging data

Run length, velocity, and fluorescence intensities were analyzed using custom Fiji macros and Python scripts using kymographs, as previously described (Derr et al., 2012), with some modifications. Kymographs were generated from axonemes with an average length of 18 μm. The variation (σ) of single fluorophores was determined using Gaussian fitting (0.17 μm). Particles were recorded using Fiji GUI and selected by the following criteria; Particles with run lengths < 0.5 μm (approximately 3σ) were removed since the trace was difficult to be distinguished from that of non-specific binding; particles bound to axonemes within 3.5 μm (spatial axis) or 10 sec (time axis) at the edges of kymograph in the direction of movement were

excluded to reduce the influence of particles that reached the edges of kymographs, for which accurate measurement of run lengths was not possible; particles that did not meet the criteria but reached the edges of kymograph were treated as detached and included in analysis.

Motile parameters were obtained from two different types of regions of interest (ROIs) for each particle. Run lengths were determined as the length that each particle moved between association and dissociation or reaching an edge of the kymograph. For analyzing velocities and fluorescence intensities, the longest and linear ROIs without overlap with other particles were selected in the trace of each particle. The ROIs were used to determine the average velocity and means of intensities of Cy3 and A647. Average velocities and standard deviations were calculated by fitting each velocity histogram with the following Gaussian distribution function:

$$f(x) = \mathrm{amp} \times \exp\{ - (x - \mu)^2 / (2 \times \sigma^2) \} \quad (1),$$

where amp is amplitude, μ is the average velocity, and σ is the standard deviation. Average run lengths were determined by fitting each cumulative distribution of run lengths with a single-exponential function:

$$f(x) = 1 - \mathrm{amp} \times \exp(- x / x_c) \quad (2),$$

where amp is amplitude and x_c is the average run length > 0. Standard errors of means were estimated by Bootstrap sampling and fitting with the same function 200 times, as previously reported (Derr et al., 2012).

Statistical analysis was performed using custom R and Python scripts (https://github.com/maximtrp/scikit-posthocs) with some modifications. Velocities were tested with parametric tests. First, the global difference was analyzed by one-way analysis of variance (ANOVA). When significant difference was noticed, the differences between groups were further analyzed by a Tukey's test (in the absence of a control group) or Dunnett's test (in the presence of a control group) In contrast, run lengths were non-parametric (Shapiro–Wilk test,

$p<0.05$) and tested using non-parametric tests. First, the global difference was analyzed by the Kruskal–Wallis test. When significant difference was noticed, the differences between data were further analyzed by the Conover–Iman test (in the absence of a control group). By contrast, no significant difference was observed in data in the presence of a control group. Parametric data (velocity) show less *P*-value (more significance) than do non-parametric data (run length).

Single-molecule photobleaching assay

The assays were performed as described in the section "Single-molecule imaging," except for the following modifications. Fluorescence imaging was initiated after infusing A647-labeled dimeric kinesin-$SNAP_f$-10K or 28HB rod–kinesin complexes (2.5 pM) in motility buffer supplemented with 2 mM AMP-PNP instead of ATP. The time traces of A647 and/or Cy3 intensities were analyzed using custom Fiji macros and Python scripts, in which each photobleaching point was finally determined by eye. The A647-labeled fractions were calculated from the histograms of step numbers with least-squares fitting to a binomial distribution using custom Python scripts.

I-3. Results

Characterization of poly-lysine-fused proteins

A new peptide sequence was developed to improve the efficiency of protein assembly on DONs. Previous studies have reported that binding efficiency may be improved by conjugating tag-proteins, such as SNAP-tag and HaloTag, to additional polypeptide-based functional modules, that can interact with the oligonucleotide handles of a DON (Nakata et al., 2015; Nguyen et al., 2017). Positively charged poly-L-lysine peptides are known to interact with large DNA molecules (Akitaya et al., 2007). These findings led to the hypothesis that conjugating a poly-

lysine sequence to a tag-protein would improve the efficiency and/or the speed of protein assembly on DONs. To evaluate this assumption, five (5K) or ten (10K) lysine residues were introduced into the C-terminal of $SNAP_f$-tag (an advanced type of SNAP-tag with high-binding kinetics) of a dimeric kinesin-$SNAP_f$ protein (Fig. 3, A and B). These fusion proteins were expressed in an *E. coli* strain and then purified via Ni-NTA chromatography followed by ion-exchange chromatography (Fig. 3C). Affinity purification using His-tag in the C-terminal of a poly-lysine, helped remove truncated peptides and purify proteins with full length poly-lysine.

The effect of poly-lysine on the folding and activity of $SNAP_f$-tag was evaluated first. An oligonucleotide conjugated with the $SNAP_f$ substrate (BG) was used to examine $SNAP_f$ activity. SDS-PAGE showed mobility shifts of the $SNAP_f$-tagged peptides bound to the BG-labeled oligonucleotide. In excess of 94% of the poly-lysine-fused dimeric kinesin-$SNAP_f$ proteins showed mobility shifts (Fig. 4), indicating that poly-lysine-fused $SNAP_f$-tags had covalently-bound to the substrate, in a manner similar to how an original $SNAP_f$-tag would bind to the same substrate (0K, 88%). Notably, the calculated values may be underestimated due to the insufficient removal of free BG.

A TIRF microscope was used to analyze the motility of poly-lysine-fused dimeric kinesin-$SNAP_f$ proteins. The proteins were fluorescently-labeled and their movements along axonemes were visualized (Fig. 5A). Poly-lysine-fused proteins were non-specifically adsorbed on the plain glass surface. Therefore, the glass surface was coated with PEG and the observation condition was optimized (e.g., ionic strength; Materials and Methods). Such optimization of observational conditions allowed the movement of poly-lysine-fused dimeric kinesin-$SNAP_f$s along axonemes to be visualized (Fig. 5B). Velocities of poly-lysine-fused proteins were largely similar to those without a poly-lysine, as shown by a difference of only ±9% between the velocities of poly-lysine-fused proteins and 0K lysine constructs (Fig. 6, A and B), which

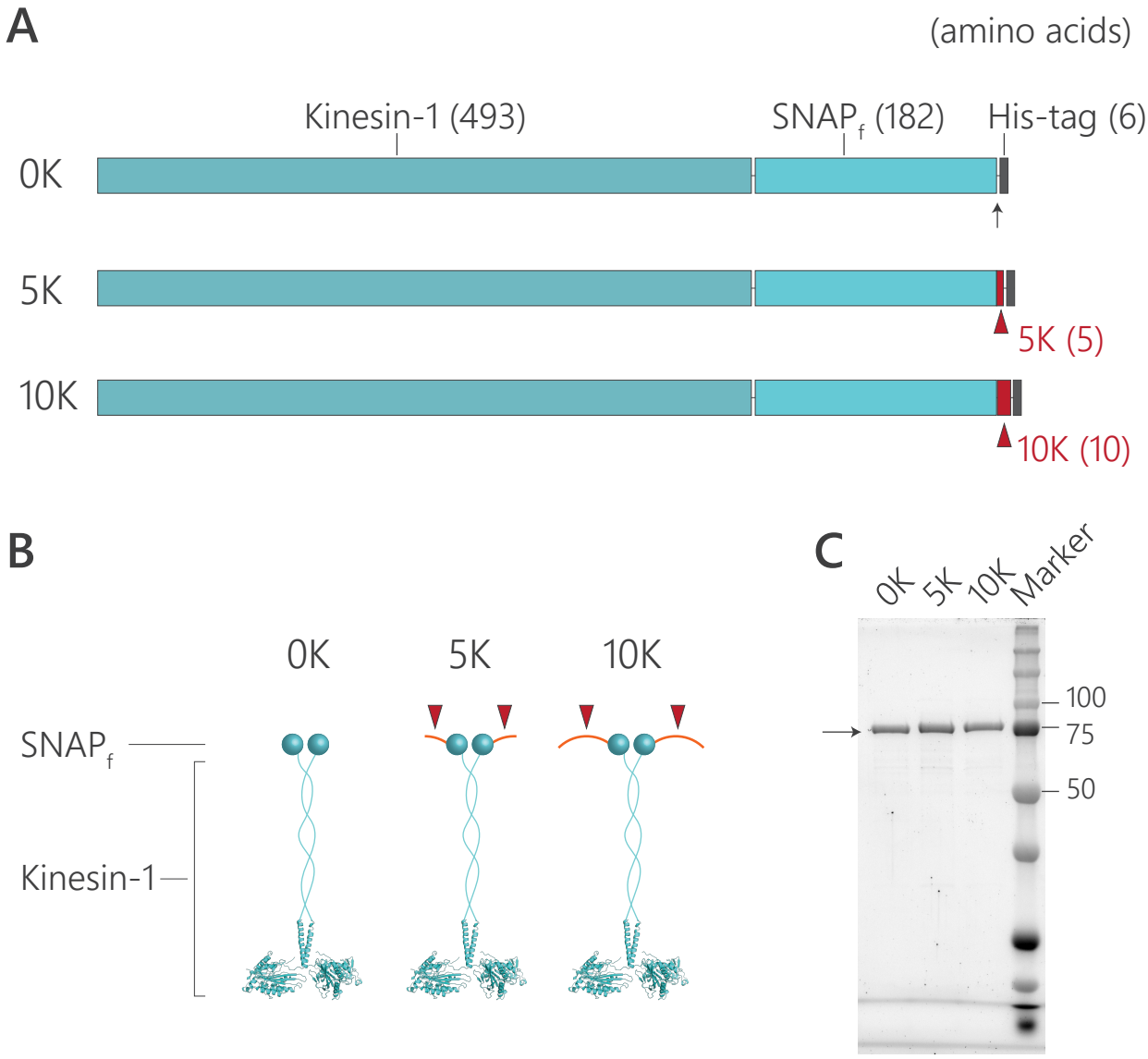

Fig. 3 | Poly-lysine was introduced to a dimeric kinesin-SNAP$_f$ protein

(A) Schematic of dimeric kinesin-SNAP$_f$ constructs. The residues of KKKKK (5K) and KKK-KKKKKKK (10K) were introduced between SNAP$_f$ and His-tag of kinesin-SNAPf-His-tag gene. The numbers in parentheses indicate numbers of amino acid residues. The lengths of all components are illustrated as proportional to the residual length. (B) Schematic of the proteins showed in (A). The proteins are dimerized by the coiled-coil domain of kinesin-1. Poly-lysine sequences (5K and 10K) are illustrated in red and indicated with arrow heads. His-tag is omitted in the figure. (C) SDS-PAGE of purified proteins. Change in the mobility of poly-lysine-fused constructs was less, confirming that the poly-lysine exerted minimal effect on the peptide length.

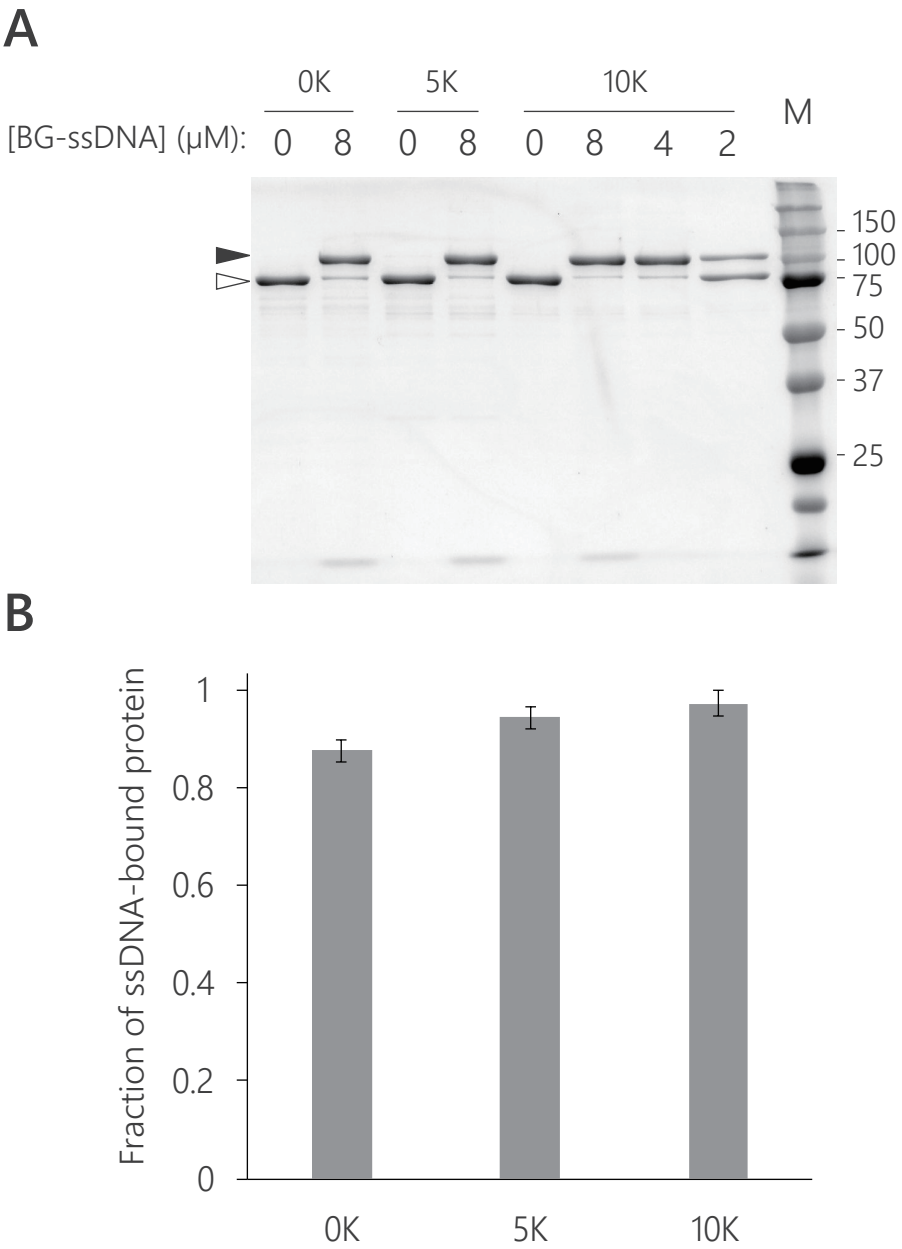

Fig. 4 | Poly-lysine-fused SNAP$_f$ proteins can bind to a BG-substrate

(A) SDS-PAGE showing the mobility shift of dimeric kinesin-SNAPf proteins bound to a BG-conjugated oligonucleotide (BG-ssDNA). The dimeric kinesin-SNAP$_f$s with 0K, 5K and 10K (1 μM) were incubated for 1.5 h at 25°C with BG-ssDNA (0, 2, 4 or 8 μM). Open and filled arrowheads denote free and BG-ssDNA-bound proteins, respectively. (B) Fractions of dimeric kinesin-SNAP$_f$s bound to BG-ssDNA. More than 94% of the poly-lysine-fused proteins (5K and 10K) showed the mobility shift. Note that the fractions of ssDNA-bound proteins were affected by free BG ligands, which was not completely removed and blocked binding between SNAP$_f$ and BG-ssDNA. The free BG more likely affects the 0K protein, which has no additional positive charge and would be harder to bind to the negatively charged BG-ssDNA than poly-lysine-fused proteins. Error bars indicate standard deviation of three independent experiments.

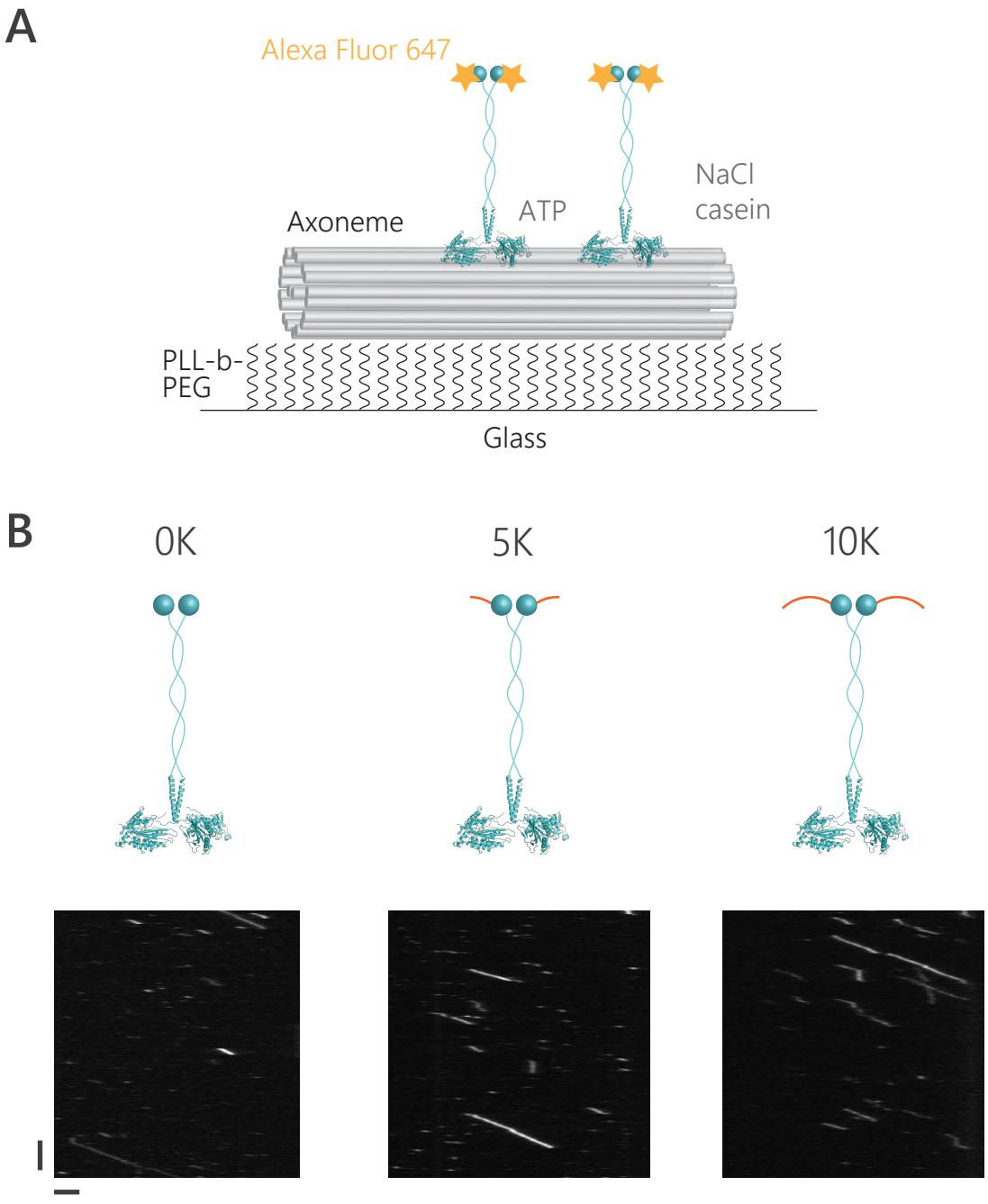

Fig. 5 | Single-molecule imaging showed poly-lysine-fused dimeric kinesin-SNAP$_f$ proteins moving along axonemes

(A) Schematic of single-molecule imaging. Axonemes, which contains microtubules, were adsorbed on a PEG-coated glass surface. Dimeric kinesin-SNAP$_f$ proteins (0K, 5K and 10K) were fluorescently labeled with BG-Alexa Fluor 647 (A647) and their movements on axonemes were visualized in the presence of 1 mM ATP. PEG, NaCl and casein were used to avoid non-specific absorption of the proteins on the glass surface. (B) Representative kymographs of dimeric kinesin-SNAP$_f$ proteins moving along axonemes. Movements were visualized using A647 fluorescence. Scale bars: vertical axis, 10 s; horizontal axis, 2 µm.

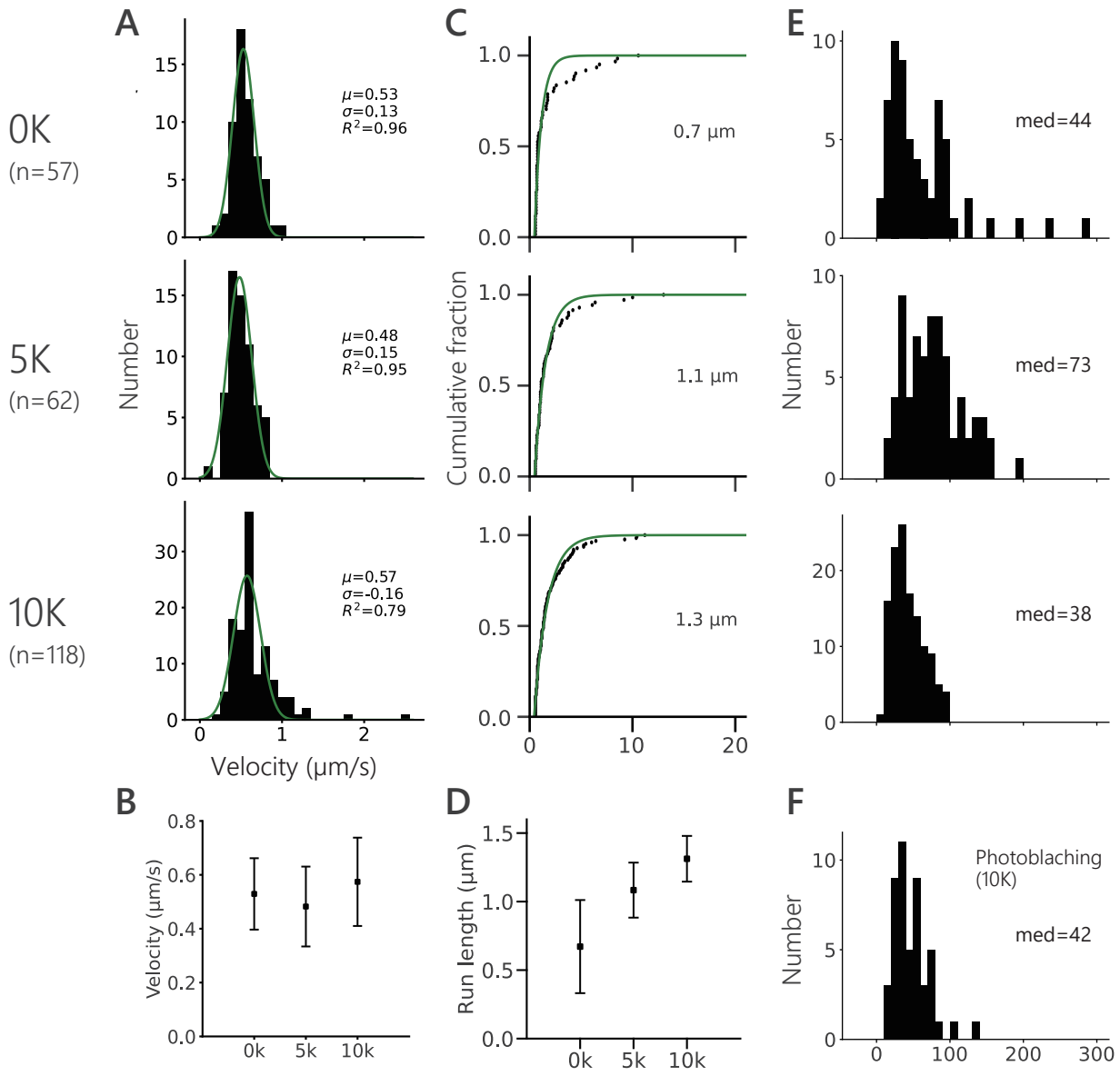

Fig. 6 | Effect of poly-lysine on motilities of dimeric kinesin-SNAP$_f$ proteins

(A-E) Analyses of dimeric kinesin-SNAP$_f$ proteins moving along axonemes. (A and B) Histograms (A) and a scatter plot (B) of velocities. Plots (μ) and error bars (σ) in (B) were determined by fitting the histograms in (A) with a Gaussian function. (C and D) Cumulative distribution functions (CDFs; C) and a scatter plot (D) of run lengths. Plots in (D) were determined by fitting the CDFs with a single-exponential function; error bars were estimated via bootstrap sampling. (E) Histograms of A647 fluorescence intensities of particles moving along axonemes. (F) Histograms of single A647 fluorophore intensities determined by photobleaching of kinesin-SNAP$_f$-10K protein immobilized on axonemes with AMP-PNP.

indicated that poly-lysine had not affected the enzymatic and motile activity of dimeric kinesin. On the other hand, increasing the number of lysines caused their run lengths to be longer (Fig. 6, C and D). These velocity and run length results were consistent with those of a previous study, which introduced 5 lysine residues into the neck coiled-coil of kinesin-1 (Thorn et al., 2000), suggesting that lysine had interacted with tubulin's C-terminal. Fluorescent intensities of the moving dimeric kinesins, which would have up to two fluorophores, were also analyzed and confirmed to be within 1–2 times the intensity of a single fluorophore determined by photobleaching (Fig. 6, E and F), suggesting that poly-lysine does not cause the proteins to aggregate. These results indicated that poly-lysine had not impeded either labeling activity of $SNAP_f$ or the motile activity of kinesin.

Poly-lysine accelerated the speed of kinesin assembly on a DON

Next, I investigated whether the speed of assembly of a POI on a DON could be improved by adding poly-lysine. In this experiment, a rod-shaped, 30HB DNA origami rod designed by Prof. Hisashi Tadakuma (Fig. 1) was used as a model nanostructure. To estimate the binding rate of $SNAP_f$-tagged kinesin molecules, a BG-modified ssDNA handle was incorporated into the 30HB rod, and the rod was allowed to react with $SNAP_f$-tagged kinesins to form a complex (Fig. 7).

The effect of the assembly of dimeric kinesin-$SNAP_f$s (0K, 5K, and 10K) was monitored using native agarose gel electrophoresis. Incubation with the $SNAP_f$-tagged proteins caused a mobility shift in the 30HB rods with a BG-handle, but not in those without a BG-handle (Fig. 8A). This indicated that specific binding had occurred between $SNAP_f$-tags in the proteins and the BG handle on the 30HB rod. The binding fraction was estimated in a time-dependent manner in order to calculate binding efficiency. Considering that the rate of binding between

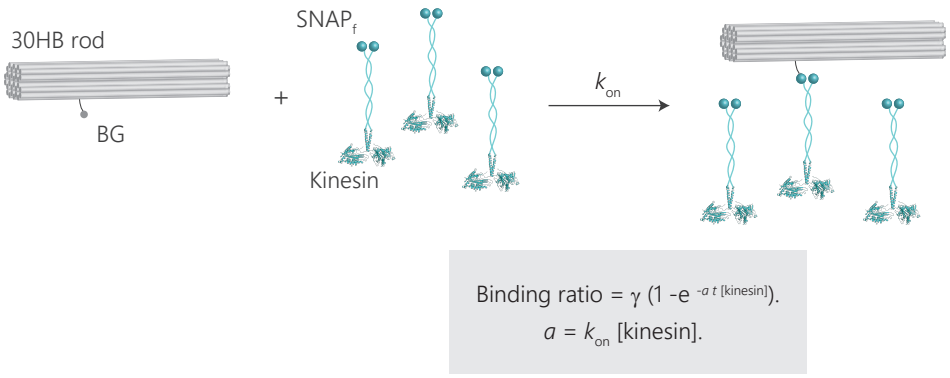

Fig. 7 | Determination of second-order rate constants for binding between SNAP$_f$ -tagged kinesins and BG-integrated 30HB rod

Schematic of binding assays. 30HB rods with a BG ligand were incubated with kinesin-SNAP$_f$ proteins and the second-order rate constant (k_{on}) for binding ratios were determined at different reaction times.

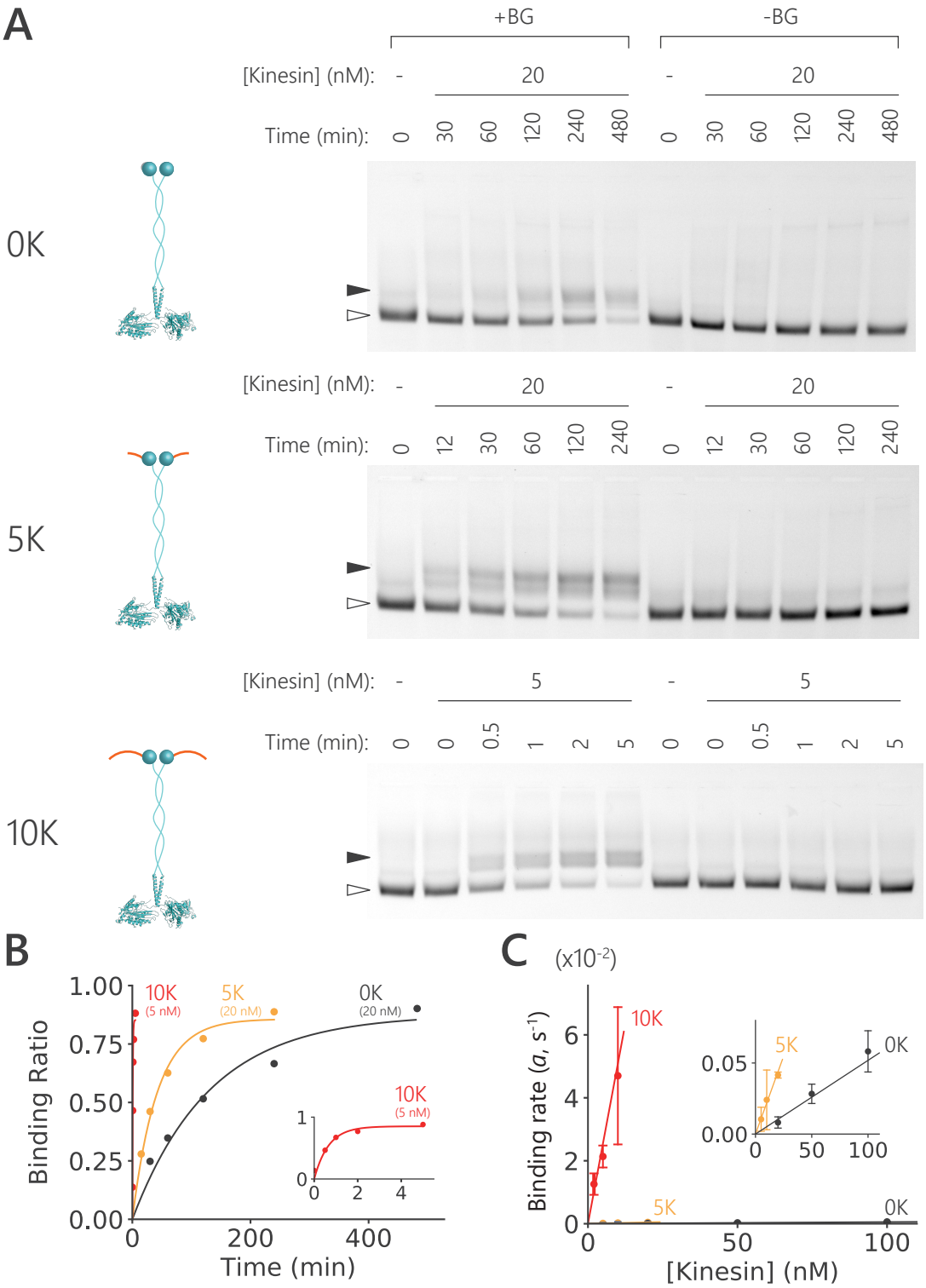

Fig. 8 | Poly-lysine accelerated assembly of a dimeric kinesin-SNAP$_f$ protein on the 30HB rod

(A) Images of 0.7% agarose gel showing time-dependent assembly of dimeric kinesin-SNAP$_f$ proteins (0K, 5K and 10K). Cy5-labeled 30HB rods were detected via fluorescence. The proteins and 30HB rods (2 nM) with or without BG-handle (±BG) were incubated at RT. The reaction times and concentrations of the proteins were adjusted to ensure that the reaction time was sufficient for the operation to complete. Open and filled arrowheads denote free 30HB rods and kinesin-SNAP$_f$ proteins bound to BG-30HB rods, respectively. (B) Time-course of binding between the dimeric kinesin-SNAP$_f$ proteins and the BG-anchored 30HB rod, as determined from gel images. Inset, the horizontal axis is re-scaled for 10K. (C) Biding rates were plotted against the molar concentrations of the dimeric kinesin-SNAP$_f$ proteins. Inset, the vertical axis was re-scaled to clearly show the data of 0K and 5K. Linear fitting revealed the following second-order rate constants: 0K, 6×10^3 M^{-1} s^{-1}; 5K, 2×10^4 M^{-1} s^{-1}; 10K, 4×10^6 M^{-1} s^{-1}. Error bars indicate the standard deviations of more than three independent experiments.

two molecules depends on the concentrations of the molecules, the concentration of the 30HB rod was fixed 2 nM; the concentration of proteins was adjusted to ensure that reaction times were sufficiently longer than the time required for proper operation. Time-dependent mobility shifts of 30HB rods with a BG-handle were observed after incubating with dimeric kinesin-$SNAP_f$ proteins (Fig. 8A). The 5K protein took a shorter time to bind to the 30HB rod than the 0K protein (Fig. 8, A and B). In addition, the 10K protein which exhibited a shorter reaction time than both 0K and 5K proteins, at a lesser concentration, assembled on the 30HB rod more efficiently (Fig. 8, A and B). These results indicated that poly-lysine had accelerated the speed of binding between the BG-labeled 30HB rod and $SNAP_f$-tagged dimeric proteins. Estimation of binding rates at several different protein concentrations indicated that the second-order rate constants (k_{on}) for 0K, 5K, and 10K were 6×10^3, 2×10^4, and 4×10^6 M^{-1} s^{-1}, respectively (Fig. 8C). This showed that the 10K had accelerated the speed of protein assembly by a factor of 700. Notably, the 30HB rod, even without a BG-handle, tended to aggregate at higher protein concentrations (>50 nM; Fig. 9), making it difficult to obtain a high yield of the complex. In stark contrast, poly-lysine achieved high binding speeds and thus facilitated complex formation with less protein concentrations and shorter incubation times.

The faster assembly of 10K-tagged protein was confirmed using a fluorescently labeled protein. The 10K-tagged dimeric kinesin-$SNAP_f$ was labeled using Cy3-NHS, which randomly reacts with lysine residues on the surface of proteins, and purified using a Ni-NTA resin. The Cy3-labeled protein was incubated with the 30HB rod. The concentration of the 30HB rod was adjusted to 5 nM to clearly visualize the Cy3 fluorescence of proteins bound to the 30HB rod. The Cy3-labeled dimeric kinesin-$SNAP_f$-10K caused mobility shifts of the BG-labeled 30HB rod in native agarose gel (Fig. 10A), where these shifts were similar to those shown by unlabeled proteins in the previous experiment. However, protein assembly on the 30HB rod

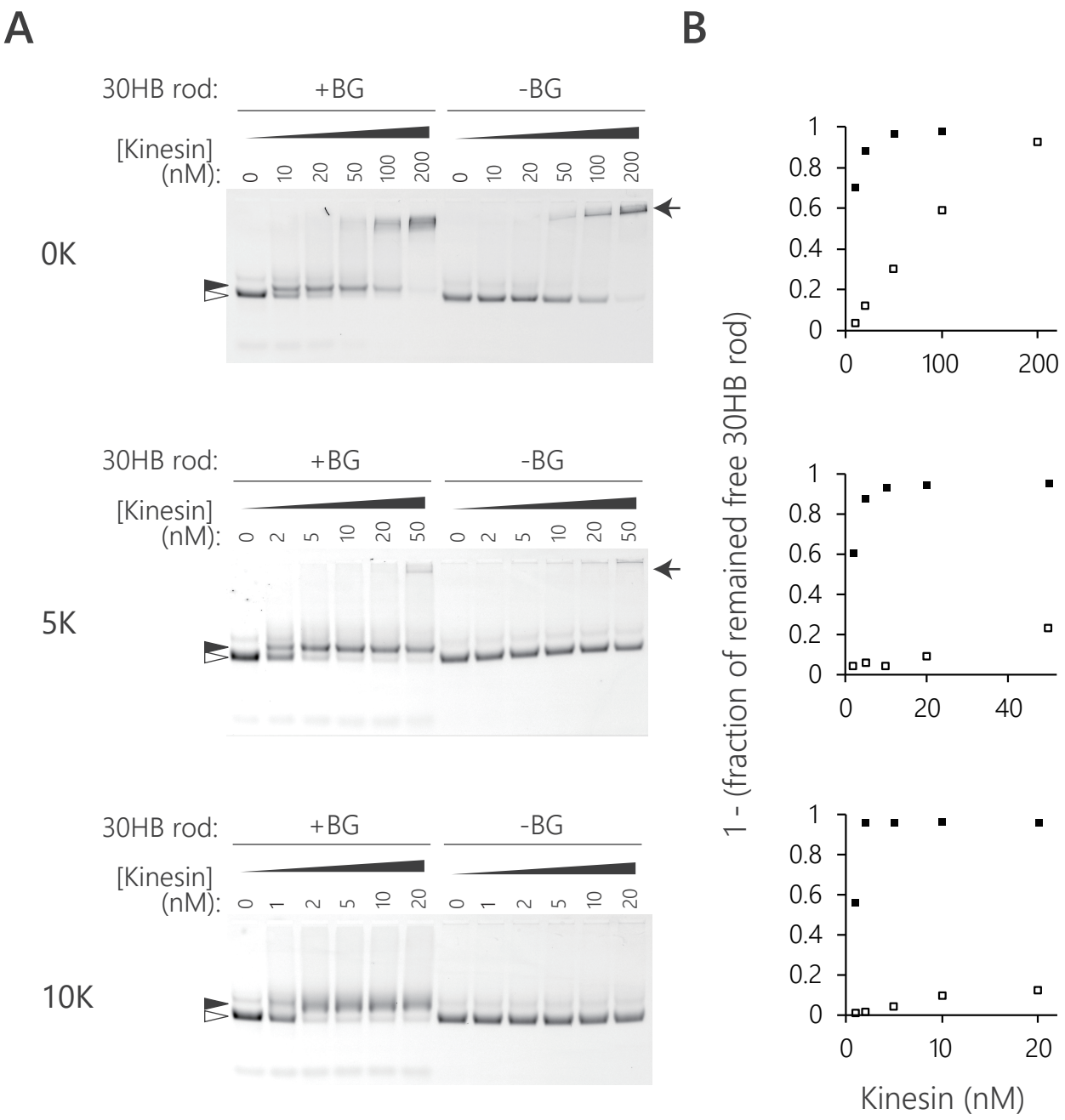

Fig. 9 | Poly-lysine allows assembly of kinesin without DNA rod aggregation

(A) Images of 0.7% agarose gel. Cy5-labeled 30HB rods were detected via fluorescence; 30HB rods (2 nM) with or without a BG-handle were mixed with indicated concentrations of dimeric kinesin-SNAP$_f$ (0K, 5K or 10K) in 23 mM PIPES (pH 7.0), 0.8 mg/mL casein, 230 mM NaCl, 12 mM $MgCl_2$, 1 mM EGTA, 50 mM ATP and 1 mM DTT, and incubated for 8 h (0K and 5K) or 3 h (10K) at 25°C. Open and filled arrowheads denote free 30HB rods and kinesin-SNAP$_f$ proteins bound BG-30HB rods, respectively. Arrows indicate aggregated 30HB rods, which might move while destroying gel. (B) The fractions of free 30HB rods that remained [indicated with open arrowheads in (A)] was measured and subtracted from 1 to display similarly (Fig. 8B). Note that any reduction in DNA rods without a BG-handle is caused by DNA rod aggregation, whereas that of DNA rods with a BG-handle is caused by both aggregation and kinesin assembly.

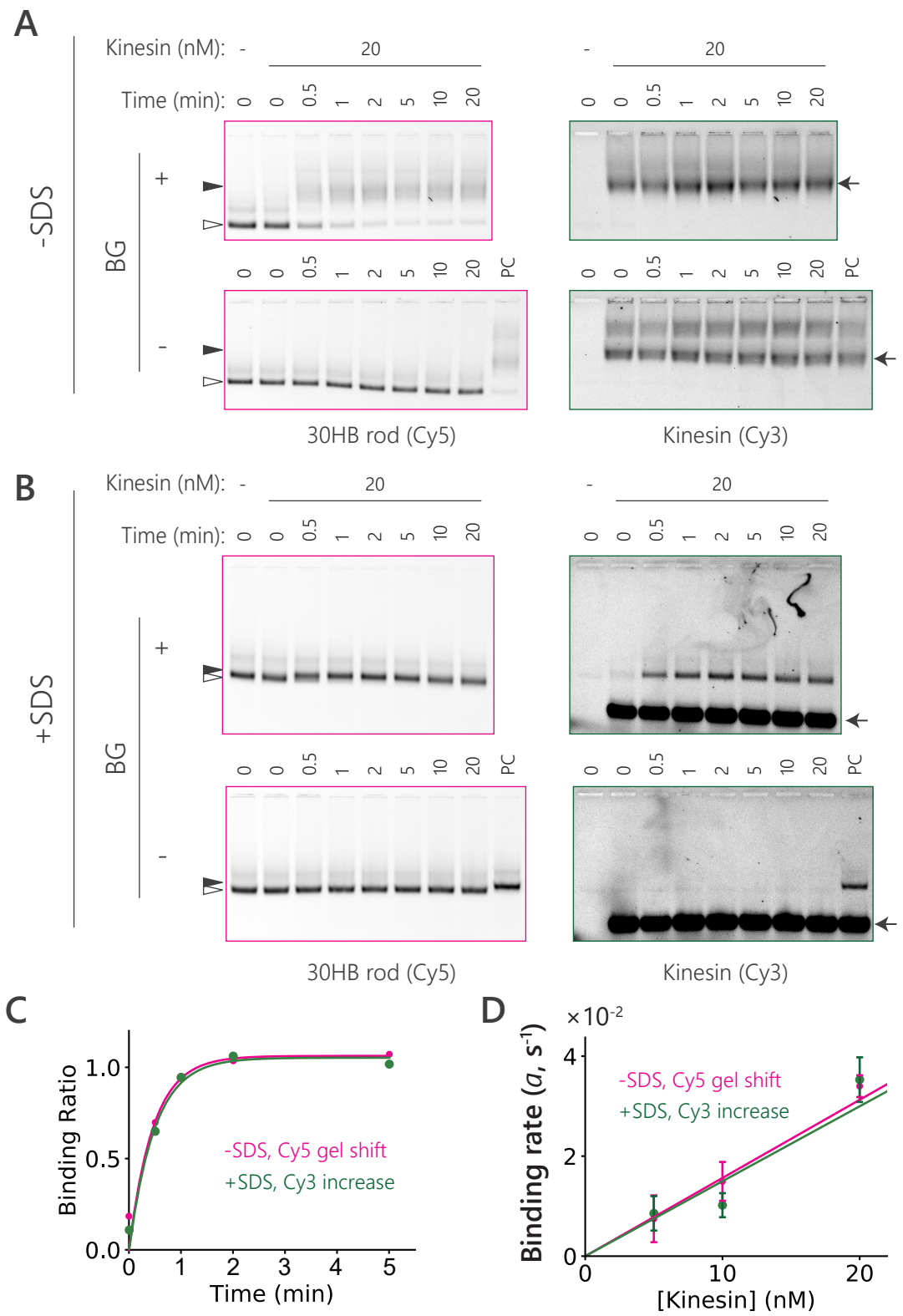

Fig. 10 | Fast assembly on 30HB rods was confirmed using fluorescently labeled dimeric kinesin-SNAP$_f$-10K

(A and B) Images of 0.7% agarose gel. Cy5-labeled 30HB rods and Cy3-labeled dimeric kinesin-SNAP$_f$-10K were detected via fluorescence. The dimeric kinesin-SNAP$_f$-10K used in Fig. 8 was labeled with Cy3-NHS and purified. 30HB rods (5 nM) with or without a BG-handle were incubated with the Cy3-labeled kinesin for the indicated times and analyzed by the same gel (Fig. 8) (A) or agarose gel supplemented with 0.1% SDS (B); 30HB rod with a BG-handle incubated for 20 min with the kinesin was loaded as a positive control (PC) for -BG samples. Open and filled arrowheads denote free 30HB rods and kinesin-SNAP$_f$ proteins bound BG-30HB rods, respectively. Arrows indicate free kinesin-SNAP$_f$-10K protein. Note that SDS affects the charge of the protein and dissociates the coiled-coil domain, dissociating dimeric protein into monomeric polypeptides. (continued to the next page.)

Fig. 10 | Fast assembly on 30HB rods was confirmed using fluorescently labeled dimeric kinesin-SNAP$_f$-10K

(continued from the previous page) (C) Time-course of binding between 20 nM Cy3-labeled dimeric kinesin-SNAP$_f$-10K and BG-attached 30HB rods determined using two different methods: (i) mobility shifts of Cy5-labeled 30HB rods in -SDS gel (same as Fig. 8B); and (ii) an increase in Cy3 fluorescence of 30HB-bound kinesin in +SDS gel. (D) Binding rates that were determined using the two different methods were plotted against molar concentrations of Cy3-labeled dimeric kinesin-SNAP$_f$-10K. Linear fitting determined second-order rate constants: (i) mobility shift in -SDS gel, 2×10^6 M^{-1} s^{-1}; and (ii) Cy3-fluorescence increase in +SDS gel, 2×10^6 M^{-1} s^{-1}; error bars indicate standard deviations of three independent experiments.

could not be detected via the fluorescence of the protein, since the mobility of the free Cy3-labeled protein was almost the same as that of the complex on which the protein was assembled on the 30HB rod (Fig. 10A, arrows). To separate free protein from the complex, sodium dodecyl sulfate (SDS), which affects the charge and mobility of the protein, was added following protein assembly (Sommese et al., 2016). This allowed any increase in Cy3 fluorescence of proteins bound to the 30HB rod to be detected (Fig. 10B). Cy3 fluorescence which was normalized to that of a fully assembled sample, prepared by incubating a 20 nM protein with a 30HB rod for 20 min, was used to calculate the binding ratio. The two types of quantitative methods, i.e., mobility shifts of the 30HB rod (Fig. 8) and the increase in Cy3 fluorescence (described here), yielded very similar binding rates (Fig. 10C) as well as k_{on} (2×10^6 M^{-1} s^{-1}) values (Fig. 10D). This result is meaningful from two perspectives: (i) fast assembly of 10K-tagged dimeric kinesin-$SNAP_f$ was confirmed via a different method and (ii) the quantitative method based on the increase in fluorescence of the 30HB rod-bound protein can be used to estimate exact k_{on} values.

The quantitative method was used to examine the effect of a poly-lysine (10K) on kinesin constructs other than the dimeric kinesin-$SNAP_f$ protein. A most intriguing issue was, whether a single peptide of poly-lysine would be sufficient to accelerate assembly, considering that the previously-used protein consisted of two poly-lysine peptides in a dimeric molecule. Thus, a poly-lysine sequence was introduced into a monomeric kinesin-$SNAP_f$ protein which lacked the coiled-coil domain responsible for dimerization. Then, monomeric proteins with or without poly-lysine were purified and labeled using Cy3-NHS. Agarose gel electrophoresis with 0.1% SDS was used to visualize the assembly of Cy3-labeled monomeric kinesin-$SNAP_f$ proteins (Fig. 11, A and B). The k_{on} values estimated for 0K- and 10K proteins were to be 2×10^3 and 6×10^5 M^{-1} s^{-1}, respectively (Fig. 11, C and D). This indicated that a single 10K peptide was

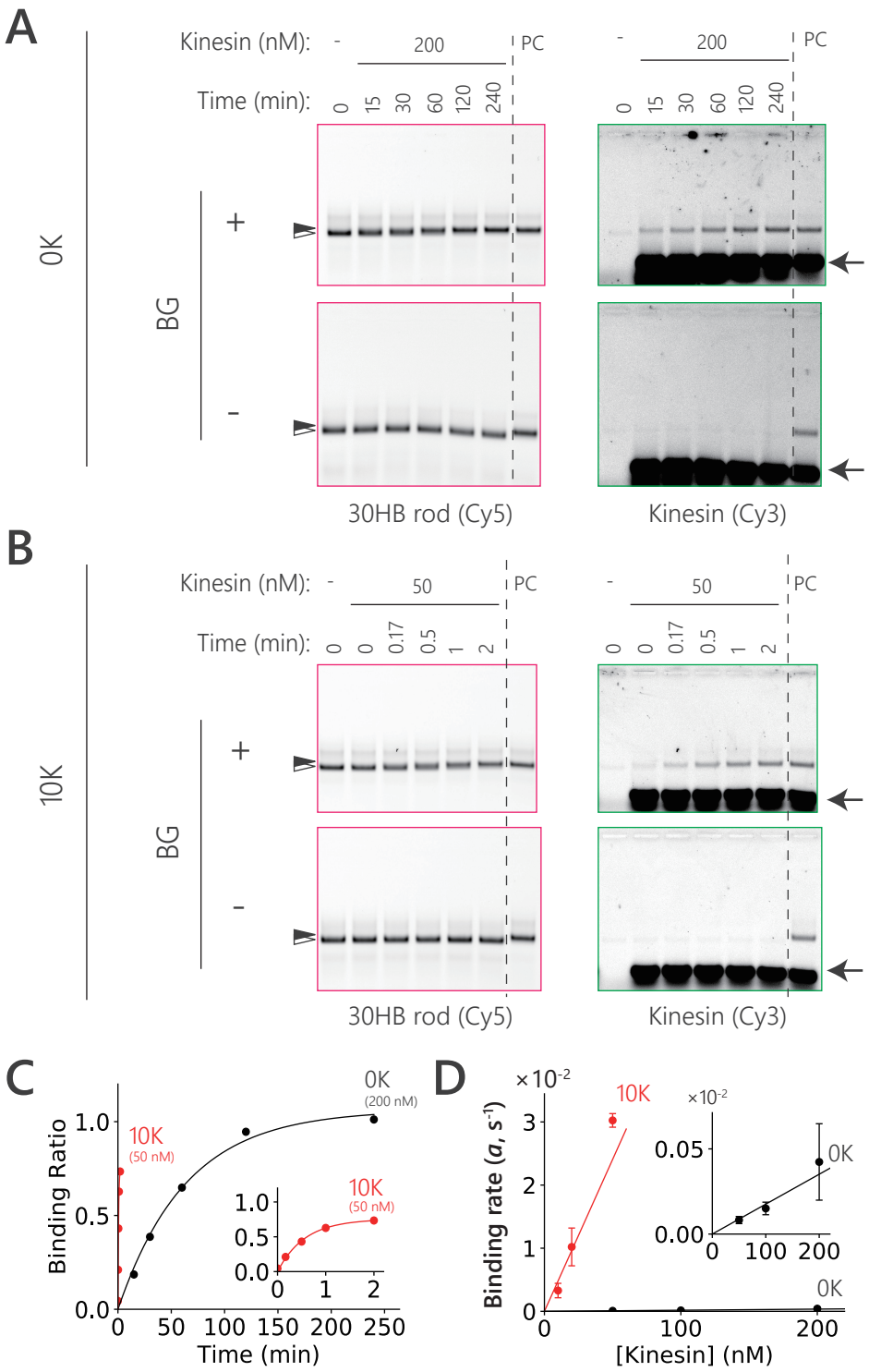

Fig. 11 | Poly-lysine accelerated the assembly of a monomeric kinesin-SNAP$_f$ protein

(A and B) Images of 0.7% agarose gel supplemented with 0.1% SDS. Cy5-labeled 30HB rods and Cy3-labeled monomeric kinesin-SNAP$_f$s were detected via fluorescence. Monomeric kinesin-SNAP$_f$s with or without poly-lysine (10K or 0K, respectively) were labeled with Cy3-NHS and purified. Then, 30HB rods (5 nM) with or without a BG-handle were incubated with Cy3-labeled monomeric kinesins for indicated times; 30HB rods with a BG-handle incubated for 480 min with 200 nM 0K (A) or for 20 min with 50 nM 10K (B) were loaded as a positive control (PC) for -BG samples. Open and filled arrowheads denote free 30HB rods and kinesin-SNAP$_f$ proteins bound BG-30HB rods, respectively. Arrows indicate free monomeric kinesin-SNAP$_f$s. (C) Time-course of binding between Cy3-labeled monomeric kinesin-SNAP$_f$s and BG-attached 30HB rods as determined by the increase in Cy3 fluorescence of 30HB-bound kinesins. Inset, the horizontal axis is re-scaled to 10K. (D) Binding rates were plotted against molar concentrations of Cy3-labeled monomeric kinesin-SNAP$_f$s. Inset, the vertical axis was re-scaled to clearly show the data of 0K. Linear fitting determined the second-order rate constants: 0K, 2×10^3 M^{-1} s^{-1}; 10K, 6×10^5 M^{-1} s^{-1}. Error bars indicate standard deviations of three independent experiments.

sufficient to accelerate the speed of protein assembly on the 30HB rod by a factor of 300. Poly-lysine was also applied to a HaloTag-fused dimeric kinesin protein (kinesin-Halo). Purified and Cy3-labeled dimeric kinesin-HaloTag proteins with or without poly-lysine were assembled onto the 30HB rod containing a ssDNA handle with chlorohexane (CH), which acts as a substrate for HaloTag (Fig. 12, A and B). Although assembly speeds of the HaloTagged proteins were slower than those of $SNAP_f$-tagged proteins, a 10K peptide accelerated the assembly speed by a factor of 10, as indicated by the k_{on} values of 1×10^2 and 1×10^3 M^{-1} s^{-1} for 0K- and 10K HaloTagged proteins, respectively (Fig. 12, C and D). These results show that poly-lysine may also be used with monomeric $SNAP_f$-tagged proteins and HaloTagged proteins.

DNA origami-based complexes were confirmed via single-molecule imaging

Poly-lysine (10K)-based complexes were applied to evaluate collective movements. One interesting issue needing a resolution was whether the layout of motor proteins on a cargo affects its velocity and run length and if so in what manner. To clarify this issue, more than two kinesins were assembled on a DNA origami scaffold and the resulting complexes were analyzed. In this experiment, a square-lattice type DNA origami object with 28-helx bundles (28HB rod) was used (Fig. 2), because it is easier to periodically design the layout of binder modules (e.g., BG) on the flat surface of a square lattice-type DON than on the ragged surface of a honeycomb lattice-type DON. The number of BG-handles were increased to up to 4 to examine the effect of the number and layout of integrated kinesins. Without poly-lysine, a 100 nM dimeric kinesin-$SNAP_f$ protein would be required to fully decorate the 28HB rod with 4 BG-handles (Fig. 13). By contrast, the 10 nM protein with poly-lysine was sufficient for assembly. This indicated that poly-lysine lowered the protein concentrations required for $SNAP_f$-tagged proteins to assemble on a 28HB rod by an order of 10. Therefore, any remaining

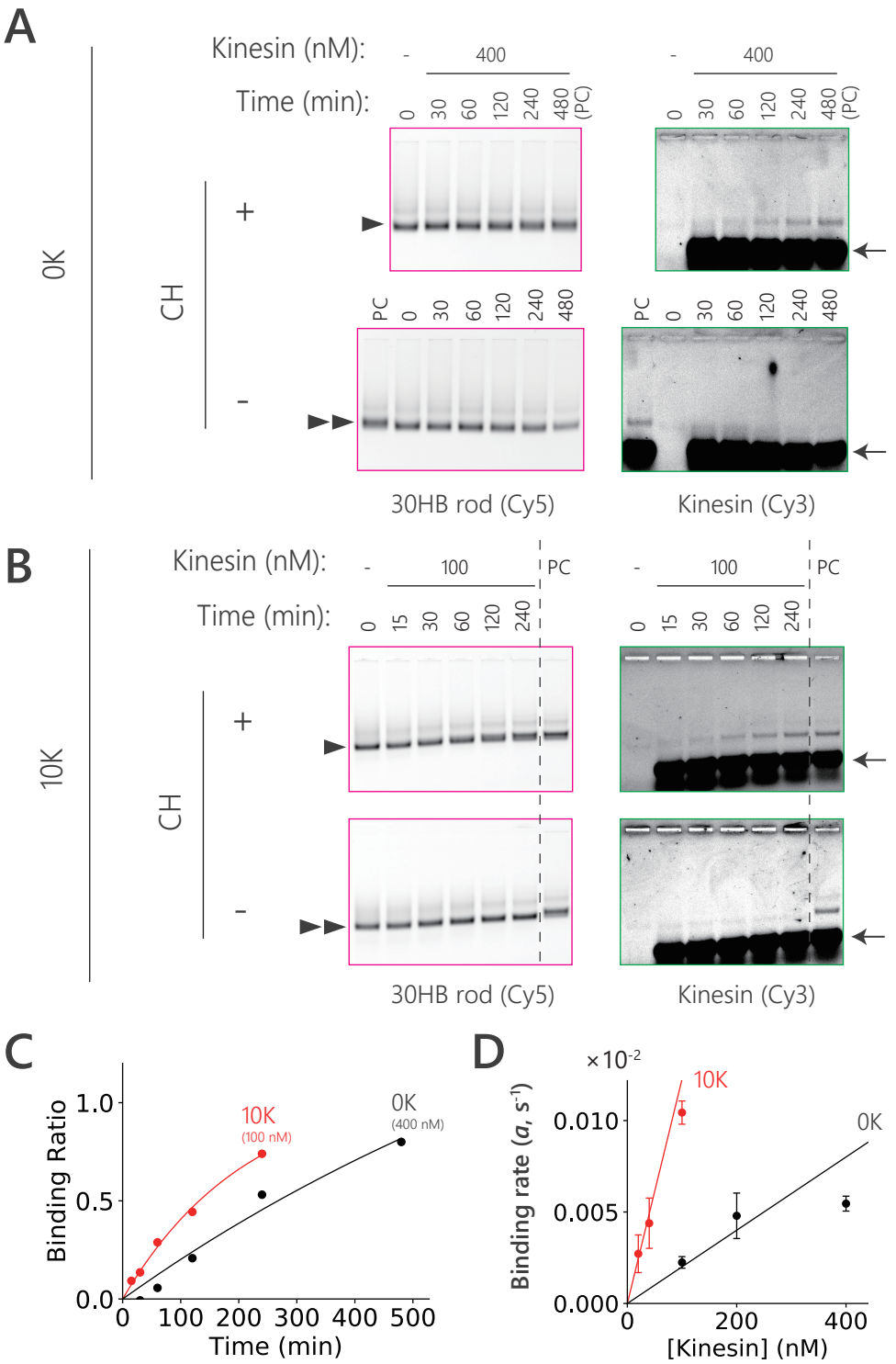

Fig. 12 | Poly-lysine accelerated the assembly of a dimeric kinesin-HaloTag protein

(A and B) Images of 0.7% agarose gel supplemented with 0.1% SDS. Cy5-labeled 30HB rods and Cy3-labeled kinesin-HaloTag proteins were detected via fluorescence. Dimeric kinesin-HaloTag proteins with or without poly-lysine (10K or 0K, respectively) were labeled with Cy3-NHS and purified. Then, 30HB rods (5 nM) with or without a CH-handle were incubated with Cy3-labeled dimeric HaloTagged kinesins for the indicated times; 30HB rods with a CH-handle incubated for 480 min with 400 nM 0K (A) or with 100 nM 10K (B) were loaded as a positive control (PC) for -CH samples. Open and filled arrowheads denote free 30HB rods and kinesin-HaloTag proteins bound CH-30HB rods, respectively. Arrows indicate free kinesin-HaloTag proteins. (C) Time-course of binding between Cy3-labeled dimeric kinesin-Halo and CH-attached 30HB rods as determined by the increase in Cy3 fluorescence of 30HB-bound kinesins. (D) Biding rates were plotted against molar concentrations of Cy3-labeled monomeric kinesin-Halo proteins. fitting determined the second-order rate constants: 0K, 1×10^{2} M^{-1} s^{-1}; 10K, 1×10^{3} M^{-1} s^{-1}. Error bars indicate standard deviations of three independent experiments.

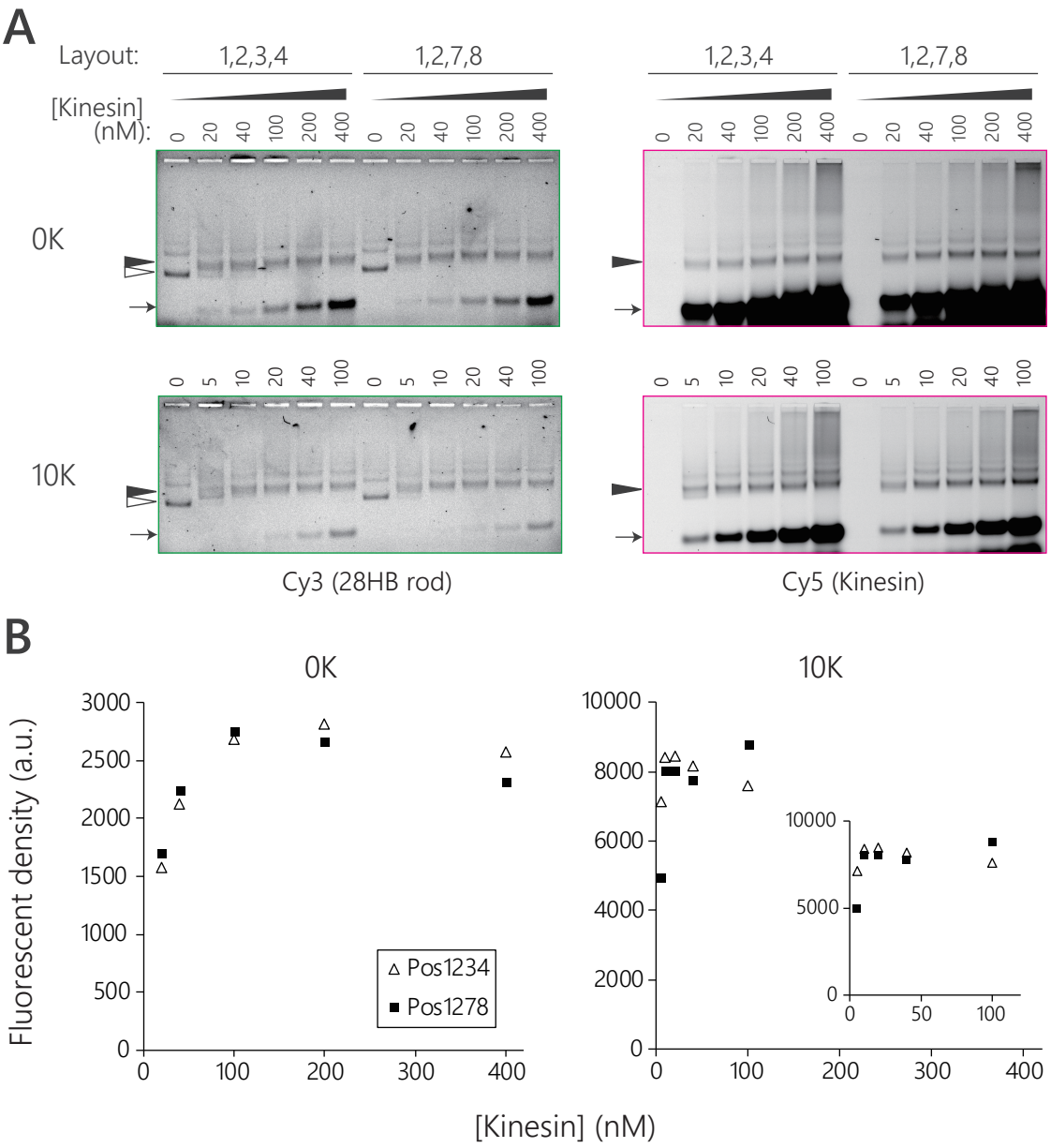

Fig. 13 | Poly-lysine lowered concentration of dimeric kinesin-SNAP$_f$ required for assembly

(A) Images of 0.7% agarose gel supplemented with 0.1% SDS. Cy3-labeled 28HB rods and Cy5-labeled dimeric kinesin-SNAP$_f$-10K were detected using fluorescence. Then, 28HB rods (2 nM) with different layouts of 4 BG-handles were incubated with the proteins for 8 h (0K) or 2 h (10K) at 25°C in 23 mM PIPES (pH 7.0), 0.8 mg/mL casein, 230 mM NaCl, 12 mM $MgCl_2$, 1 mM EGTA, 50 mM ATP and 1 mM DTT. Open and filled arrowheads denote free 28HB rods and kinesin-SNAP$_f$ proteins bound BG-30HB rods, respectively. Arrows indicate free kinesin-SNAP$_f$ proteins. (B) Intensities of Cy3 fluorescence of 28HB-bound kinesins were plotted against the concentration of kinesins. Inset in 10K, the horizontal axis was re-scaled. Maximal amounts of kinesin binding are similar for different layouts with 0K and 10K. By contrast, the required concentration of 10K (10 nM) is 10 times lower than that of 0K (100 nM). Cy5 intensities (kinesins) were corrected using Cy3 intensities (28HB rods). Note that fluorescence intensities of different gels were not calibrated and thus cannot be compared for 0K and 10K.

unincorporated free proteins could be suppressed using poly-lysine. This illustrated the advantage of using poly-lysine for single-molecule imaging, wherein unincorporated free motor molecules may impede movements of complexes (Ibusuki et al., 2020; Seitz and Surrey, 2006; Telley et al., 2009) and obstruct signals that help distinguish a complex from that of unincorporated free motors.

The fluorescent labeling method was optimized since the default NHS labeling method preferentially labels lysines with the poly-lysine sequence, impeding the quantitative assembly of fluorescently labeled proteins. To reduce the effect of fluorescent labeling on the assembly, dimeric kinesin-SNAP$_f$-10K labeled with a low molar ratio BG-conjugated A647 dye was used. This system resulted in partially labeled dimeric kinesin-SNAP$_f$-10K proteins, on which one or both SNAP$_f$ of dimeric kinesin-SNAP$_f$-10K would be occupied by the A647 dye while the rest remained vacant and thus free to bind to BG-attached 28HB rods (Fig. 14, left).

The assembly of fluorescently labeled dimeric kinesin-SNAP$_f$-10K was evaluated at a single-molecule level using a photobleaching assay. First, 28HB rods with different numbers of BG-handles were incubated with protein and the resulting complexes were purified multiple times using size-exclusion spin columns (Fig. 14). The complexes were then immobilized on axonemes with AMP-PNP, an ATP analog which is not hydrolyzed by kinesin. Using this scheme, particles immobilized on axonemes could be successfully visualized (Figs. 15 and 16). More than 80% of these complexes reflected single step photobleaching of a fluorophore attached to the 28HB rod, indicating that minimal aggregation has taken place on the 28HB rod. Only particles with single step photobleaching of the 28HB rod were used to analyze photobleaching stages of a fluorophore attached to kinesin (A647). As expected, the number of photobleaching steps involved in the kinesin channel increased with numbers of BG-handles on the 28HB rod. A binominal distribution fitted to the histogram of the photobleaching step

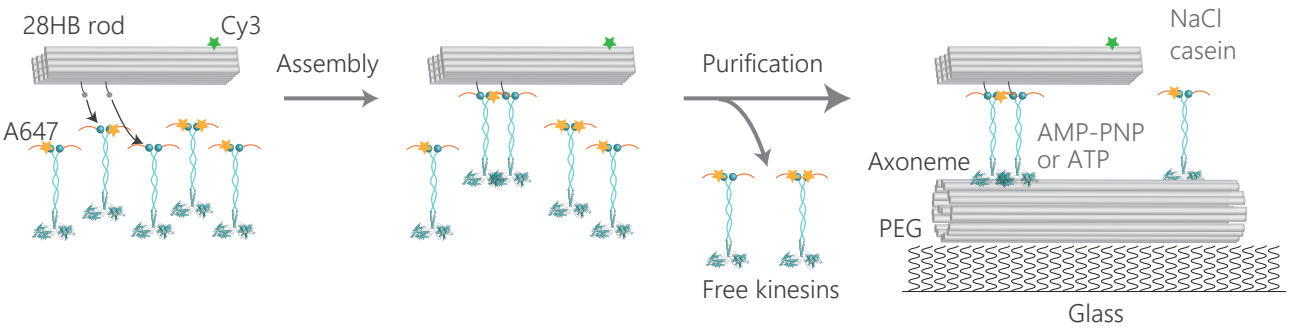

Fig. 14 | Single-molecule imaging of a 28HB rod-based transporter

Schematic showing fabrication and observation of a kinesin-bound transporter. The dimeric kinesin-SNAP$_f$-10K protein labeled with A647 was incorporated into a Cy3-labeled 28HB rod and purified using columns. The sample was infused into a flow cell in which axonemes were adsorbed on PEG-coated glass surface and the transporter was visualized using a TIRF microscope, under the presence of AMP-PNP or ATP.

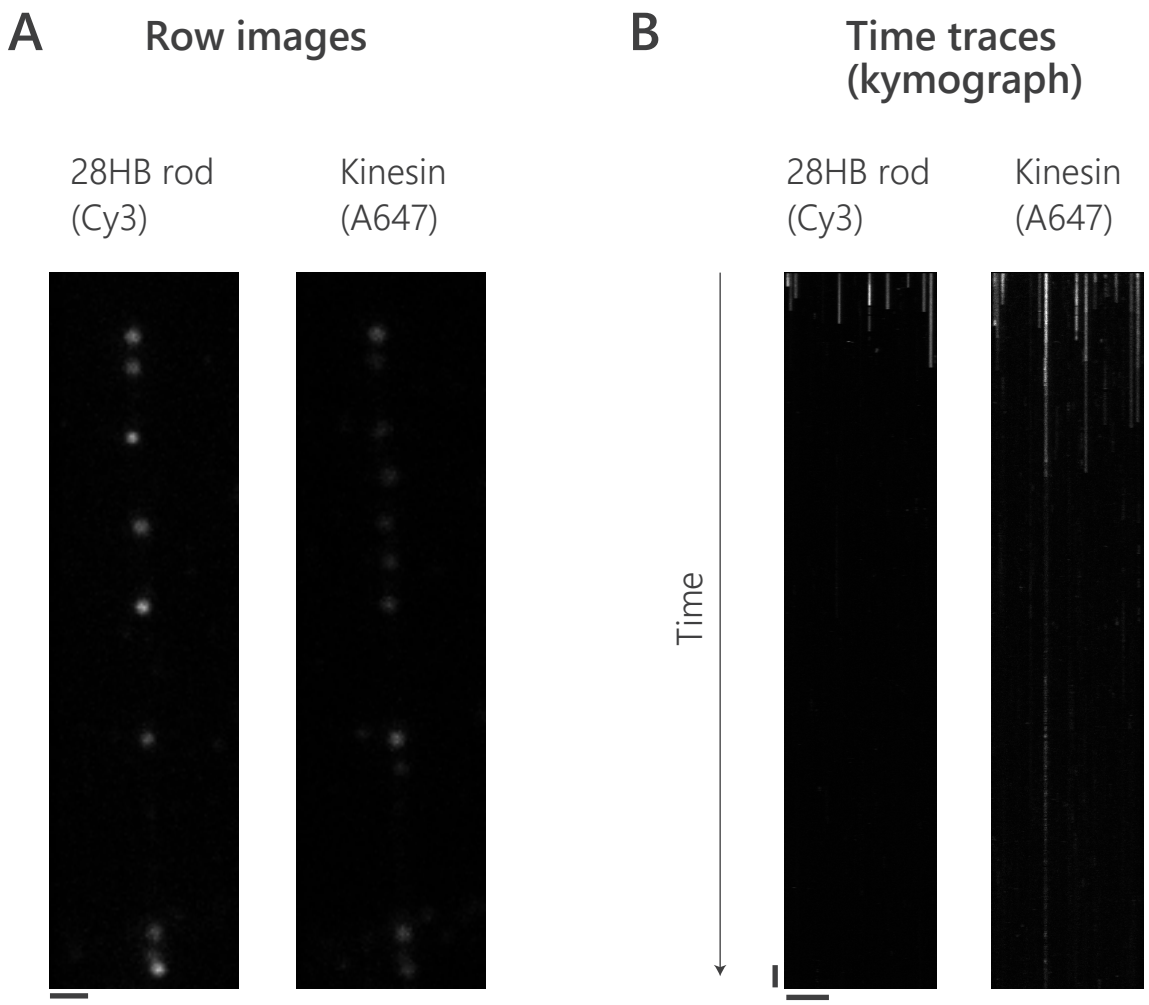

Fig. 15 | Photobleaching assay of transporters immobilized on an axoneme

(A) Row fluorescence images of 28HB rod (Cy3) and kinesin (A647) channels. Cy3-labeled 28HB rod with 4 BG-handles ("1,3,5,7" layout) bound to A647-labeled kinesin-$SNAP_f$-10K were attached to an axoneme with 2 mM AMP-PNP and 50 mM NaCl, and illuminated with two lasers (532 and 633 nm). Most 28HB rod particles showed kinesin (A647) fluorescence whereas several free-kinesin particles without 28HB rod (Cy3) fluorescence were remained. Scale bar, 1 μm. (B) Time traces of Cy3 and A647 fluorescence on the axoneme in (A), showing photobleaching of immobilized transporters. Scale bars: vertical axis, 10 s; horizontal axis, 5 μm.

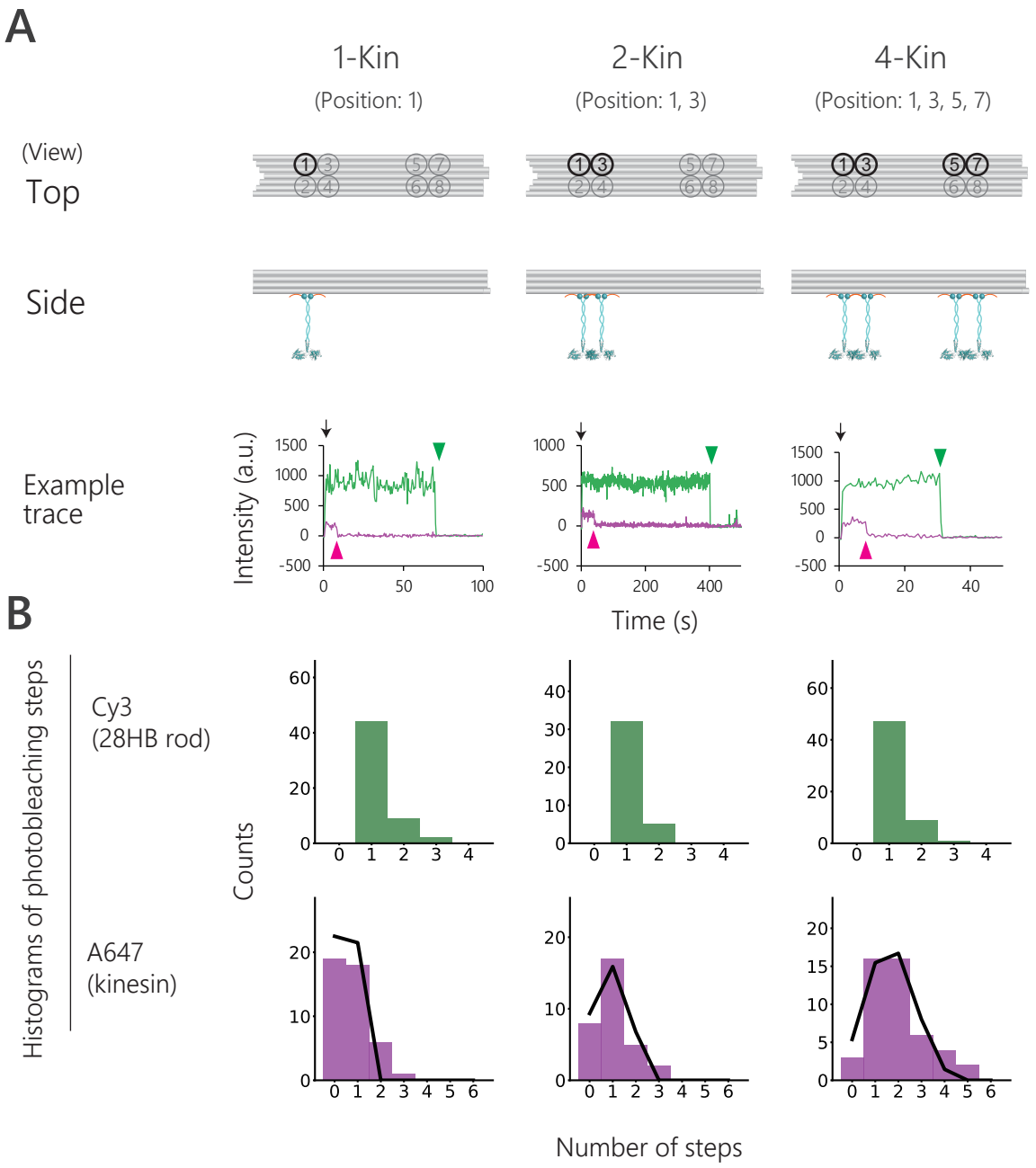

Fig. 16 | Photobleaching assays confirmed incorporation of kinesin molecules onto 28HB rods

(A) Schematic of transporters and typical time-traces of single step photobleaching of individual transport complexes. Cy3-labeled 28HB rods with 1, 2, or 4 BG-handle(s) bound to A647-labeled kinesin-SNAP$_f$-10K were immobilized on axonemes and illuminated a few seconds after starting image capture (arrows). Green and magenta arrowheads indicate photobleaching of Cy3 (28HB rod) and A647 (kinesin), respectively. (B) Histograms of photobleaching step numbers of Cy3 (28HB rod, top) and A647 (kinesin, bottom). For A647, data of particles with one step Cy3 photobleaching were used. Occupancy fractions of A647-kinesin and number of A647-kinesin per site were estimated using a two-step process. First, A647 photobleaching step data were fitted with binomial distribution (solid lines) and estimated to be 0.49, 0.46, and 0.42 for 1, 2, and 4 BG-handle(s), respectively. Because 28HB rods without kinesin do not bind to axonemes, data for 1 BG-handle may be considered as reflecting a DNA rod occupied with 1 kinesin (kinesin occupancy = 1). Therefore, the occupancy fractions of kinesin of 2- and 4-BG handles were converted from A647-dye occupancy data, and estimated to be 0.94 and 0.86, respectively.

number, indicated that the occupancy fractions of kinesin per handle for the two- and four-handle transporters were 0.94 and 0.86, respectively. The failure of the occupancy fractions to reach 1 (100% construction yield) may be attributed to the defective incorporation of staples into a DON, as previously suggested (Strauss et al., 2018).

Properties of these complexes were also examined in the presence of ATP. Single-molecule imaging showed transporters [i.e., particles showing the Cy3 (28HB rod) signal] moving along axonemes (Fig. 17). By contrast, no signals were observed when 28HB rods without a BG-handle were used (Fig. 18), indicating that visualized transporters were complexes formed via BG-$SNAP_f$ linkage. For the purpose of examining the effect of protein numbers on transporter motility, the following four parameters were obtained from transporters moving along axonemes: fluorescent intensity of the 28HB rod channel (Cy3); fluorescent intensity of the protein channel (A647); velocity; and run length. Fluorescent intensity of the kinesin channel increased with the number of BG-handles, whereas that of the 28HB rod channel was less affected (Fig. 19). This result was consistent with that of immobilized particles analyzed via the photobleaching assay (Fig. 16). Velocities remained constant (Fig. 20, A and B) among DON-based transporters ($P \geq 0.05$, one-way ANOVA). On the other hand, the run length increased with the number of BG-handles among the transporters (Fig. 20, C and D; $P < 0.001$, Kruskal–Wallis test). This result confirmed those of previous studies which linked kinesin-1 via another rod-shaped DON (Derr et al., 2012), a 20–100-bp DNA scaffold (Feng et al., 2018; Furuta et al., 2013; Rogers et al., 2009), single α helix polypeptide (Norris et al., 2014), bead (Beeg et al., 2008), or a quantum dot (Seitz and Surrey, 2006). These results confirmed that the desired complexes were formed and could be used in single-molecule imaging experiments.

DNA origami-based experimental system showed that the layout of kinesins affects the

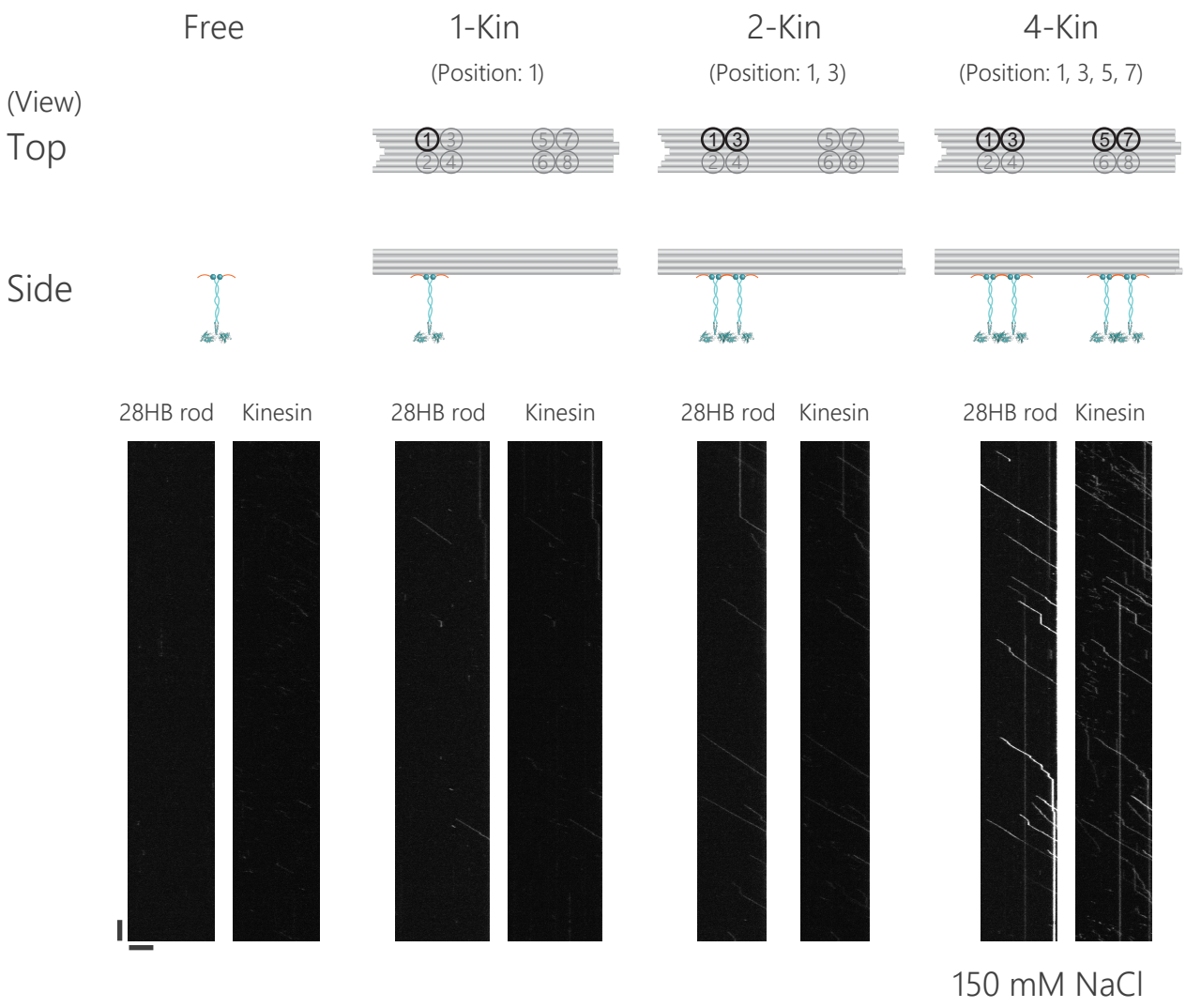

Fig. 17 | Single-molecule imaging of transporters containing different numbers of dimeric kinesins

Schematic of transporters (top) and kymographs showing movements on axonemes (bottom). The A647-labeled dimeric kinesin-SNAP$_f$-10K protein was integrated onto Cy3-labeled 28HB rods with 1, 2 or 4 molecule(s) of BG and visualized on axonemes. Free dimeric kinesin was also visualized as a comparison. Scale bars: vertical axis, 10 s; horizontal axis, 5 μm. The assay was performed with 150 mM NaCl.

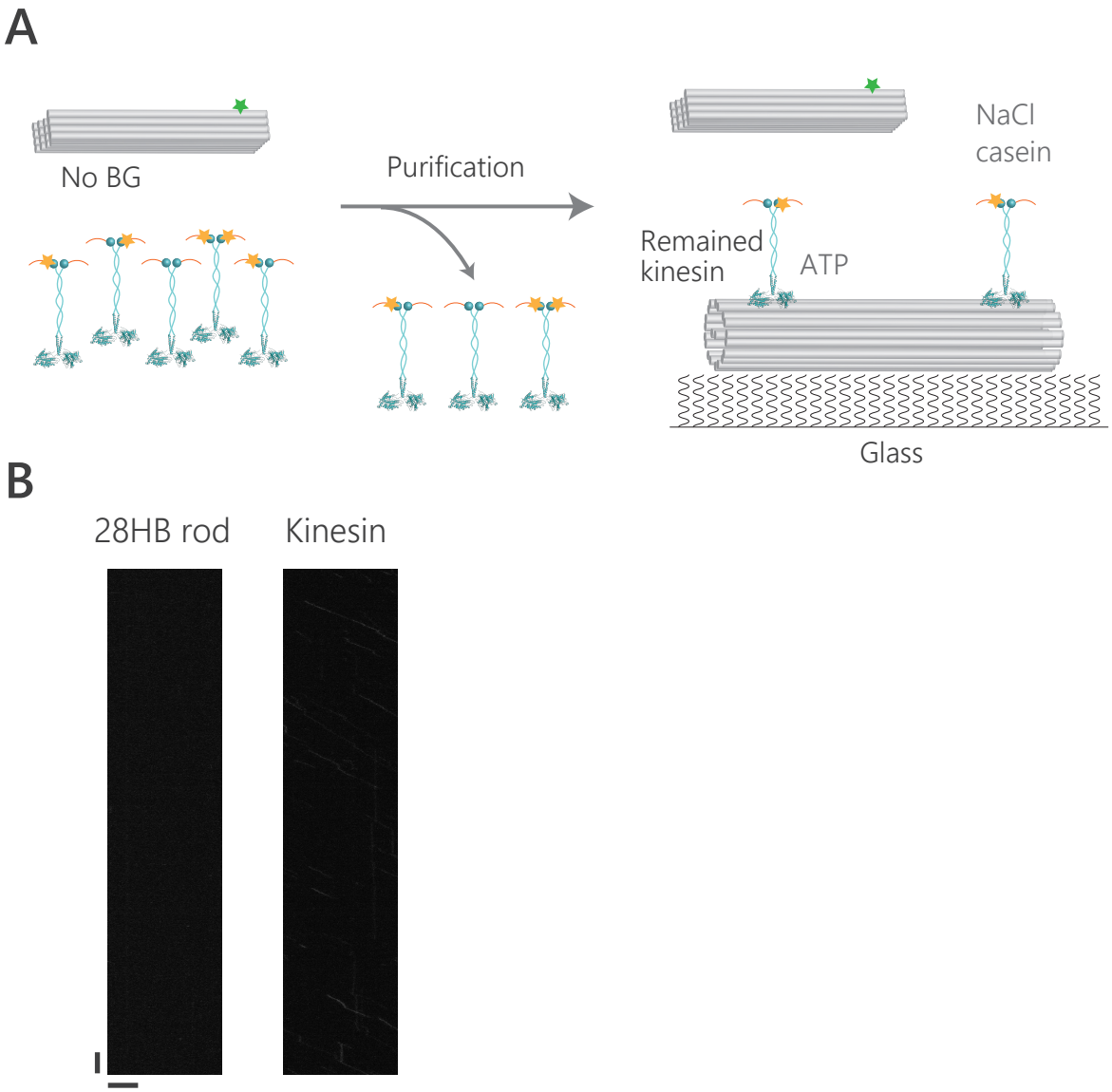

Fig. 18 | No movement was observed for the BG-less 28HB rod

(A) Schematic showing an experiment using 28HB rods without BG. The dimeric kinesin-SNAP$_f$-10K labeled with A647 was incubated with the Cy3-labeled 28HB rod and purified using columns same as Fig. 14. The sample should contain 28HB rods and free kinesins which was not removed completely. (B) Representative kymographs showing Cy3 and A647 fluorescence on an axoneme. No 28HB rod (Cy3) signal was observed whereas free remaining kinesins moved along the axoneme: scale bars: vertical axis, 10 s; horizontal axis, 5 µm.

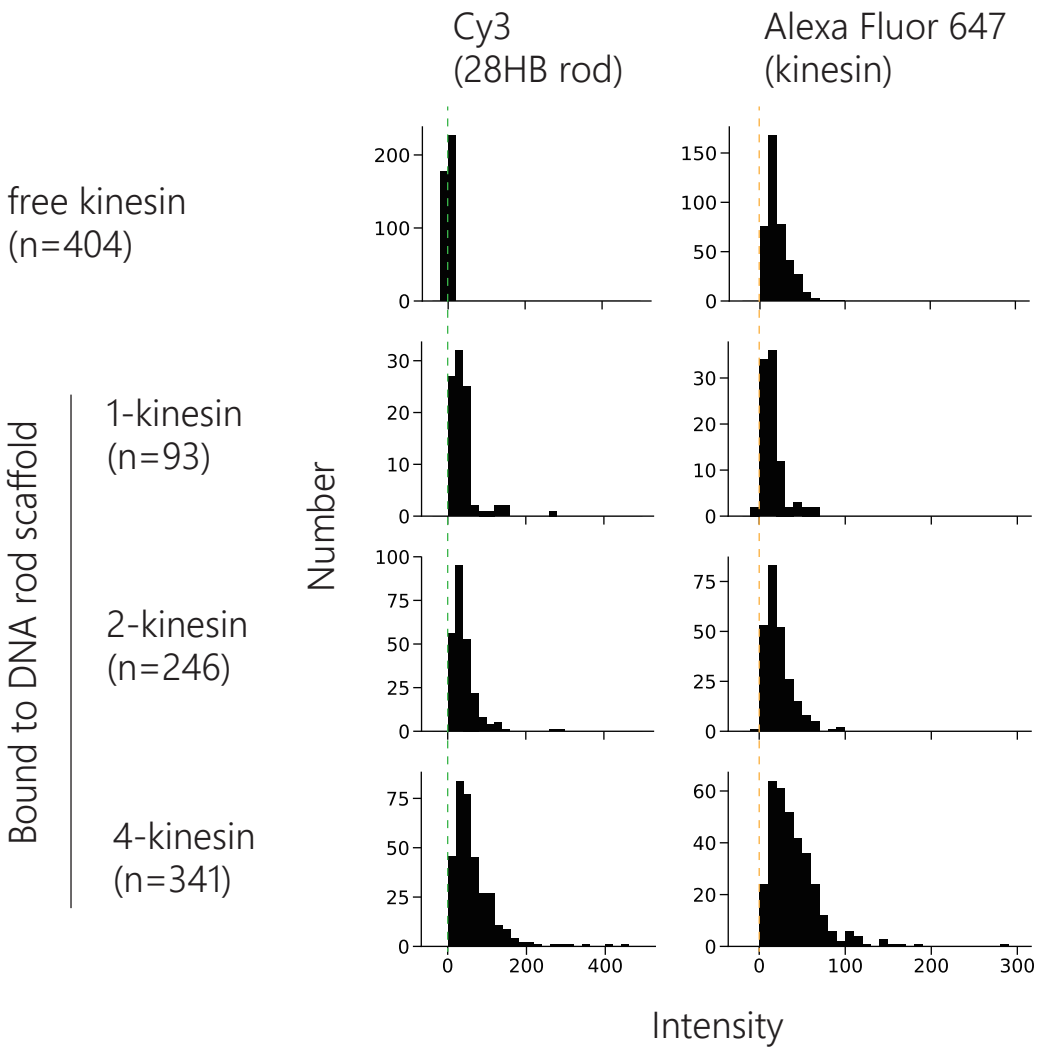

Fig. 19 | Fluorescence intensity of kinesin increased with the number of BG on the transporter

Fluorescence intensity distributions of transport complexes moving along an axoneme. The transporters were prepared with Cy3-labeled 28HB rods with different numbers of BG and A647-labeled kinesin-$SNAP_f$-10K. Free kinesin showed A647- but not Cy3-signaling.

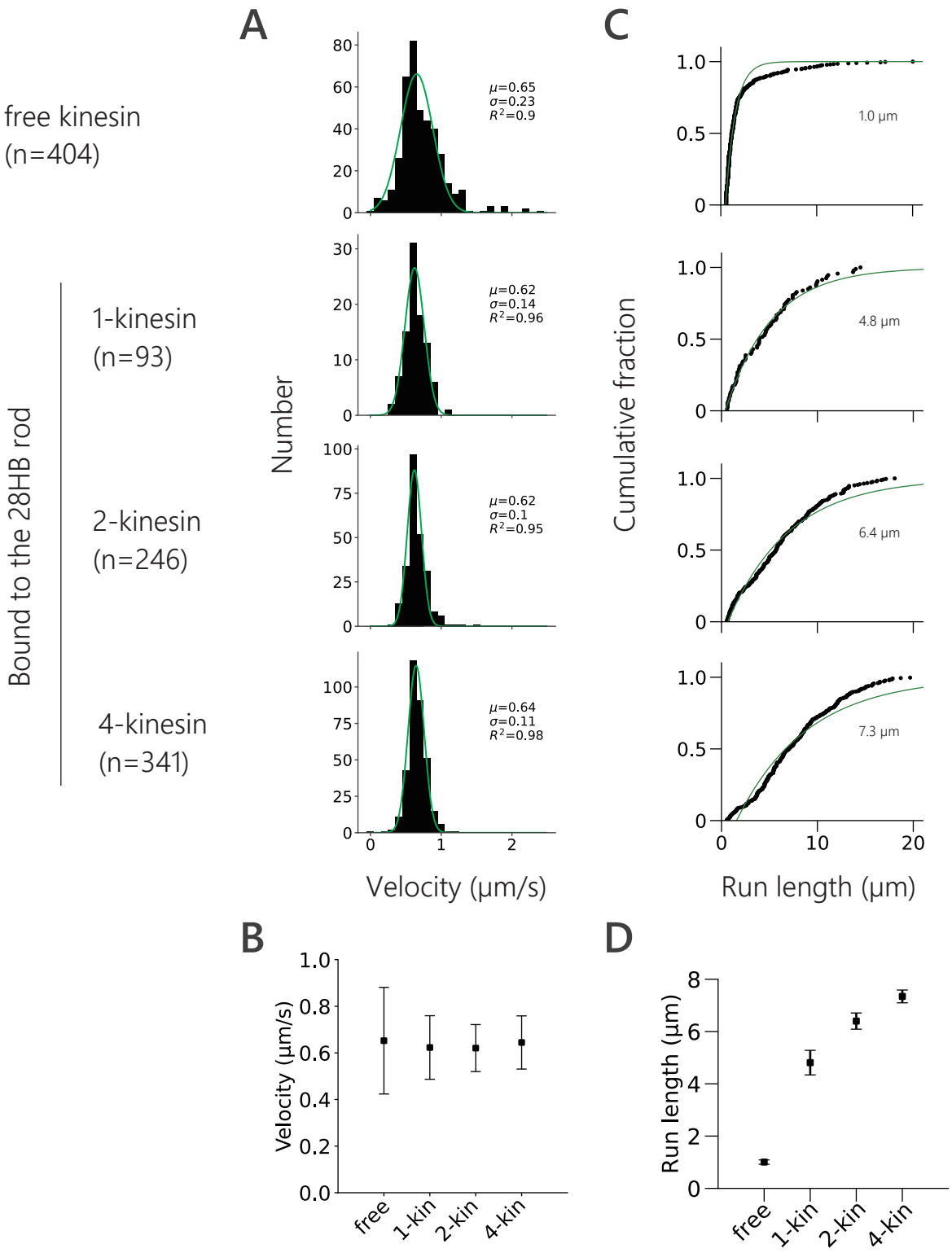

Fig. 20 | The number of dimeric kinesins affects run length but not velocity

Analyses of free kinesin and transporters containing 1, 2 and 4 kinesin(s). (A and B) Histograms (A) and a scatter plot (B) of velocities. The plots (μ) and error bars (σ) in (B) were determined by fitting the histograms in (A) with a Gaussian function. (C and D) CDFs (C) and a scatter plot (D) of run lengths. The plots in (D) were determined by fitting the CDFs in (C) with a single-exponential function and error bars were estimated via bootstrap sampling. Note that the assay was performed with 150 mM NaCl.

processivity

To evaluate whether the layout of kinesin molecules affects the motility and if so in what manner, 28HB rods with different layouts of kinesins were prepared and the movements on axonemes were visualized. First, I examined transporters with 4 kinesins, indicating that 4 BG-handles were incorporated into the 28HB rod (up to 4 molecules of the dimeric kinesin-SNAP$_f$-10K protein can be integrated with one rod) in three different layouts as follows: four kinesins located at the corners of a 7–10 nm rectangle ("1,2,3,4;" Fig. 21, top); two sets of two kinesins separated by 66 nm ("1,2,7,8"); or four kinesins located on a straight line ("1,3,5,7"). Under previous ionic conditions (Fig. 17; 150 mM NaCl), many transporters with 4 kinesins reached the edges of axonemes or fields of view. During observation, ionic strength was optimized, long runs were suppressed in order to accurately evaluate run lengths of these transporters, and movements were observed under 250 mM NaCl conditions (Fig. 21, bottom). The 28HB rods (Cy3) and kinesins (A647) of the three different layouts exhibited similar fluorescent intensities (Fig. 22), indicating that similar numbers of kinesins were incorporated into these complexes. These complexes showed similar velocities (Fig. 23, A and B; $P \geq 0.05$, one-way ANOVA). By contrast, run lengths were different; the transporter on which 4 kinesins were located in a small (7–10 nm) rectangle (the "1,2,3,4" layout) showed a significantly shorter run lengths (Fig. 23, C and D; $P < 0.001$, Kruskal–Wallis test; $P<0.001$, when compared to "1,2,3,4" and another layout, Conover–Iman test).

To explore the minimum number of kinesins with layouts that affect motility, I prepared transporters with 2 kinesins in three different layouts, wherein dimeric kinesins were located either 8-10 nm apart on the shorter axis ("1,2;" Fig. 24, top), incorporated 7 nm apart on the longer axis ("1,3"), or separated by 66 nm on the longer axis of the 28HB rod ("1,7"). Movement was observed under conditions involving 210 mM NaCl (Fig. 24, bottom). The

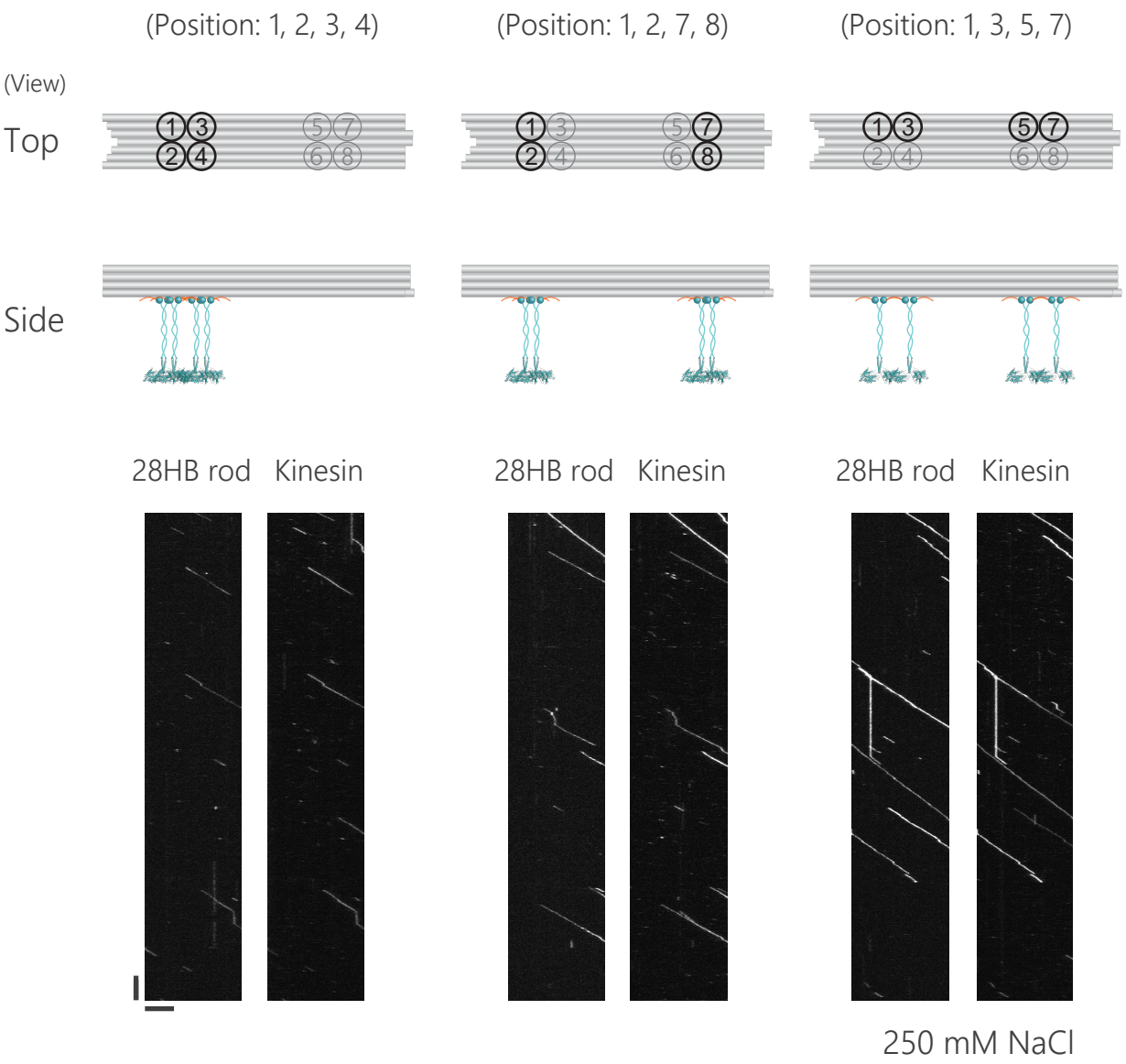

Fig. 21 | Single-molecule imaging of transporters containing 4 dimeric kinesins with different layouts

(Top) Schematic of transporters. (Bottom) Kymographs showing movements on axonemes. A647-labeled dimeric kinesin-SNAP$_f$-10K was integrated onto Cy3-labeled 28HB rods with 4 molecules of BG in the illustrated layouts. Scale bars: vertical axis, 10 s; horizontal axis, 5 µm. The assay was performed with 250 mM NaCl.

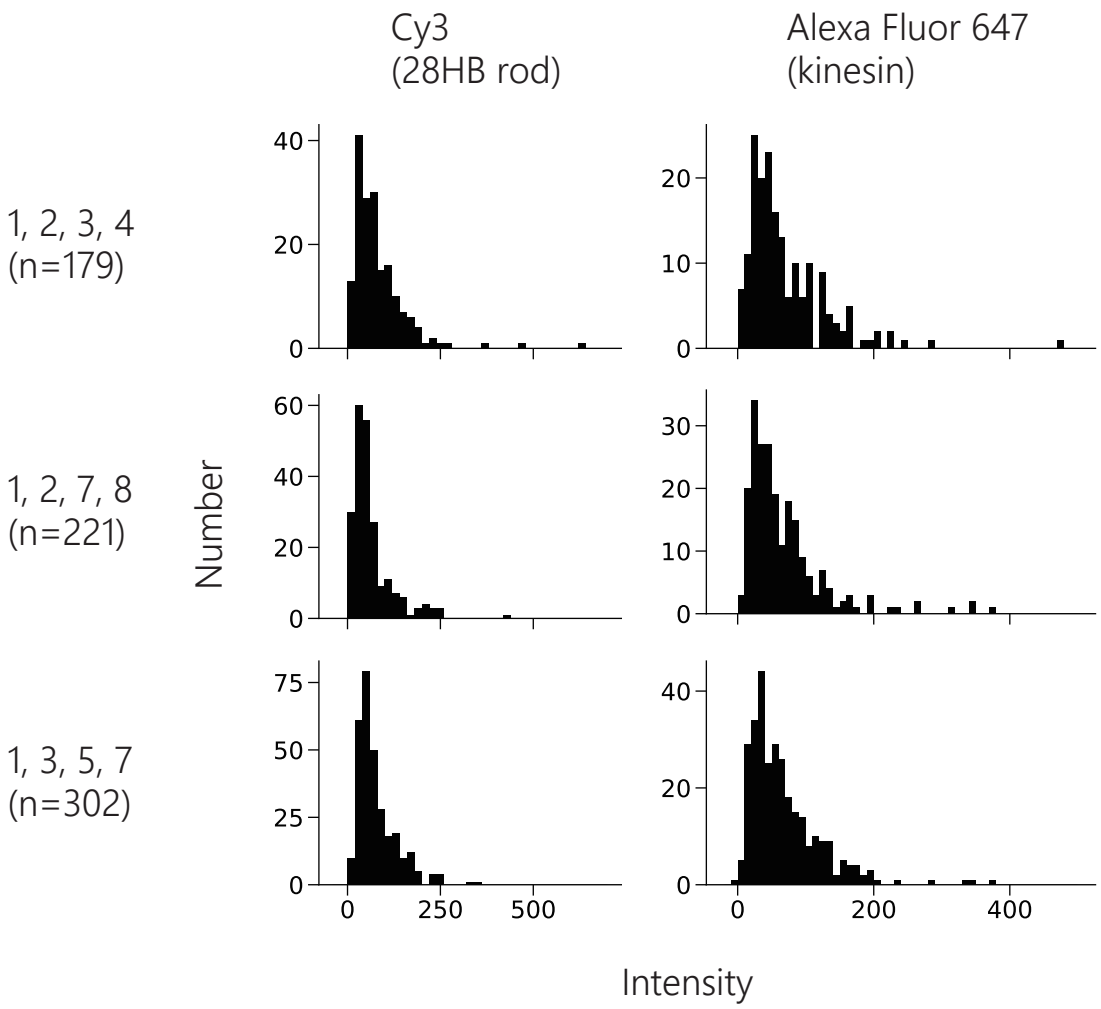

Fig. 22 | Similar fluorescence intensities were observed in three-types of transporters with 4 dimeric kinesins

Fluorescence intensity distributions of transporters moving along axonemes, which contained 4 dimeric kinesins with different layouts.

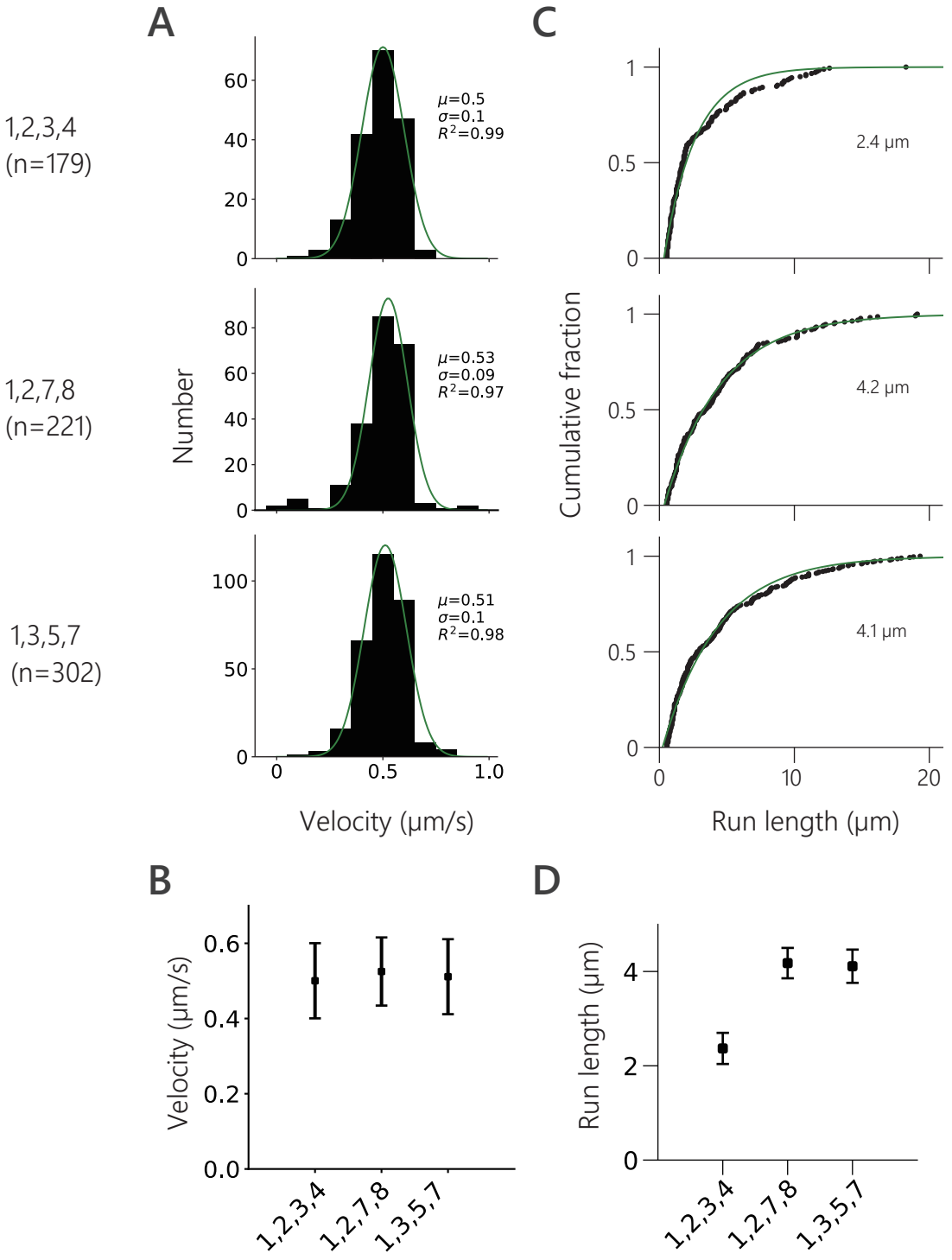

Fig. 23 | The layout of 4 dimeric kinesins affected the run length but not velocity

Analyses of transporters containing 4 dimeric kinesins with different layouts. (A and B) Histograms (A) and a scatter plot (B) of velocities. The plots (μ) and error bars (σ) in (B) were determined by fitting the histograms in (A) with a Gaussian function. (C and D) CDFs (C) and a scatter plot (D) of run lengths. The plots in (D) were determined by fitting the CDFs in (C) with a single-exponential function and error bars were estimated by bootstrap sampling. Note that the assay was performed with 250 mM NaCl.

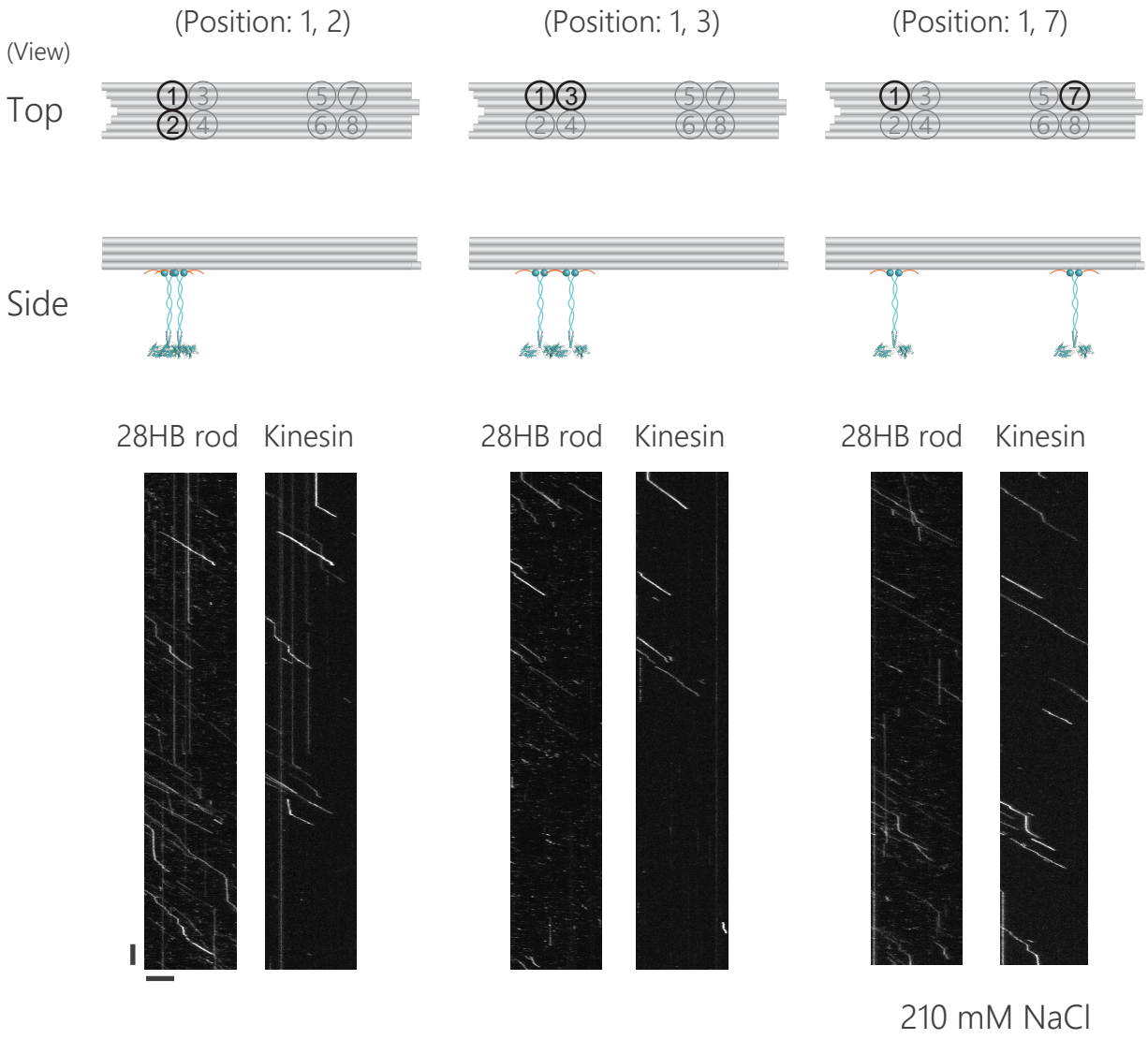

Fig. 24 | Single-molecule imaging of transporters containing 2 dimeric kinesins with different layouts

(Top) Schematic of transporters. (Bottom) Kymographs showing movements on axonemes. A647-labeled dimeric kinesin-SNAP$_f$-10K was integrated onto Cy3-labeled 28HB rods with 2 molecules of BG in the illustrated layouts. Scale bars: vertical axis, 10 s; horizontal axis, 5 µm. The assay was performed with 210 mM NaCl.

fluorescent intensities corresponding to the three different layouts of transporters were similar (Fig. 25), indicating that similar numbers of kinesins were incorporated onto these complexes. All three types of transporters with 2 kinesins showed similar velocities; although these groups showed a statistical difference ($P < 0.001$, one-way ANOVA), the differences in the mean velocities (~0.03 μm s^{-1}) were too small compared with the mean values (0.55–0.58 μm s^{-1}) and error levels (SD, 0.08–0.10 μm s^{-1}; Fig. 26, A and B). On the other hand, the run lengths were different ($P < 0.05$, Kruskal-Wallis test) with the transporter with two kinesins separated by 66 nm showing a significantly longer run length (Fig. 26, C and D; "1,2-1,7," $P < 0.01$; "1,3-1,7," $P < 0.05$; Conover-Iman test). The results corresponding to the 4- and 2-kinesin-occupied transporters suggested that spatial proximity of dimeric kinesins had decreased the processivity of the transporters but exerted only a little effect on velocity.

Finally, I examined the movements of transporters on which the monomeric kinesin-$SNAP_f$-10K was assembled. Although a monomeric kinesin itself does not move processively, complexes of more than two monomeric kinesins linked with a DON (Miyazono, 2017) or a short DNA molecule (Miyazono et al., 2010) reportedly showed processive movement. Similar to the results of dimeric kinesins, transporters with proximal monomeric kinesins exhibited shorter run lengths in the cases of both 2- (Figs. 27 and 28; $P < 0.05$, Kruskal–Wallis test; $P < 0.05$ between "1,7" and another layout, Conover–Iman test) and 4- (Figs. 29 and 30; $P < 0.05$, Conover–Iman test) monomeric kinesins. On the other hand, velocities of these transporters with monomeric kinesins were also mildly affected. The spatial proximity of monomeric kinesins decreased the velocity of both transporters (2-kin, Figs. 28, $P < 0.001$, one-way ANOVA and Tukey's test; 4-kin, Fig. 30, $P < 0.01$, Tukey's test). Notably, different velocities were obtained from the "1,2" and "1,3" transporters on which monomeric kinesins were located 8-10 nm apart on the shorter axis ("1,2") and 7 nm apart on the longer axis ("1,3"). These

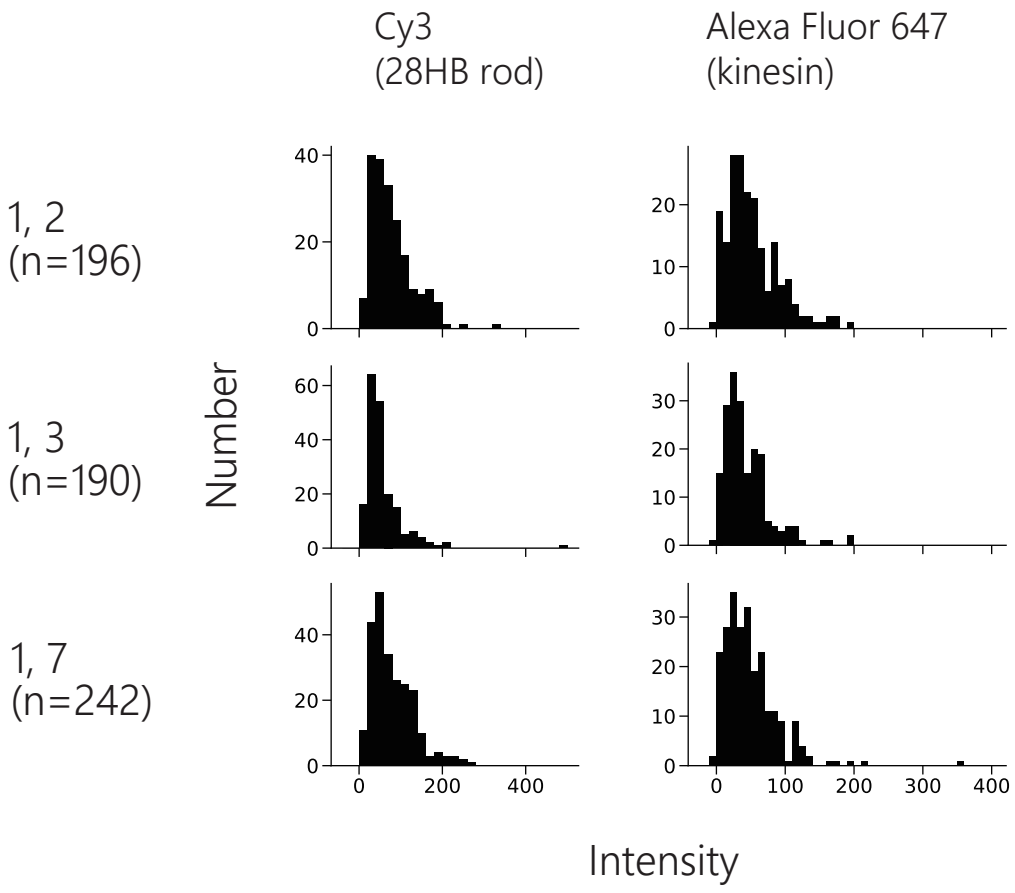

Fig. 25 | Similar fluorescence intensities were observed in three-types of transporters with 2 dimeric kinesins

Fluorescence intensity distributions of transporters moving along axonemes, which contained 2 dimeric kinesins with different layouts.

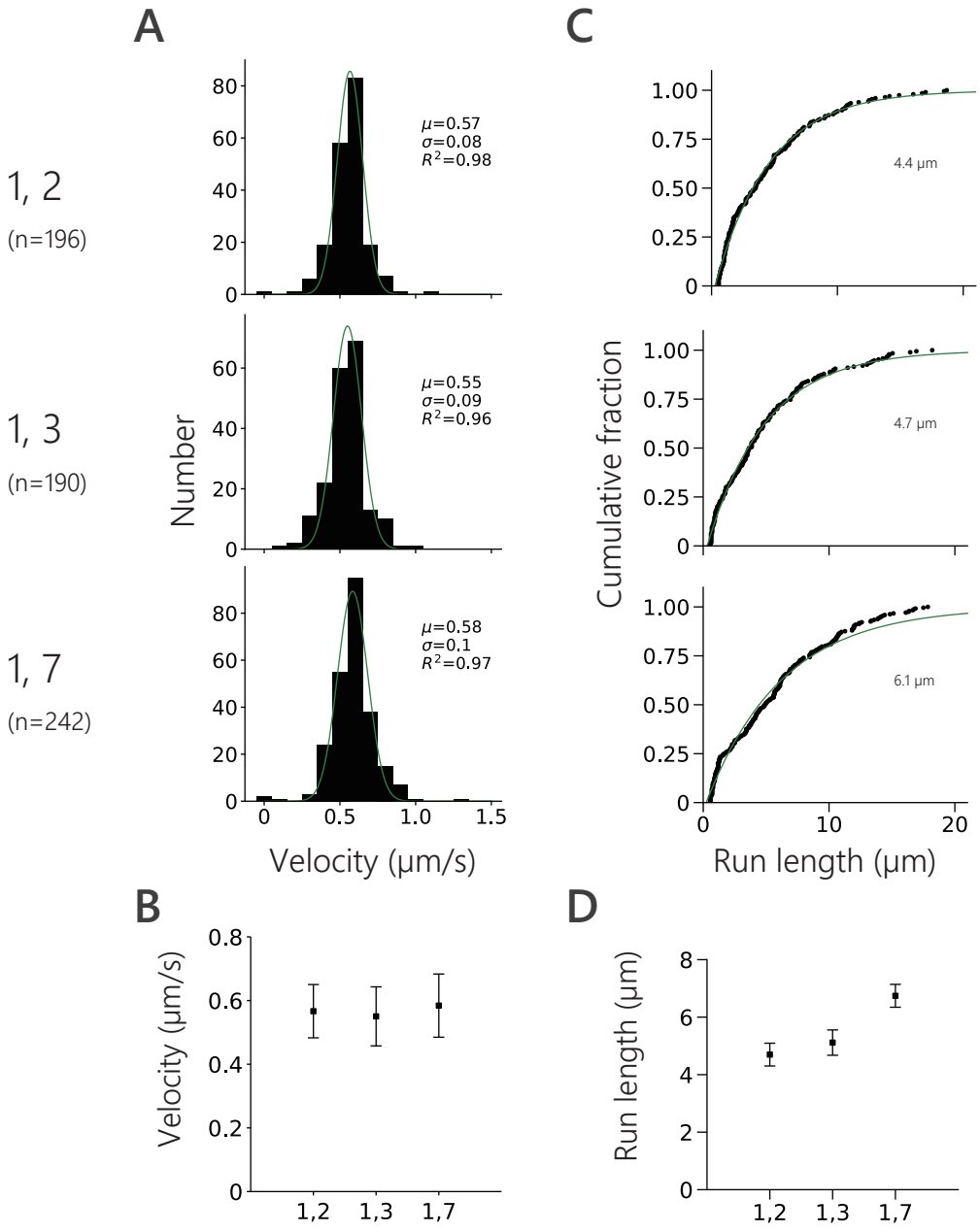

Fig. 26 | The layout of 2 dimeric kinesins affected the run length but had little effect on the velocity

Analyses of transporters containing 2 dimeric kinesins with different layouts. (A and B) Histograms (A) and a scatter plot (B) of velocities. The plots (μ) and error bars (σ) in (B) were determined by fitting the histograms in (A) with a Gaussian function. (C and D) CDFs (C) and a scatter plot (D) of run lengths. The plots in (D) were determined by fitting the CDFs in (C) with a single-exponential function and error bars were estimated by bootstrap sampling. Note that the assay was performed with 210 mM NaCl.

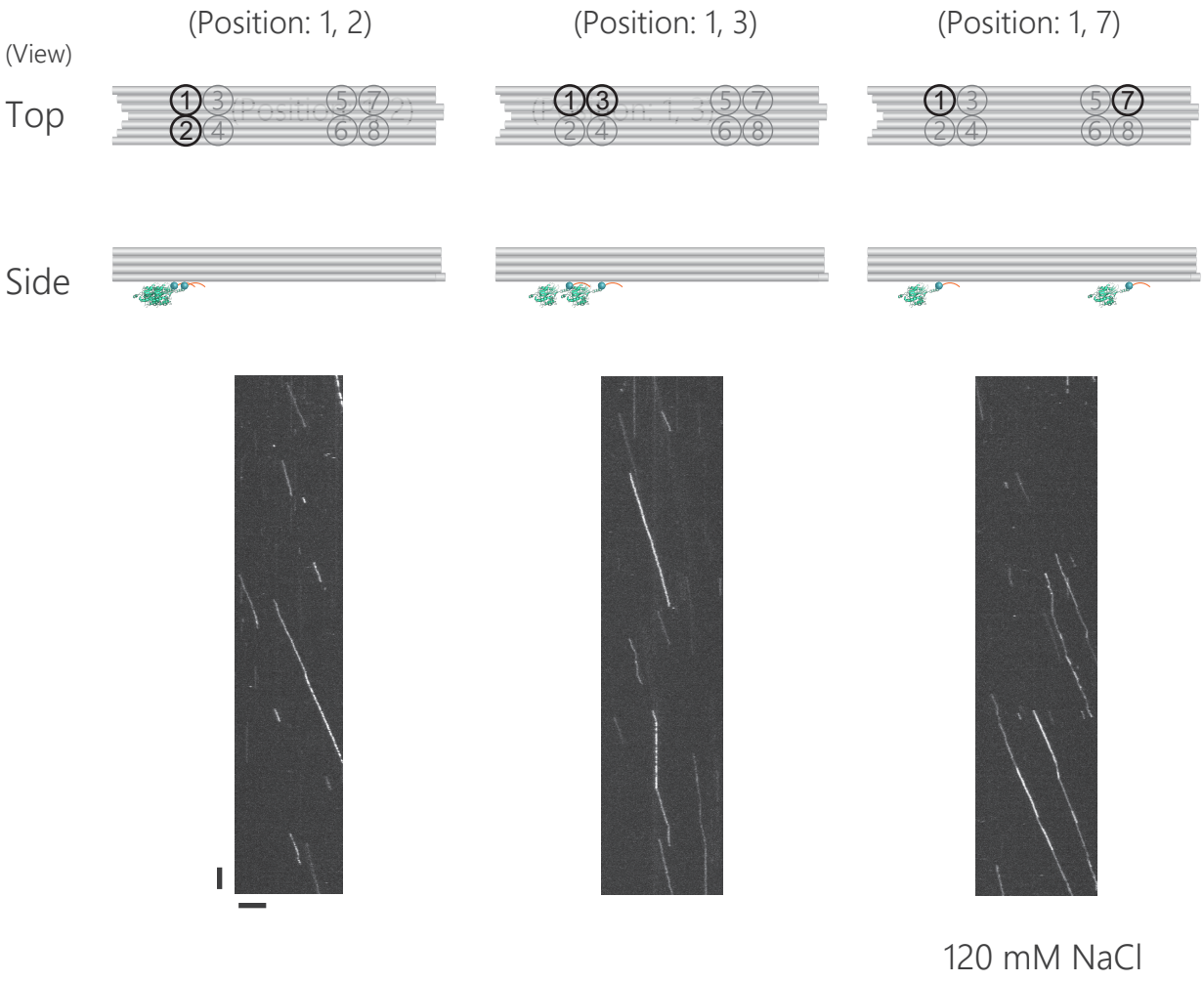

Fig. 27 | Single-molecule imaging of transporters containing 2 monomeric kinesins with different layouts

(Top) Schematic of transporters. (Bottom) Kymographs showing movements on axonemes. The monomeric kinesin-SNAP$_f$-10K was integrated onto Cy3-labeled 28HB rods with 2 molecules of BG in the illustrated layouts. The transporters were tracked by the Cy3 (28HB rod) fluorescence. Scale bars: vertical axis, 10 s; horizontal axis, 5 μm. The assay was performed with 120 mM NaCl.

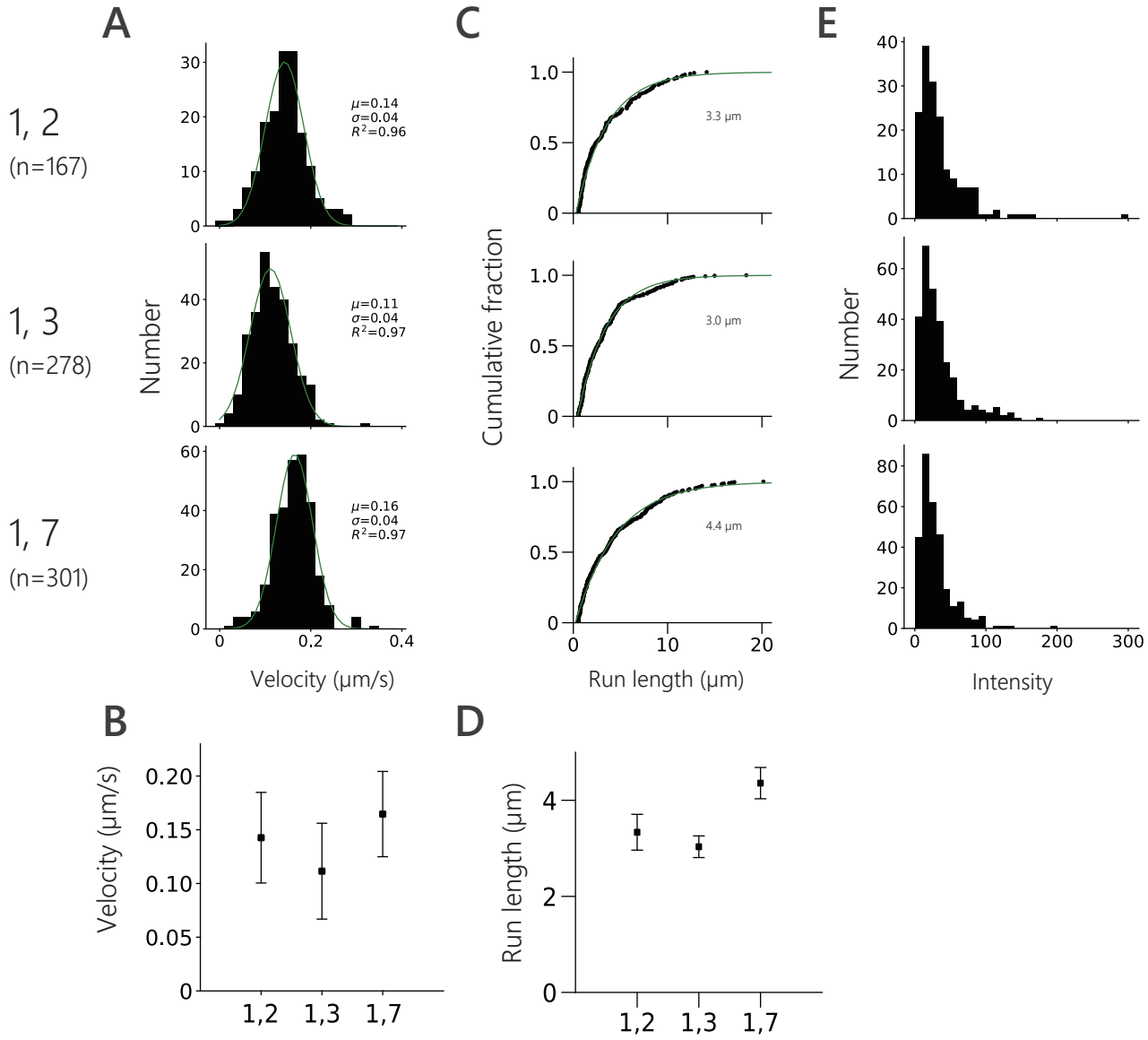

Fig. 28 | The layout of 2 monomeric kinesins affected the motility

Analyses of transporters containing 2 monomeric kinesins with different layouts. (A and B) Histograms (A) and a scatter plot (B) of velocities. The plots (μ) and error bars (σ) in (B) were determined by fitting the histograms in (A) with a Gaussian function. (C and D) CDFs (C) and a scatter plot (D) of run lengths. The plots in (D) were determined by fitting the CDFs in (C) with a single-exponential function and error bars were estimated by bootstrap sampling. (E) Histograms of Cy3 (28HB rod) intensities. Note that the assay was performed with 120 mM NaCl.

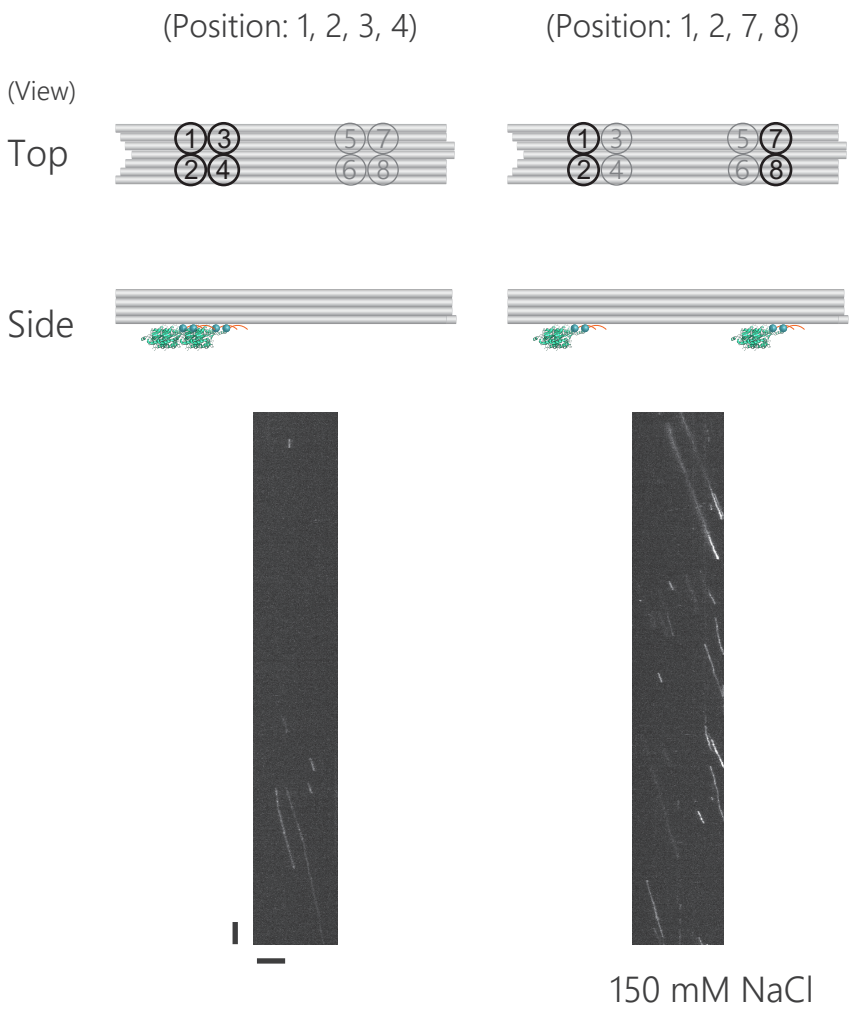

Fig. 29 | Single-molecule imaging of transporters containing 4 monomeric kinesins with different layouts

(Top) Schematic of transporters. (Bottom) Kymographs showing movements on axonemes. The monomeric kinesin-SNAP$_f$-10K was integrated onto Cy3-labeled 28HB rods with 4 molecules of BG in the illustrated layouts. The transporters were tracked by the Cy3 (28HB rod) fluorescence. Scale bars: vertical axis, 10 s; horizontal axis, 5 μm. The assay was performed with 150 mM NaCl.

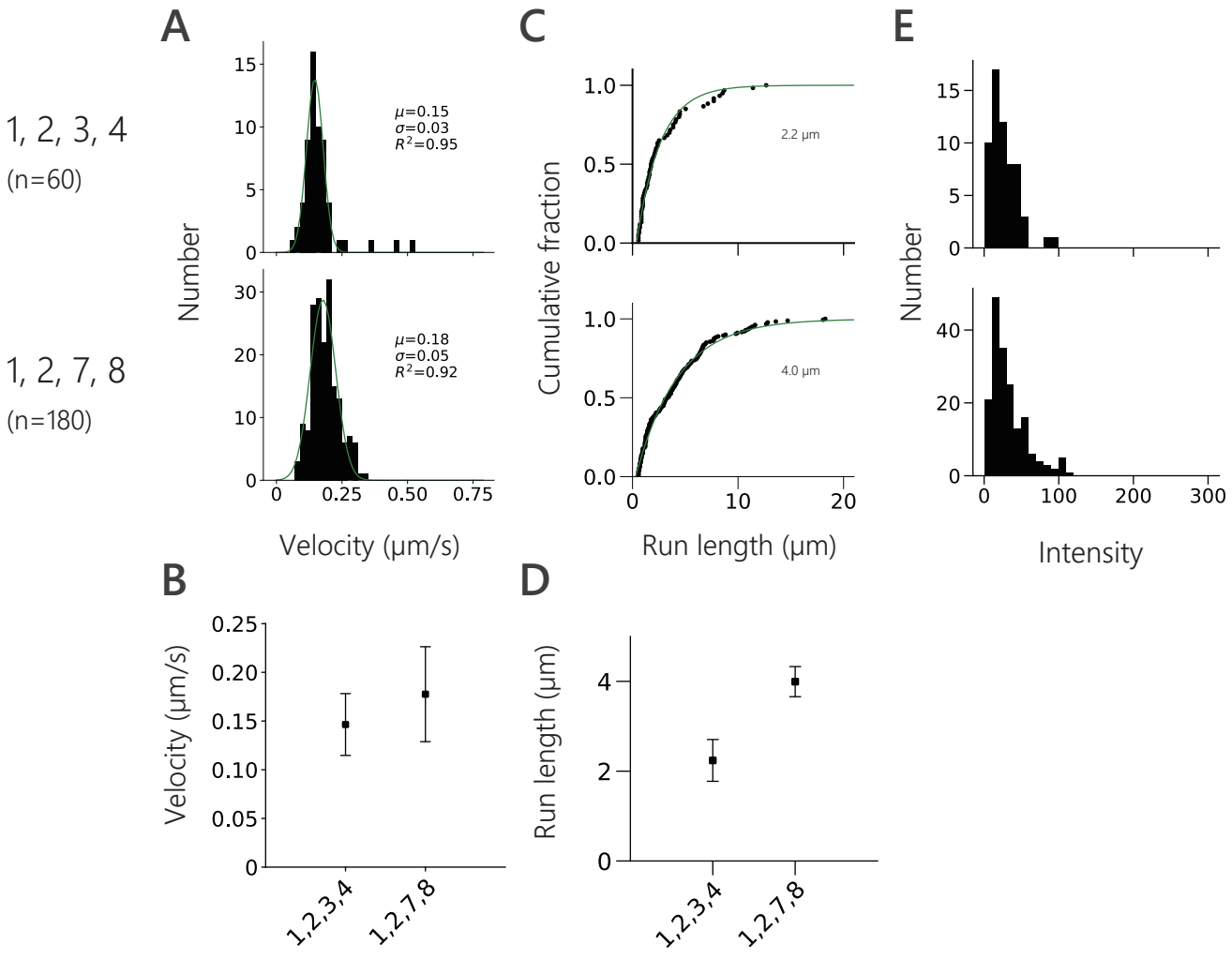

Fig. 30 | The layout of 4 monomeric kinesins affected the motility

Analyses of transporters containing 4 monomeric kinesins with different layouts. (A and B) Histograms (A) and a scatter plot (B) of velocities. The plots (μ) and error bars (σ) in (B) were determined by fitting the histograms in (A) with a Gaussian function. (C and D) CDFs (C) and a scatter plot (D) of run lengths. The plots in (D) were determined by fitting the CDFs in (C) with a single-exponential function and error bars were estimated by bootstrap sampling. (E) Histograms of Cy3 (28HB rod) intensities. Note that the assay was performed with 150 mM NaCl.

results indicate that the layout of monomeric kinesins may affect processivity and, possibly, velocity.

I-4. Discussion

In this part, I proposed a method that can be utilized to integrate a POI with a DON showing a high binding rate and demonstrated that the collective movement of kinesins may show potential for use as a biological application. The poly-lysine of 10K significantly accelerated the speed of $SNAP_f$-tagged protein assembly on rod-shaped DONs. Poly-lysine could be applicable to dimeric $SNAP_f$-tagged proteins, monomeric $SNAP_f$-tagged proteins and HaloTagged proteins, indicating the versality of the poly-lysine approach. The improvement in assembly speed enabled the construction of DNA origami-based transporters with defined numbers and layouts of kinesin molecules. The quality of transporters at a single-molecule level was confirmed using a TIRF microscope. Thus, this new experimental system showed that spatial proximity of kinesin molecules may negatively affect motility, particularly run length.

Advantages of the poly-lysine-based assembly method

In contrast to the frequently-used DNA hybridization method (Niemeyer, 2010), the assembly approach I reported in this part capitalizes on advantages conferred by a self-ligating protein tag system (Saccà et al., 2010), such as covalent bond formation, as well as the unnecessity of chemical modification or the incorporation of relatively-small-sized tags (2–3 nm in size for $SNAP_f$-tag). In addition, the higher kinetics associated with irreversible covalent bond formation can reduce the POI concentration required for assembly on DONs (Figs. 9 and 13). This becomes meaningful when analyzing a DON-incorporated POI due to the following reasons; when the binding kinetics are slow, an excess of POI and/or a long incubation time are

required for POI assembly. However, high concentrations of POI may result in side effects such as the aggregation of DONs (Fig. 9). Long incubation may also lead to deactivation, aggregation and/or degradation of POIs and the DONs. By contrast, the fast, covalent binding accelerated by poly-lysine may yield expected complexes with a lesser POI concentration and a shorter incubation time. Lessening the amount of excess POI needed for assembly also facilitates the purification of POI-assembled complexes from free POI. Versality of poly-lysine is also supported by the fact that poly-lysine used in the current study consists of only ten amino acid residues and exerts no negative effects on either $SNAP_f$ folding (Fig. 4) or POI activity (kinesin motility; Figs. 5 and 6). Although $SNAP_f$-poly-lysine system is now limited to assembling only one type of protein ($SNAP_f$-tagged POI), this limitation may be addressed by combining poly-lysine with the DNA binding domain-conjugated approach developed by Morii's grope (Nguyen et al., 2017).

The consecutive length of poly-lysine may be critical for the $SNAP_f$-tag-based protein assembly

The length of poly-lysine affects the speed of protein assembly on a rod-shaped DON (DNA rod). A previous study has shown that poly-L-lysine causes DNA compaction and that increasing the number of lysine residues from 3-mer to 9-mer accelerated by a factor of $> 10^4$ (Akitaya et al., 2007). Similarly, the results of the current experiment indicated that ten-lysine remarkably accelerated the speed of conjugation between dimeric kinesin-$SNAP_f$ protein and the DNA rod (700-fold), whereas 5K exerted a much lesser effect (only 3-fold; Fig. 8). Significance of the consecutive ten-lysine sequence was also indicated by the results which showed that the monomeric kinesin-$SNAP_f$-10K protein bound to the DNA rod 30-times faster (6×10^5 M^{-1} s^{-1}; Fig. 11) than the dimeric kinesin-$SNAP_f$-5K protein (2×10^4 M^{-1} s^{-1}; Fig. 8),

despite the number of lysine residues introduced per protein molecule being the same. Considering the results reported by Akitaya et al. which indicated that changing the number of lysine residues from 3 to 9-mer affected the efficiency of DNA compaction by four orders of magnitude (Akitaya et al., 2007), it was surmised that not only the global charge (pI) of the POI but also the absolute length of poly-lysine would be critical for ensuring efficient interactions between POIs and DNA-based nanostructures as also for accelerating POI assembly speed.

Notably, the assembly speed of monomeric kinesin-SNAP$_f$-10K on the DNA rod was higher than that of SNAP$_f$ with low-molecular BG derivatives (< 10^5 /M/s) (Sun et al., 2011). This suggests that the binding rate was no longer limited by the reactivity of SNAP$_f$ itself and that the rate-limiting issues specific to assembly on DONs could be mostly resolved. Further development of protocols that improve integration of ligand-conjugated ssDNA-handles on DONs may help more increase the yield of POI-assembled complexes even further.

HaloTag-based protein assembly

The 10-fold acceleration of the assembly of HaloTagged dimeric protein with 10K (Fig. 12), was still lesser than that corresponding to the SNAP$_f$-based assembly system (700-fold, Fig. 8). This may be due to the following factors: (i) the electric charge near poly-lysine (-8, -5 and +5 at pH 7.4 for Halo-10K, SNAP$_f$-0K and SNAP$_f$-10K, respectively) estimated by an isoelectric point calculator (Kozlowski, 2016) was correlated with the assembly speed on the DNA rod; (ii) the geometrical position of C-terminals (the sites where poly-lysine was introduced) causes the distance between the C-terminal and the active site in the SNAP$_f$-tag (Mollwitz et al., 2012) to be shorter than the distance between them in HaloTag (Liu et al., 2017). Therefore, the speed of HaloTagged POI-assembly on DONs may be advanced by introducing poly-lysine into the N-terminal, which is relatively closer to the active site of HaloTag. An advanced type of HaloTag

developed by Niemeyer's group (Koßmann et al., 2016) also showed a high potential for improving the binding kinetics. Further improvement of assembly methods using a HaloTag and/or other self-ligating proteins, such as SpyCatcher (Kröll et al., 2022), indicating that using multiple self-ligating protein tags simultaneously may help us better understand the collective function of more than two different POIs.

The essences of single-molecule imaging data

The latter sections of this part focus on the measurement of the movements of DNA origami-based transporters containing defined numbers and layouts of dimeric and monomeric kinesins. Single-molecule imaging data showed the following results: (i) increasing the number of dimeric kinesins enhanced run lengths but not velocities (Fig. 20); (ii) spatial proximity of dimeric kinesins decreased run lengths but hardly affected velocities (Figs. 23 and 26); (iii) 2D arrangement of two dimeric kinesins did not affect motility (Figs. 24 and 26); (iv) spatial proximity possibly affected not only the run lengths of monomeric kinesins but also their velocities (Figs. 28 and 30); and (v) transporters with different 2D arrangements of monomeric kinesins showed different velocities (Figs. 27 and 28).

Although previous studies have focused on the collective movement of kinesins, whether a layout of defined numbers of kinesins affects motility, and if so, in what manner, remains unclear. Such a lack of clarity is attributed to the difficulties associated with applying stoichiometric to the assembly of motor proteins on DONs, as well as heterogeneity in the numbers of assembled motors, which affects motility, which may interfere with the interpretation of experimental data. The poly-lysine-based assembly system enabled efficient construction of DNA origami-based transporters (Fig. 13) and the low contamination of free kinesin allowed confirmation of kinesin-assembly via fluorescence (Figs. 16, 19, 22, and 25).

This confirmed that kinesins exhibited similar occupancy patterns among different-layout transporters with the same number of BG-handles (Figs. 22 and 25, right panels). Thus, the technological improvement achieved by the current study enabled the molecular layout to be accurately analyzed and allowed its effect to be distinguished from that of the motor number.

Interpretation of single-molecule imaging data compared with previous studies

Findings of several studies that investigated dimeric kinesin motilities using kinesin-1 may be interpreted as follows.

(i) The effects exerted by a given number of dimeric kinesins were consistent with those reported by previous studies using a DON (Derr et al., 2012), a 20–100-bp DNA molecule (Feng et al., 2018; Furuta et al., 2013; Rogers et al., 2009), or another scaffold (Beeg et al., 2008; Norris et al., 2014; Seitz and Surrey, 2006).

(ii) The context of spatial proximity of dimeric kinesins is deemed to be associated with obstacles on axonemes that are formed by other kinesin molecules bound to the same DNA origami scaffold, which possibly obstruct movement. Surrey's group proposed that excess amounts of kinesins on microtubules may decreased run length more than velocity (Telley et al., 2009), which substantiates my results. Gliding assays, in which unanchored microtubules were transported by kinesin bound to a glass surface supplemented with kinesin molecules, have linked spatial proximity to the density of kinesins. Previous reports have shown that the gliding velocities of microtubules remained largely un-affected by densities up to 1,000–5,000 molecules μm^{-2} of kinesins with a coiled-coil domain attached to glass surfaces (Bieling et al., 2008; Howard et al., 1989), due to loose mechanical interference. In spite of the highly-packed layouts used in this study (e.g., 4 kinesins were located within 7–10 nm, 4 molecules per approximately 70 nm^{-2} at the anchor points), it is assumed that the effect of kinesin density on

velocity is weakened as kinesin molecules spread outside the anchor points on the DNA rod.

(iii) Similar motilities were observed among “1,2” and “1,3” transporters with dimeric kinesins located on the shorter and longer axes of the 28HB rod, respectively. This may be attributed to translational and rotational diffusion. Although information regarding diffusion constants of the 28HB rod appears to be lacking, several studies have shown that translational and rotational diffusion constants of similar-sized gold nanoparticles may range between 6–7 $\mu m^2\ s^{-1}$ and 2–4 ms^{-1}, respectively (Berger Bioucas et al., 2019; Feller et al., 2021). This indicates that the 28HB rod itself diffuses approximately 80 nm and 100° (2 radian), while a kinesin, on average, walks 0.6 nm on an axoneme (1 ms, calculated using a velocity of 0.6 $\mu m\ s^{-1}$), suggesting that rotational diffusion may cause the arrangement between a 28HB rod and an axoneme to be disordered. This hypothesis should be verified in future studies. Further advances in DNA origami nanotechnology may lead to the preparation of larger structures with well-defined layouts (Ibusuki et al., 2022; Wagenbauer et al., 2017) which may enable a stoichiometric evaluation of the binding between a DON and a larger particle (Abdellatef et al., 2022; Torisawa et al., 2014) to be conducted leading in turn to a better understanding of the effects exerted by 2D layouts on large cargos, such as organelles.

Discussion corresponding to (ii) and (iii) suggests that there are mechanisms on which spatial proximity of dimeric kinesins decreases run lengths, other than 2D arrangements between DONs and axonemes. The effects of the scaffold and linker stiffness can be excluded because the same DON scaffold and linker were used for all transporter experiments. Here, steric hindrance between kinesin motors bound to the same DON is proposed to be a reasonable factor that affects run lengths of different-layout transporters. When a part of kinesins of a multi-motor transporter binds on an axoneme, the kinesin(s) occupy a part of binding sites on microtubule(s) [MT(s)] and would hinder further binding of other kinesin motors in the same

DON, affecting on-rate of DON-bound kinesins. Steric hindrance might also increase the off rate of close kinesin motors. Thus, spatial proximity between motors may reduce the number of motors that simultaneously associate with MTs in the same transporter and thus would decline consequent run lengths. Form another perspective, the cooperative effect in the binding of kinesin based on conformational switching of MTs (Peet et al., 2018; Shima et al., 2018), where binding of kinesin(s) causes a conformational change of MTs and promotes further binding (binding frequency) of other kinesin motors (Shima et al., 2018), is considered. Currently, it is difficult to obtain conclusion: 1) free remaining kinesins and/or other microtubule-associated proteins on axonemes might affect the data; 2) little is known about the conformational effect in axonemes and that under high ionic (>210 mM NaCl) conditions used in the current study; and 3) we have not measured the MT conformation directly. However, when one or some of kinesins on a multi-motor transporter bound to an axoneme, the cooperative binding of kinesin owing to the MT conformational change may accelerate the binding frequency of other motors on the same transporter and might enhance the run length. The conformational change in MTs is known to be switch-like (Shima et al., 2018) but barely propagate along neighboring protofilaments (PFs) in a MT (Peet et al., 2018; Vu et al., 2022). Considering the fast rotational diffusion of the 28HB rod (iii), the 2D arrangement of kinesins on a DON would not affect the real kinesin arrangement on MT, and thus would not affect the number of PFs used for transporter movements. On the other hand, crowded conditions could increase the number of involved neighboring PFs for motors on a transporter with two pathways: (i) enhancing kinesin dissociation (Telley et al., 2009), which increases the possibility of re-binding of the kinesin motor on a neighboring PF; or (ii) causing kinesin side-shifting to neighboring PFs (Schneider et al., 2015; Telley et al., 2009). In this scenario, steric hindrance of kinesins in multi-motor transporters may enhance the number of PFs involved in motors on the same transporter and

thus decrease the number of bound kinesin per PF, diminishing the cooperative effect in the binding of kinesin among the same PF. Taken together, steric hindrance might be a reasonable and/or dominant factor that affect run lengths in different-layout transporters, but conformational switching of MTs might also involve it. Further analyses of kinetics of motors in a transporter and structural effects of kinesin binding on axonemes help understand how spatial proximity of dimeric kinesins decreases run lengths.

(iv) With respect to monomeric kinesins, Miyazono et al. have previously described the effect of inter-molecular distance on motility (Miyazono et al., 2010). They linked two monomeric kinesins with a 2–14-nm DNA molecule and analyzed motility. Single-molecule imaging data obtained by the current study which indicated that the distance between two monomeric kinesins exerted a strong effect on run length and a weak effect on velocity within a short distance, is consistent with their results. In addition, a gliding assay indicated that the gliding velocity of a coiled-coil-truncated short kinesin was more affected by motor density than that of a longer kinesin containing a coiled-coil domain, due to the difference in mechanical interference (Bieling et al., 2008). The fact that spatial proximity affected the velocity of monomeric kinesins more than that of dimeric kinesins may be attributed to the stronger mechanical interference between monomeric kinesins, which lack a coiled-coil domain.

(v) Miyazono showed that a molecular property, motile probability, of linked monomeric kinesins was affected by intermolecular distances around 8 nm. Considering that the rotational diffusion may disorder the arrangement of 28HB rods on axonemes, the difference between the motilities of the “1,2” and “1,3” transporters may be attributed not to 2D arrangement but to minor differences between the inter-molecular distances of monomeric kinesins (8–10 and 7 nm in “1,2” and “1,3” layouts, respectively).

Further application to evaluate collective functions of motors

The findings of the current study may be applicable to other motor proteins although the layout effect may be different in individual motors. For example, the effect of motor numbers is different in motors; increasing the numbers of a monomeric motor KIF1A (Soppina et al., 2014) and retrograde motor dynein (Torisawa et al., 2014) and Ncd (Furuta et al., 2013) enhanced velocities whereas increasing the number of kinesin-1 hardly affected velocity (Fig. 20). The main objective of this study was to establish an experimental system that enabled these biological issues to be explored. It may also be interesting to investigate the underlying molecular mechanisms, including stepwise dynamics and association/dissociation constants, in more detail. The fact that my experimental system enabled the successful visualization of fluorescence in motor molecules on transporters indicated that it may be useful for observing the behavior of individual motors in transporters. However, several optimizations and technological advancements are required in order to achieve this. For example, the $SNAP_f$-tag contains a cysteine residue, which prevents the application of conventional maleimide-based chemistry to label a specific residue in the motor domains. The aldehyde-tag (Shi et al., 2012) and the unnatural amino acid technology (Liu and Schultz, 2010) are excellent approaches that may be utilized to overcome such specific labeling issues. Besides, small and efficient fluorescence probes should be developed to a level which would allow them to be uses for tracing fluorescence behaviors of a motor domain in a transporter. Further advances in these technologies may help elucidate molecular mechanisms underlying collective transports.

In summary, this study used a DNA origami scaffold to reveal the manner in which the layouts of dimeric and monomeric kinesin-1 molecules affect collective movement. Dense layouts of dimeric kinesin motors shortened run length while exerting a moderate effect on velocity. Since reconstitution of higher-order structures using DONs involves a major research

area aimed at exploring detailed mechanisms (Abdellatef et al., 2022; Hariadi et al., 2015; Ibusuki et al., 2020) and/or engineering molecular machines (Hariadi et al., 2016; Ibusuki et al., 2022; Matsuda et al., 2019), the information gathered by the current study may be useful for designing future transport systems. Furthermore, the system that I have developed here can be applied to other motors as well as to investigate more complicated characteristics corresponding to opposition to motion, applied load, and avoiding roadblocks. Combining theoretical model analyses (Furuta et al., 2013; Kunwar et al., 2008; Uçar and Lipowsky, 2020) with layout effects may enable the construction of artificial motile systems that can function in both natural and artificial cells. It is anticipated that the experimental system that I have built will provide a powerful platform with which to evaluate the role played by intermolecular layouts of motors and intermolecular coordination mechanisms in collective motility.

Part II. DON-based purification system for cryo-EM analysis

II-1. Introduction

In the previous part, DONs were used to establish an experimental system for functional analysis of a motor protein. The system showed the ability of DONs for controlling molecular layouts. In addition to functional analysis, structural determination of POIs is also crucial for understanding how biological processes are occurred and highly regulated. Cryo-EM single-particle analysis (SPA) is a powerful platform to determine the architectures of POIs with high resolutions (Schultz, 1988). Purified POIs are applied on grids, and POIs embedded within thin layers of vitrified ice are visualized. Thousands to millions of POI particles within the thin ice layers are captured using cryo-EM, and used to reconstruct high-resolution 3D structures. The sample preparation of POIs limits the efficiency of this process. The architectures of many mesoscale super-complexes have been determined by independently purifying several components and then reconstituting complete complexes in test tubes (Abdella et al., 2021; Chen et al., 2021; Hao et al., 2021; Webster et al., 2020; Zhang et al., 2021). These purification processes are expensive and time intensive. Moreover, increasing the structural intricacy increases the heterogeneity of the reconstructed super-complexes and hence the cost of SPA. Furthermore, the reconstituted complexes might be different from those of the native structures inside cells. To address these challenges, a method of purification from cellular extracts using size-exclusion chromatography has been reported, which requires fewer steps (Kyrilis et al., 2021). This purification approach has advantages in terms of the analysis of native structures; however, as the separation is dependent only on the size, purifying complexes of interest from similar-sized non-target complexes is difficult. Affinity-based binders can capture specific sub-components and thus help overcome this problem. Antibody-coated superparamagnetic beads achieve affinity purification from cell lysate (Schmidli et al., 2019). For multi-affinity

purification however, the random absorbance of binder modules on the bead surfaces makes it difficult to purify complexes using spatially-defined multiple binder modules in one step. On the other hand, the layouts of the binder modules can be accurately designed on DONs, so they can be used as a carrier for multi-affinity purification using defined layouts of binder modules that interact with different motifs of POIs (Rinker et al., 2008). A pioneering study has reported multi-affinity purification of a POI, thrombin, using microchip isotachophoresis (Mei et al., 2013). Nonetheless, the DON-based purification of native POIs expressed in cell lysate and cryo-EM-based structural analysis have not yet been performed. Therefore, establishing a system to purify POIs from cell lysates via DONs and provide cryo-EM analysis is meaningful.

In this part, an experimental system to purify a POI using a DON carrier is introduced. The system enabled the purification of model super-molecules, ribosomes, from bacterial lysate. Purified complexes of DONs and ribosomes were visualized using cryo-EM. SPA reconstructed the structures of ribosomes, confirming the DON-based purification of native ribosomes expressed in bacterial cells. These results highlight the potential of DONs as purification carriers for the structural analysis of super-complexes.

II-2. Materials and Methods

Preparation of DNA origami

The square lattice-type, 42-helix bundle (42HB) DNA origami brick reported by Dietz group (Gerling et al., 2018) was used. The positions of dual biotin (dB) and Cy3 were designed by Yuxiang Liu (Tadakuma group) and Prof. Hisashi Tadakuma (School of Life Science and Technology, ShanghaiTech University, China) using caDNAno (https://cadnano.org/). The 42HB bricks were prepared following a protocol provided by Yuxiang Liu and Prof. Hisashi Tadakuma.

dB-modified 42HB bricks were prepared using the following procedures or provided by Yuxiang Liu. The scaffold of P7560 was purchased from tilibit nanosystems. For samples prepared by the author, unmodified, dB-modified (Supplementary Table 7) and Cy3-labeled staple (staple number, 198) were purchased from Eurofins Genomics, Integrated DNA Technologies, and Sigma Aldrich, respectively. For samples prepared by Yuxiang Liu, all staple strands were purchased from GenScript. Staple mixes were prepared using all staples except a Cy3-staple that was omitted owing to fragility against ultraviolet (UV) light. P7560 (20 nM) and 200 nM of each staple (10-fold excess) were mixed in Barrel Buffer [5 mM Tris-borate, pH 7.6, 20 mM magnesium acetate ($Mg(OAc)_2$), 5 mM sodium acetate (NaOAc), and 1 mM EDTA] and heated at 65°C for 15 min and annealed at 50°C for 4 h. Excess staples were removed by PEG precipitation (Stahl et al., 2014). The purified 42HB bricks were irradiated for 1 h with UV light using ASASHI SPECTRA MAX-350 to produce thymine dimers at the cross-overs or at the end of staples. The UV-irradiated 42HB bricks were incubated with the Cy3-labeled oligonucleotide for 30 min at 45°C. The samples prepared by the author were directly used in the following process. The samples prepared by Yuxiang Liu were concentrated to 1 μM by PEG precipitation and delivered to RIKEN (1-chōme-7-22 Suehirochō, Tsurumi Ward, Yokohama, Kanagawa 230-0045, Japan) at RT.

The 42HB bricks with dB and Cy3 were diluted to 5-20 nM and incubated with streptavidin (SA; S888, Invitrogen; 1600 Faraday Avenue, PO Box 6482, Carlsbad, CA, 92008, USA) for 20 min at RT at a molar ratio of dB/SA of 1:10 in Barrel Buffer containing 5 mM $Mg(OAc)_2$. The remaining SA was removed by PEG precipitation with 10 mM Mg^{2+}. The pellets of SA-labeled 42HB bricks were dissolved in Barrel Buffer containing 5 mM $Mg(OAc)_2$ or buffer containing an indicated concentration of Mg^{2+}. The molar concentration was determined using a NANODROP 2000 (Thermo Scientific) with an approximate molar mass of

4.67 MDa. The concentration of SA was assumed as the 42 HB brick concentration multiplied by the designed dB number. The purified 42HB bricks were frozen in liquid nitrogen and stored at -80°C.

Preparation of ribosomes

Purified 70S ribosomes containing L20-SNAP-tag and S2-HaloTag were provided by Prof. Hisashi Tadakuma and Prof. Koichi Ito (Department of Computational Biology and Medical Sciences, Graduate School of Frontier Sciences, The University of Tokyo) (Zhou et al., 2011). Molar concentration of ribosomes was determined using a NANODROP 2000 at 260 nm using a molar extinction coefficient of 41,700 M^{-1} cm^{-1}.

For labeling with biotin and Cy5, 10 μM ribosomes were incubated for 30 min on ice with 40 μM SNAP-biotin [BG-biotin; New England Biolabs]. BG-labeled ribosomes were further incubated with 10 μM Cyanine5 NHS ester (Cy5-NHS; 23020, Lumiprobe Corporation) for 60 min on ice. Unreacted BG and Cy5-NHS were removed using an Amicon Ultra-0.5 Centrifugal Filter Unit of 30 kDa molecular weight cutoff (Merck Millipore) following the manufacturer's protocol. Washing procedure was performed five times using buffer A [20 mM 4-(2-hydroxyethyl)-1-piperazineethanesulfonic acid (HEPES; pH 7.5), 200 mM KCl, 6 mM $Mg(OAc)_2$ and 7 mM 2-mercaptoethanol]. Ribosome concentration was determined as described above. Purified ribosomes were frozen in liquid nitrogen and stored at -80°C.

Preparation of *E. coli* lysate

A strain of *E. coli* containing L20-SNAP-tag and S2-HaloTag was provided by Prof. Koichi Ito (Zhou et al., 2011). Tag-fused ribosomal proteins were induced by arabinose. Cells were pre-cultured for 6 h at 37°C in LB medium containing 0.2% arabinose, 50 μg/mL ampicillin and 50

ug/mL kanamycin. Pre-culture (100 µL) was inoculated into 200 mL media containing 0.1% yeast extract, 1% tryptone, 0.25% NaCl, 0.5% arabinose, 50 µg/mL ampicillin, and 50 µg/mL kanamycin and shaken overnight at 37°C. Cells were harvested by centrifugation at 2,000×g for 10 min at 4°C. The pellet was suspended in 5 mL buffer A supplemented with 1× cOmplete Proteinase Inhibitor Cocktail EDTA-free (Roche). The suspended cells were lysed by sonication using TAITEC VP-30[5] with an output of 5 on ice for total 2 min (12 cycles of 10-sec sonication and 30-sec cooling). The crude extract was centrifuged at 20,000×g for 30 min at 4°C in a 15 mL tube and sterilized with a 0.22-µm polyvinylidene fluoride filter (Merck, SLGVR33RB). Protein concentration was determined using Bradford assay (Bio-Rad, 5000006) with bovine serum albumin (BSA) as a standard. The lysate was frozen in liquid nitrogen and stored at -80°C.

Electrophoretic mobility shift assay (EMSA)

The methods and buffer conditions were adjusted to each experiment. For EMSAs using biotin-conjugated DNA, a DNA fragment (biotin-ACGGGAAAGTCGACAGGGATCGGTGCACTACCACAAGCACCCAGGTGGATGTGGAGATATGGTTATGGGTAAGATAGATGGTGAGGTGATGAGTTTAAAGGAGTGAAGTATGGAGTGAAGAGAGATGGGTAGATAGTAGTTGAGTAGGGAGTGAAGTCCtgca, where uppercases are double-stranded and lowercases are single-stranded) was provided by Dr. Yuko Murayama (Murayama et al., 2023). Briefly, DNA was generated by PCR using a biotin-conjugated primer (5' biotin-ACGGGAAAGTCGACAGG) and purified using Wizard® SV Gel and PCR Clean-Up System (Promega). Biotin-labeled 42HB bricks were prepared by introducing a dB-conjugated staple at different positions as described in the section "Preparation of DNA origami". After mixing SA, the SA-labeled 42HB bricks (20 nM) was incubated for 30

min at RT with the biotin-conjugated DNA at a SA tetramer/biotin molar ratio of 1:8 in Barrel Buffer containing 5 mM $Mg(OAc)_2$.

For EMSA using unlabeled ribosomes, 1 μM SNAP-tagged ribosomes were pre-incubated for 30 min at RT with SNAP-biotin (New England Biolabs) at a SNAP/BG molar ratio of 1:0, 0.5, and 2 in buffer A containing 30 mM KCl. The 42HB brick with one Cy3 and four SA tetramers at the positions #4, 6, 7, and 8 (Supplementary Table 7) was incubated for 30 min at RT with biotinylated ribosomes at indicated SA/ribosome molar ratio in buffer A containing 30 mM KCl.

For EMSA using biotin-labeled ribosomes, 10 nM 42HB brick with eight SA tetramers (80 nM SA) were incubated for 20 min at RT with 0, 20, 80, or 320 nM biotin-labeled ribosome in buffer A containing 30 mM KCl.

For EMSAs using *E. coli* lysate, BG-Cy5-biotin was provided by BingXun Wang and Prof. Hisashi Tadakuma (Shen et al., 2022) used to label the SNAP-tagged L20 protein. Briefly, Cy5 Bis NHS ester was simultaneously reacted with amino-modified BG and biotin hydrazide and the product containing both BG and biotin was purified using thin layer chromatography. Purified BG-Cy5-biotin was dissolved in dimethyl sulfoxide and delivered from ShanghaiTech University, China to RIKEN. BG-Cy5-biotin was mixed with BG-biotin (SNAP-biotin, New England Biolabs) at a molar ratio of 1:19 and used as a BG-biotin mixture. Cell lysate (2 mg/mL protein) containing L20-SNAP-tag and S2-HaloTag was pre-incubated for 60 min at RT with the BG-biotin mixture. Unless otherwise noted, SA-labeled 42HB bricks at a SA concentration of 160 nM were incubated with biotinylated lysate (1.4 mg/mL protein) for 30 min on ice at a SA/BG molar ratio of 1:4. The concentration of BG-biotin mixture at the pre-incubation step was adjusted to achieve the SA/BG molar ratio of 4 at the binding step.

These samples were mixed with loading dye containing magnesium ion and then applied

on 1–2% agarose gel prepared in 0.5× Tris-borate-EDTA (TBE) (nacalai tesque, INC.) containing 5 mM $MgCl_2$ dipped in running buffer (0.5× TBE and 2 mM $MgCl_2$) at 4°C. Electrophoresis was performed for 60–120 min at 100 V at 4°C. Fluorescent images of Cy3-labeled 42HB, Cy5-labeled ribosome and/or BG-Cy5-biotin were captured using Amersham Typhoon scanner (RGB system), ImageQuant LAS 4000 or LAS 4000mini (Cytiva). DNA was detected with the same devices after staining with SYBR Safe or SYBR Gold (Invitrogen).

Sucrose density gradient (SDG) centrifugation

Five to eight picomoles of 42HB bricks with ribosome and/or cell lysate were prepared following the procedures described in the section "Electrophoretic mobility shift assay (EMSA)." The samples were gently loaded onto a 10–40% sucrose gradient in buffer A containing 10 mM $Mg(OAc)_2$ prepared using Biocomp Gradient Master in a 13.2-mL Thinwall tube (Beckman Coulter, 344059). Centrifugation was performed at 34,300 rpm for 3 h at 4°C using a Beckman SW 41 Ti rotor in an Optima L-20K Ultracentrifuge (Beckman Coulter). The gradient was fractionated using Piston Gradient Fractionator (Biocomp) with a Triax detector (Fxn collector ATTO AC-5700, Biocomp). 42HB brick (Cy3 fluorescence)-containing fractions were verified by the Cy3 fluorescence using an Amersham Typhoon scanner (Cytiva) and were analyzed using 2% agarose gel for cryogenic electron microscopic (cryo-EM) analysis.

The fractions determined by agarose gel electrophoresis were collected and concentrated by PEG precipitation. Briefly, the fractions were incubated on ice for 10 min in buffer A containing 10 mM $Mg(OAc)_2$ and 5% PEG 8,000 and centrifuged at 50,000 rpm for 30–60 min at 4°C. After removing the supernatant, the pellets were dissolved in buffer A containing 10 mM $Mg(OAc)_2$.

Cryo-EM analysis

Plain 42HB bricks without ribosomes were applied to glow-discharged holey carbon grids (Quantifoil R1.2/1.3; Quantifoil Micro Tools; -C). Samples containing ribosomes were applied to the same grid with a thin carbon layer (+C). Plunge freezing was performed using an EM GP2 (Leica) with the following settings: temperature, 10°C; humidity, 75%; wait time, 0 (-C) or 30 (+C) sec; blot time, 2-3 (-C) or 0 (+C) sec. The grids were stored in liquid nitrogen. The grids were imaged as previously reported (Ehara et al., 2017), with some modifications. Briefly, images were obtained using a Tecnai Arctica cryo-EM (FEI) operated at 200 kV and equipped with a K2 summit direct electron detector (Gatan), using the software of SerialEM 3.8 (Mastronarde, 2005). Movies were captured with 1.47 Å/pixel and 1.25 e/Å^2/frame at 23,500×magnification.

Single-particle analyses were performed using Relion 3.1 (Nakane et al., 2018). The movies were motion-corrected using MotionCor2 (Zheng et al., 2017). The contrast-transfer functions were estimated using CTFFIND4.1 (Rohou and Grigorieff, 2015). More than 500 particles of each of the plain 42HB bricks, free 70S ribosomes, and complexes of the 42HB brick and the ribosome were manually picked to obtain reference images for auto-picking. The manually-picked particles were subjected to reference-free 2D classification and then reference 2D averages were generated. After auto-picking using the 2D references (Supplementary Table 8), the particles were extracted and selected with two rounds of 2D classification. For an initial model of the plain 42HB brick, a previously reported map of EMD-4354 (Gerling et al., 2018) was used with an initial low-pass filter of 20 Å. The initial models for free ribosomes (70S and 50S) and complexes of the 42HB brick and ribosome were generated using Relion from each dataset. The particles were subjected to 3D classification with four classes, and the selected classes were used to reconstruct a refined 3D density map. Postprocessing was performed to

calculate the Fourier shell correlation (FSC) and global resolution. The maps and atomic models from Protein Data Bank (PDB) were displayed using UCSF ChimeraX (Goddard et al., 2018) or open-source PyMOL (Schrodinger, LLC. 2010) (the PyMOL Molecular Graphics System, v.2.5.0 Open-Source; Python 3.1.0; Windows10, 64 bit).

II-3. Results

Visualization of a DNA origami nanostructure using cryo-EM

As the first step to observe POI captured by a DNA nanostructure, the DNA nanostructure itself, which does not contain any POI, was observed using cryo-EM. A 42HB DNA origami brick was used because the particles have been successfully observed using Cryo-EM (Gerling et al., 2018). The 42HB brick was folded from P7560 scaffold DNA and staples and purified by PEG precipitation (Fig. 31A). Cryo-EM measurement showed that particles of the 42HB brick (500 nM) were distributed at the edges of holes in a Quantifoil R1.2/1.3 grid (Fig. 31, B and C). The orientation of particles was biased; the surface with the largest area of the 42HB brick was parallel to the vitrified ice layer (Fig. 31C). By contrast, few particles were observed at the centers of holes in the same grid (Fig. 31D). This is probably because particles with the other orientations were unstable in the thin ice layer and therefore, rotated to a stable orientation or adsorbed by the carbon support film or filter paper during blotting. These particles were also found on carbon support films in the presence of more than 10 mM Mg^{2+} (Fig. 32A), suggesting a possible interaction between 42HB bricks and carbon support films under high Mg^{2+} concentration. 42HB bricks were also applied on a grid with an additional thin carbon layer to evaluate the effect of carbon surfaces on measurements. 42HB bricks were observed on the surface of a thin carbon layer. However, the orientation was extremely biased on the grid with a thin carbon layer; only the orientation facing the largest area to the carbon surface was observed

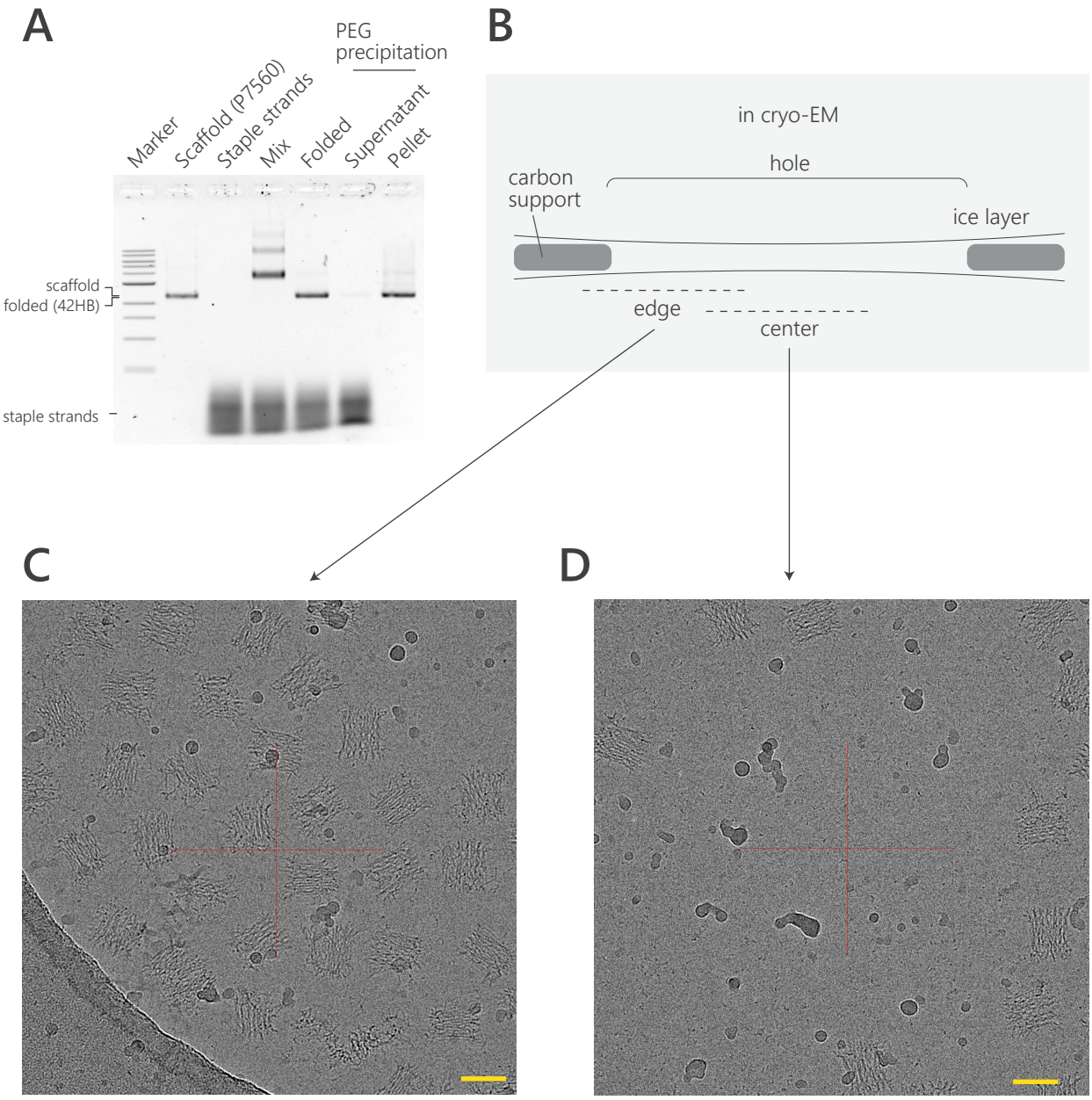

Fig. 31 | 42HB bricks were observed at the center of a grid

(A) An image of SYBR Safe-stained 1.0% agarose gel showing the process of preparation of the 42HB DNA origami brick. The 42HB brick was folded with a scaffold DNA and staples for 15 min at 65°C and for 4 h at 50°C and then purified by PEG precipitation. (B) Schematic showing the cross-section of a grid in cryo-EM. The regions shown in C and D are indicated with dashed lines. (C and D) Images of a grid on which the purified 42HB brick (500 nM) was applied. An edge (C) and center (D) of a hole of the carbon support film were observed using Arctica cryo-EM. Scale bars, 50 nm.

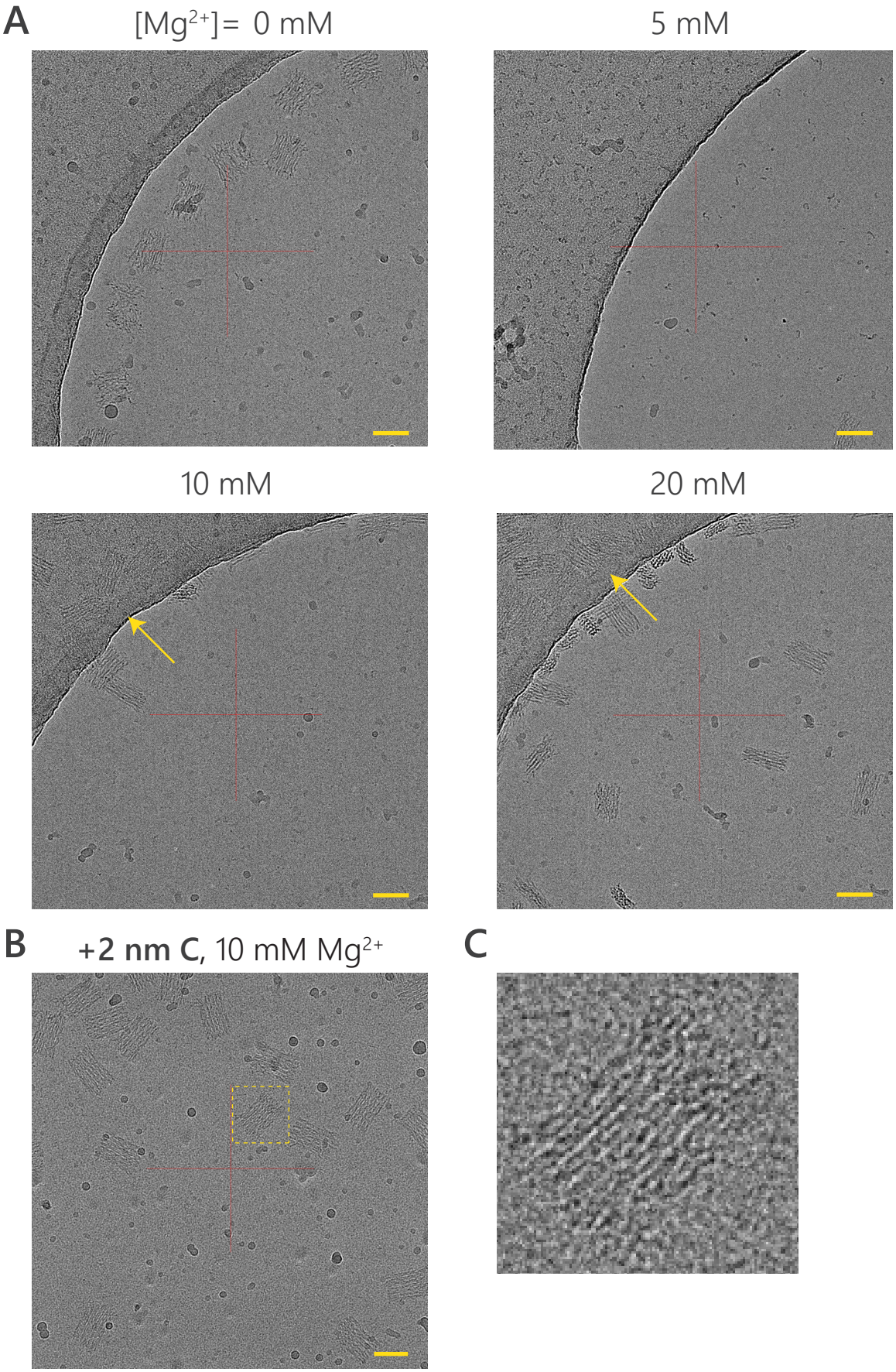

Fig. 32 | 42HB bricks were adsorbed onto the large area surface of a carbon film

(A) Images of 42HB bricks dissolved in buffer with different concentrations of Mg^{2+}. Edges between holes and carbon-support films in plain grids were captured. Yellow arrows denote the 42HB bricks adsorbed on a carbon film. (B) An image of a grid with a thin carbon layer. The 42HB brick with 10 mM Mg^{2+} was applied on the grid. Scale bars, 50 nm (C) A zoomed view of a 42HB brick particle indicated with a dashed square in (B).

(Fig. 32, B and C).

SPA was also performed to confirm that the experimental system worked. The property of biased orientation on carbon surfaces is not suitable for SPA, which requires different orientations of particles. Thus, the 42HB brick was applied on a plain Quantifoil R1.2/1.3 grid with several optimizations. 42HB bricks were concentrated to 1.5 μM by PEG precipitation, adjusted for blotting time, and regions with thick vitrified ice layers were imaged. Cryo-EM measurements showed two different orientations of 42HB bricks (Fig. 33). For SPA, reference 2D Class averages were generated from manually picked 42HB brick particles, and 2D classification confirmed different orientations of the particles (Fig. 34A). After several 2D/3D classifications, the 3D density map of 42HB bricks was reconstructed with a global resolution of 21 Å from 9,201 selected particles (Fig. 34, B-D). This structure was similar to a previously reported structure (Fig. 34E) (Gerling et al., 2018). These results indicate that cryo-EM measurement and SPA can be used to visualize 42HB brick-related structures.

Establishing a system to capture and purify POI using DNA origami

An experimental system was built to capture POIs onto 42HB brick particles. Non-covalent binding is desirable for future application to multi-affinity capture; thus, a SA-biotin system (Yan et al., 2003) was used to assemble POIs in the current part. Eight varieties of dual biotin-modified staples were incorporated into 42HB bricks and labeled with SA. Assembly of biotin-labeled molecules on the SA-labeled 42HB bricks was confirmed by EMSA using biotin-labeled double-stranded DNA (Fig. 35A). The average binding ratios to a SA site were estimated to be approximately 0.91 (Fig. 35B).

Using the SA-biotin binding system, ribosomes were assembled on 42HB bricks. To obtain biotin-labeled ribosomes, ribosomes from *E. coli* were biotinylated through a SNAP-tagged

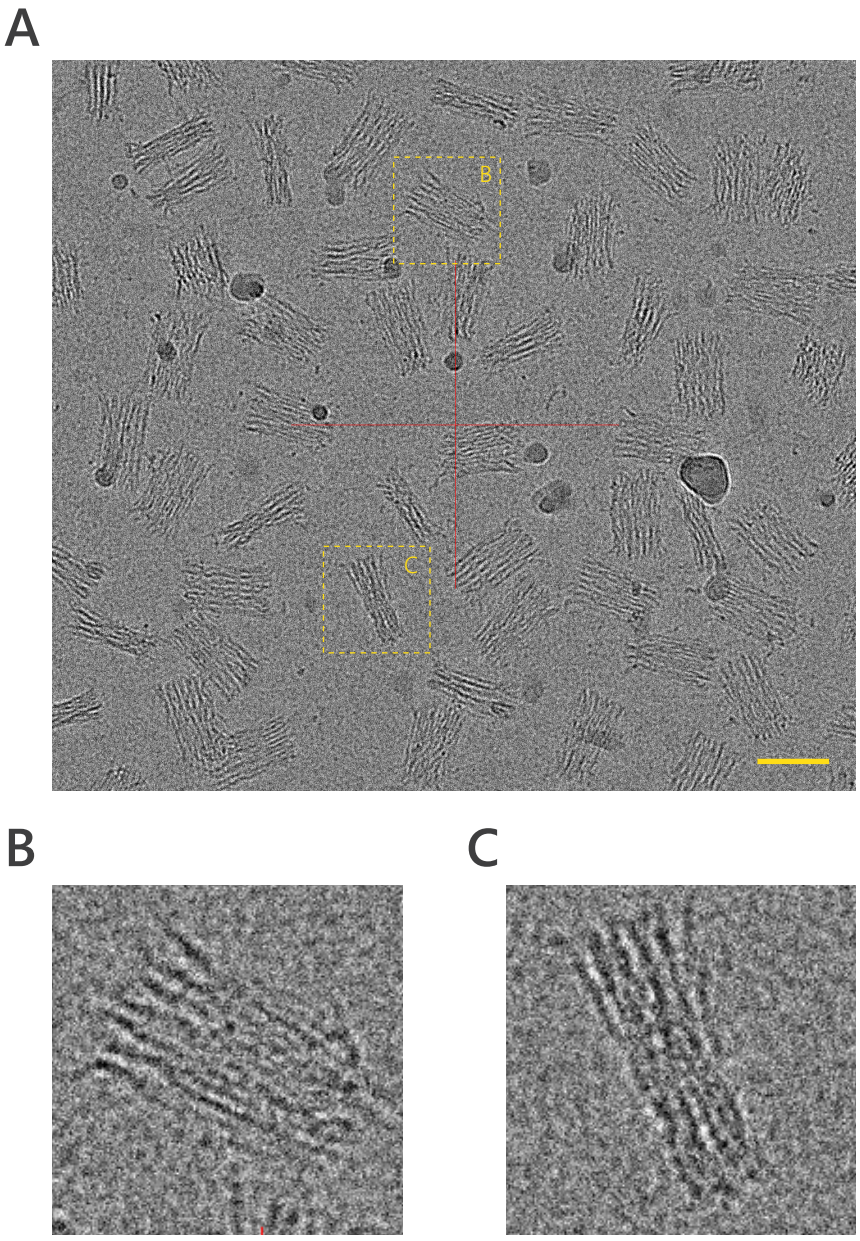

Fig. 33 | Cryo-EM measurement of the 42HB brick

(A) An image of a grid on which 1.5 μM 42HB bricks with 5 mM Mg^{2+} were applied. Scale bar, 50 nm. (B and C) Zoomed views of 42HB brick particles adsorbed by large- (B) or small- (C) area side, indicated with dashed squares in (A).

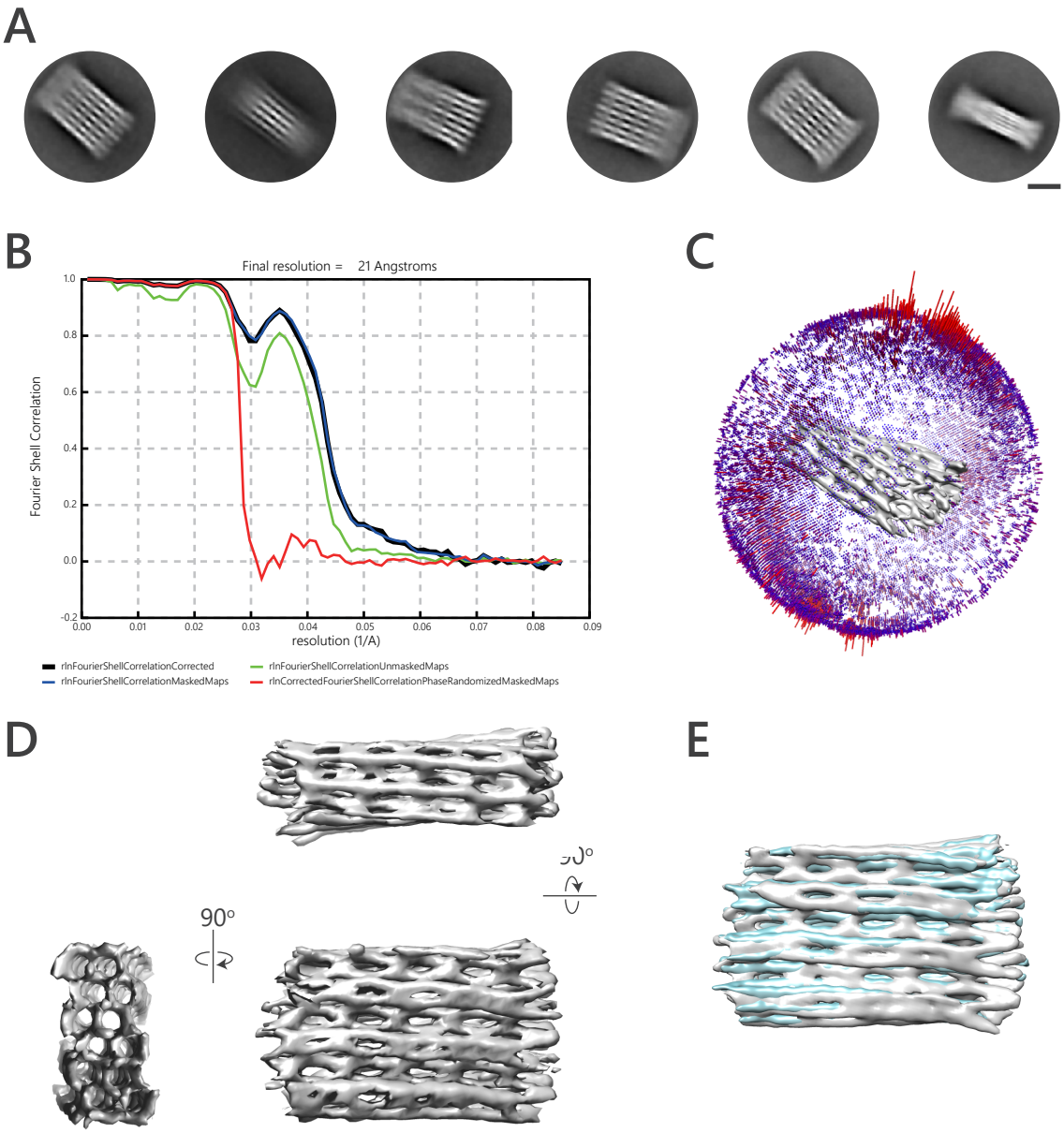

Fig. 34 | Reconstruction of the 3D structure of the 42HB brick

(A) Representative 2D Class averages. Scale bar, 20 nm. (B) FSC plot showing a global resolution of 21 Å. Results were obtained from 9,201 selected particles extracted from 522 images. (C) 3D histogram showing the distribution of orientation of 42HB bricks. (D) The reconstructed 3D density map of the 42HB brick. (E) The density map in (D) (gray) superimposed on a previously reported density map of the same particle (cyan, EMD-4354).

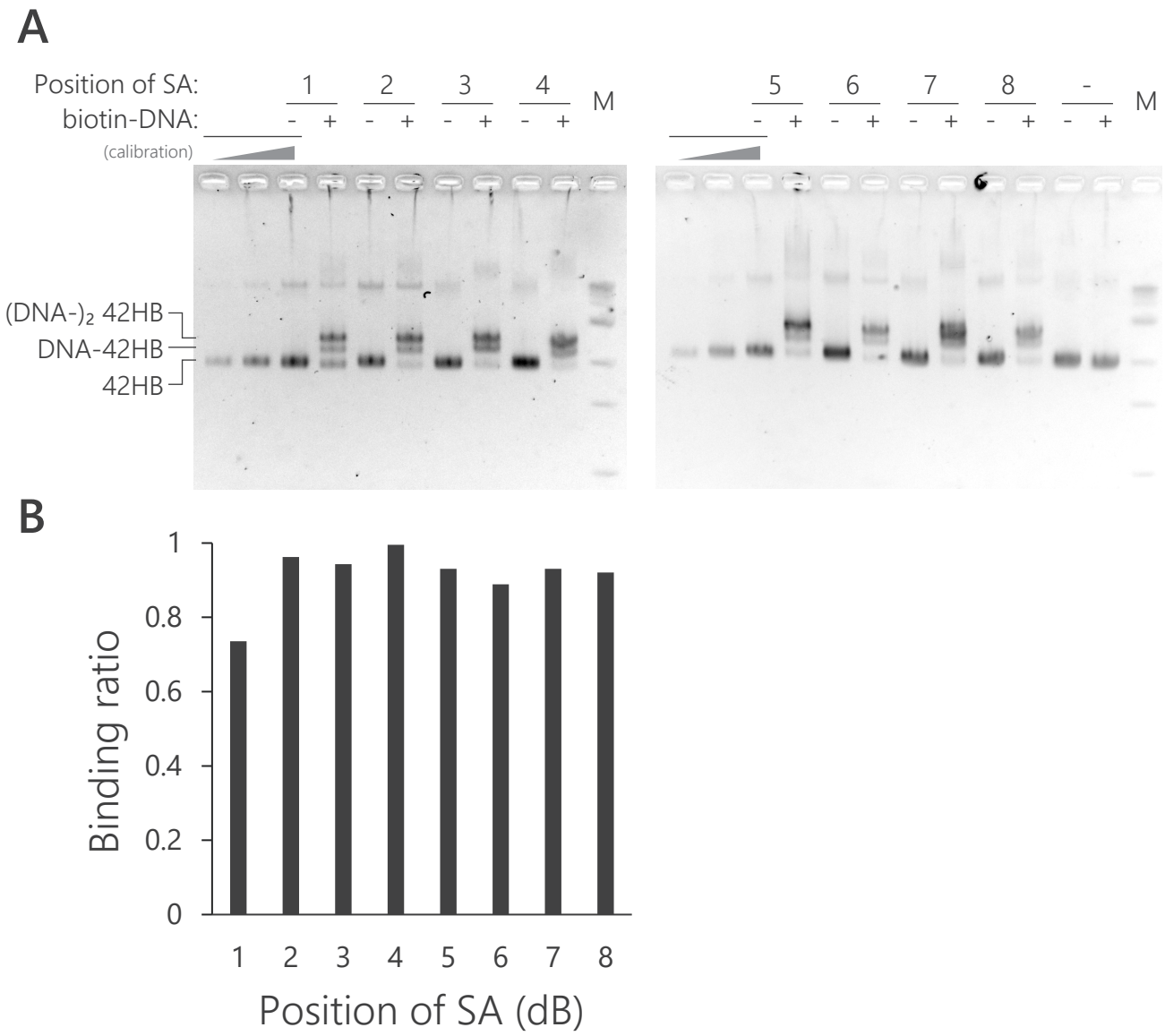

Fig. 35 | A biotin-labeled molecule bound to SA on the 42HB brick

(A) Images of SYBR Safe-stained 2.0% agarose gel showing mobility shifts of 42HB bricks with a SA tetramer in different positions. The positions of SA are denoted with the numbers #1–8 (see Supplementary Table 7). The 42HB bricks were incubated with biotin-labeled 159-bp DNA fragments and were then analyzed by electrophoresis. Note that up to two molecules of the biotin-DNA fragments bind to SA on the 42HB brick, since SA has four binding pockets for biotin and only two of them are occupied by a dB-labeled staple. 42HB denotes the 42HB brick. (B) Quantification of the binding ratio of biotin-labeled DNA fragment. The vertical axis shows molar fraction of each 42HB brick bound to more than one biotin–DNA molecule. Calibration curves for estimation were prepared for each gel.

ribosomal protein L20 incorporated into the 50S ribosome (Fig. 36A). EMSA showed specific binding of SNAP-tagged ribosomes to a SA-labeled 42HB brick via SNAP-ligand (BG)-conjugated biotin molecule (BG-biotin) (Fig. 36B). Assembly on the 42HB brick was further confirmed using purified L20-biotinnlated ribosomes cleaned of free biotin (Fig. 36C). By contrast, biotin-independent and non-specific binding of purified ribosomes to SA-coated magnetic beads was observed even under 1 M NaCl concentration (Fig. 37). These results indicate an advantage of DNA origami as a carrier with little non-specific interaction with POI.

The 42HB brick-ribosome complex was used to develop a purification method to separate the complex from free ribosomes. Several purification methods, such as size exclusion chromatography using open column, PEG-precipitation, ammonium sulfate precipitation, and ultra-filtration, were found to be ineffective. By contrast, SDG centrifugation successfully separated 42HB-bound ribosomes from free ribosomes (Fig. 38A). In this system, the unbound 42HB brick was contaminated with ribosome-bound 42HB brick as identified by the broad peak distribution of the free 42HB brick (Fig. 38B). To avoid the effect of unbound 42HB bricks, the concentrated samples were applied on grids with a thin carbon layer, on which ribosomes adsorb more efficiently than do the unbound 42HB bricks. Cryo-EM measurements showed possible densities of the 42HB brick with additional globular densities, which seems to be a ribosome, in the vicinity (Fig. 39A). To analyze these complexes, possible complexes were manually picked and used to create 2D Class averages for auto-picking. Several 2D Class averages regarding possible ribosome-bound 42HB bricks were observed (Fig. 39B). The low resolution of class averages may be attributed to the translational and rotational motions of ribosomes relative to 42HB bricks caused by the flexible linkers such as SA- and SNAP-tag protein. A reconstructed 3D density map showed a set of one globule and dozens of bundles, which seemed to be a ribosome and a 42HB brick, respectively (Fig. 39C). This indicates that the complex of a 42HB

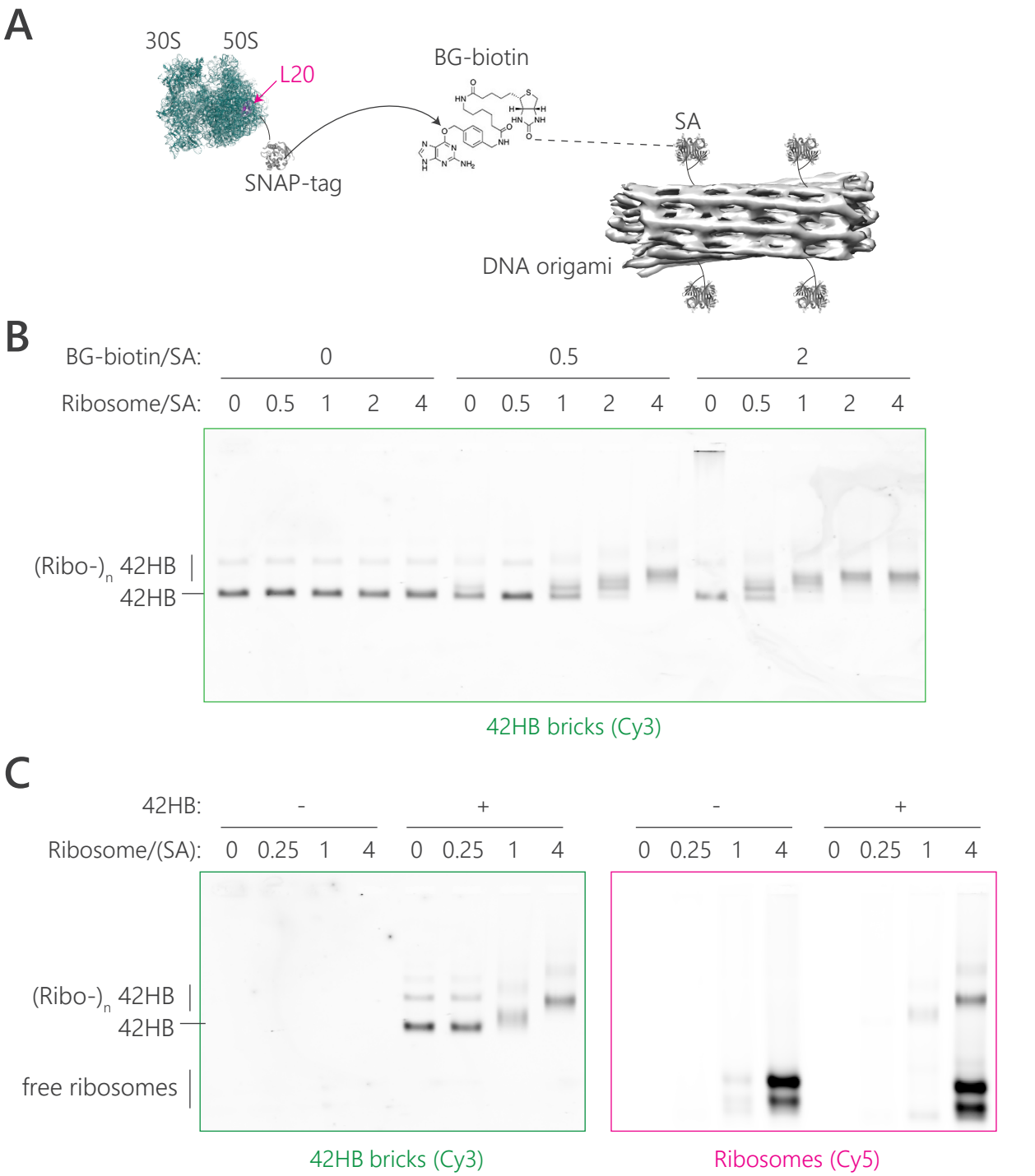

Fig. 36 | Biotin-labeled ribosomes bound to SA on the 42HB brick

(A) Schematic showing assembly of ribosomes on a 42HB brick via BG-biotin. The 50S subunit of ribosomes was labeled with SNAP-tagged ribosomal protein L20 (indicated with a magenta arrow). SNAP-tagged ribosomes were biotinylated with BG-biotin (SNAP-biotin, New England Biolabs) and incorporated into SA-labeled 42HB bricks. Cyan, the ribosome (PDB, 4V4A); magenta, L20; gray, SNAP-tag (PDB, 3L00), SA (PDB, 1MK5), and 42HB brick. (B) An image of 1.0% agarose gel showing mobility shifts of the SA-labeled 42HB brick and SNAP-tagged ribosomes via BG-biotin. The Cy3-labeled 42HB brick with four SA molecules was detected. Ribosomes containing SNAP-tagged L20 were pre-incubated with the indicated amount of BG-biotin and then mixed with the SA-labeled 42HB brick. The amounts of BG-biotin and ribosomes are shown as molar ratios to SA. (C) Images of 1.0% agarose gel showing mobility shifts of the Cy3/SA-labeled 42HB brick bound to Cy5/biotin-labeled ribosomes. The 42HB brick contains eight molecules of SA. The amounts of ribosomes [Ribosome/(SA)] denote a molar ratio of ribosomes to SA (+42HB). For (-42HB) lanes, the same ribosome concentrations as for (+42HB) were used. 42HB, the 42HB brick; Ribo, a ribosome.

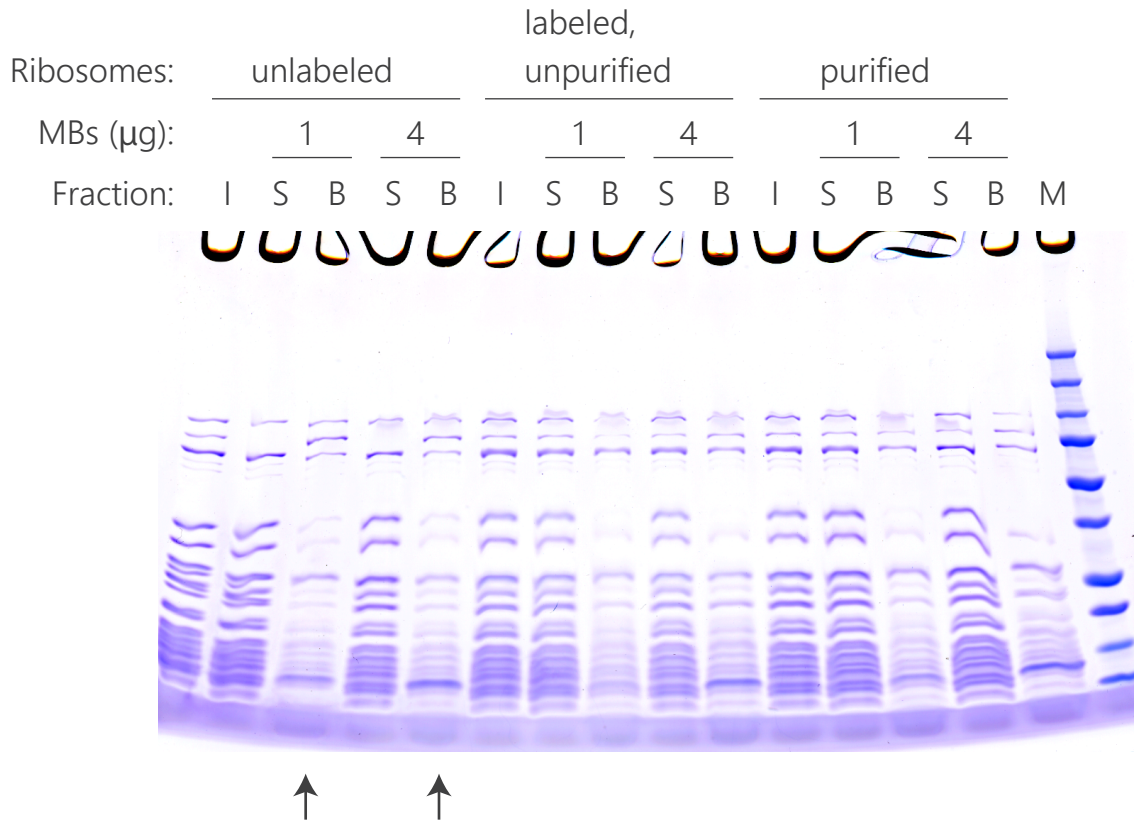

Fig. 37 | Ribosomes non-specifically interact with SA-coated magnetic beads

SDS-PAGE showing non-specific interaction between ribosomes and magnetic beads. Ribosomal proteins were stained with CBB. One or four microgram of Dynabeads MyOne Streptavidin C1 (Invitrogen) were applied on each of three types of 5 pmol ribosomes containing SNAP-tagged L20: (i) unlabeled ribosomes (unlabeled); (ii) ribosomes labeled with Cy5-NHS and BG-biotin but not purified (labeled, unpurified); and (iii) ribosomes labeled with Cy5-NHS and BG-biotin and then purified by ultra-filtration (purified). Beads were equilibrated and bound to ribosomes with buffer containing 1 M NaCl following the manufacturer's protocol. Arrows denote unlabeled ribosomal proteins non-specifically associated with magnetic beads. I, input; S, supernatant; B, beads; MBs, magnetic beads.

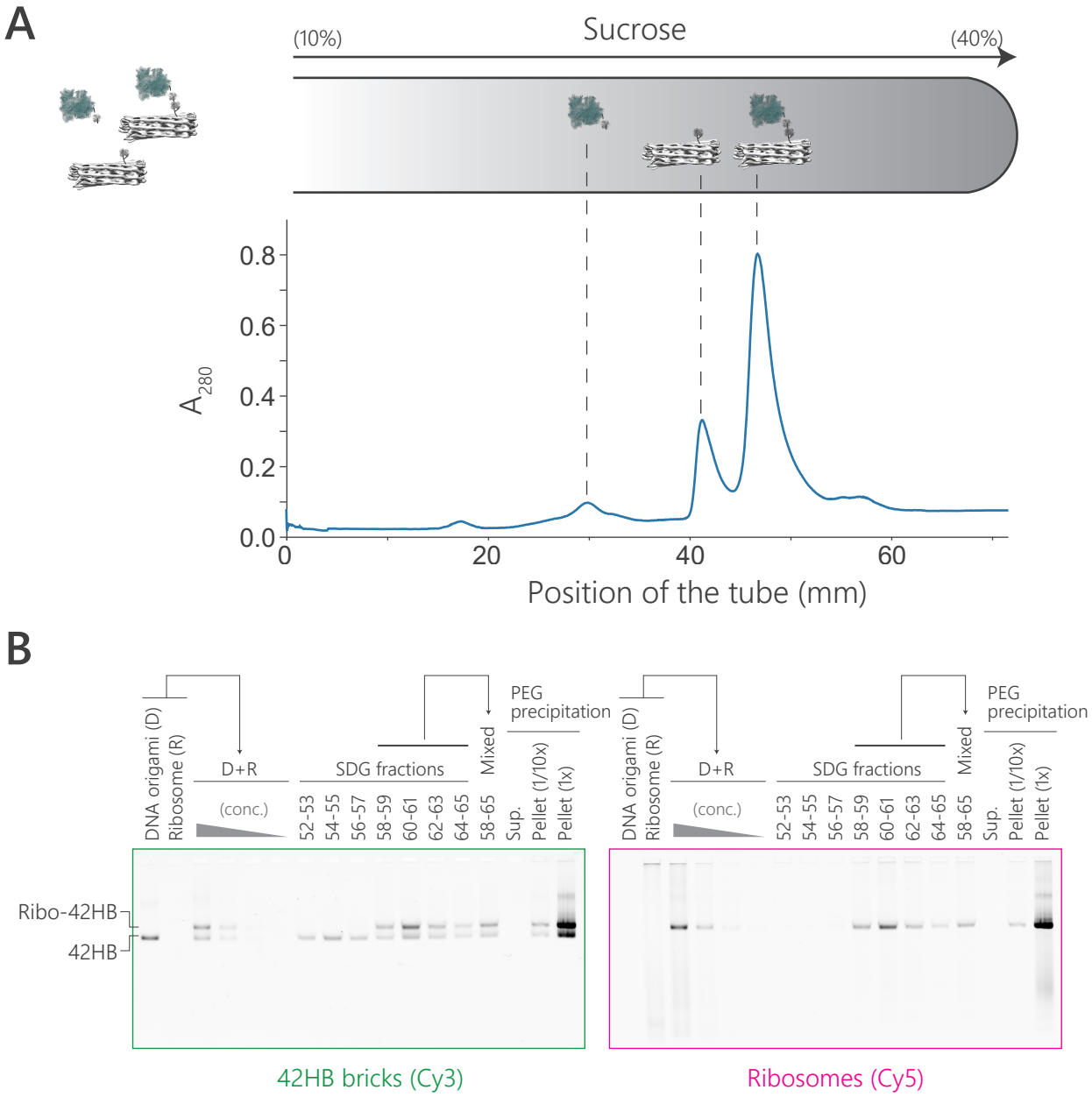

Fig. 38 | 42HB brick-bound ribosomes were separated from free ribosomes by SDG centrifugation

(A) Schematic of SDG centrifugation (top) and fraction profile of absorbance at 280 nm (bottom). The 42HB brick with one SA (5.12 pmol) was incubated with equimolar biotin-labeled ribosomes and applied on a 10–40% sucrose gradient. Note that both ribosomes and the 42HB brick show absorption at 280 nm. (B) Images of 2.0% agarose gel showing the preparation of ribosome-bound 42HB brick. The Cy3-labeled 42HB brick and Cy5-labeled ribosomes were detected through fluorescence. SDG fractions containing the 42HB brick (Cy3 fluorescence) were loaded. The fractions containing the ribosome-bound 42HB brick were collected and concentrated by PEG precipitation. 42HB, the 42HB brick; Ribo, ribosomes.

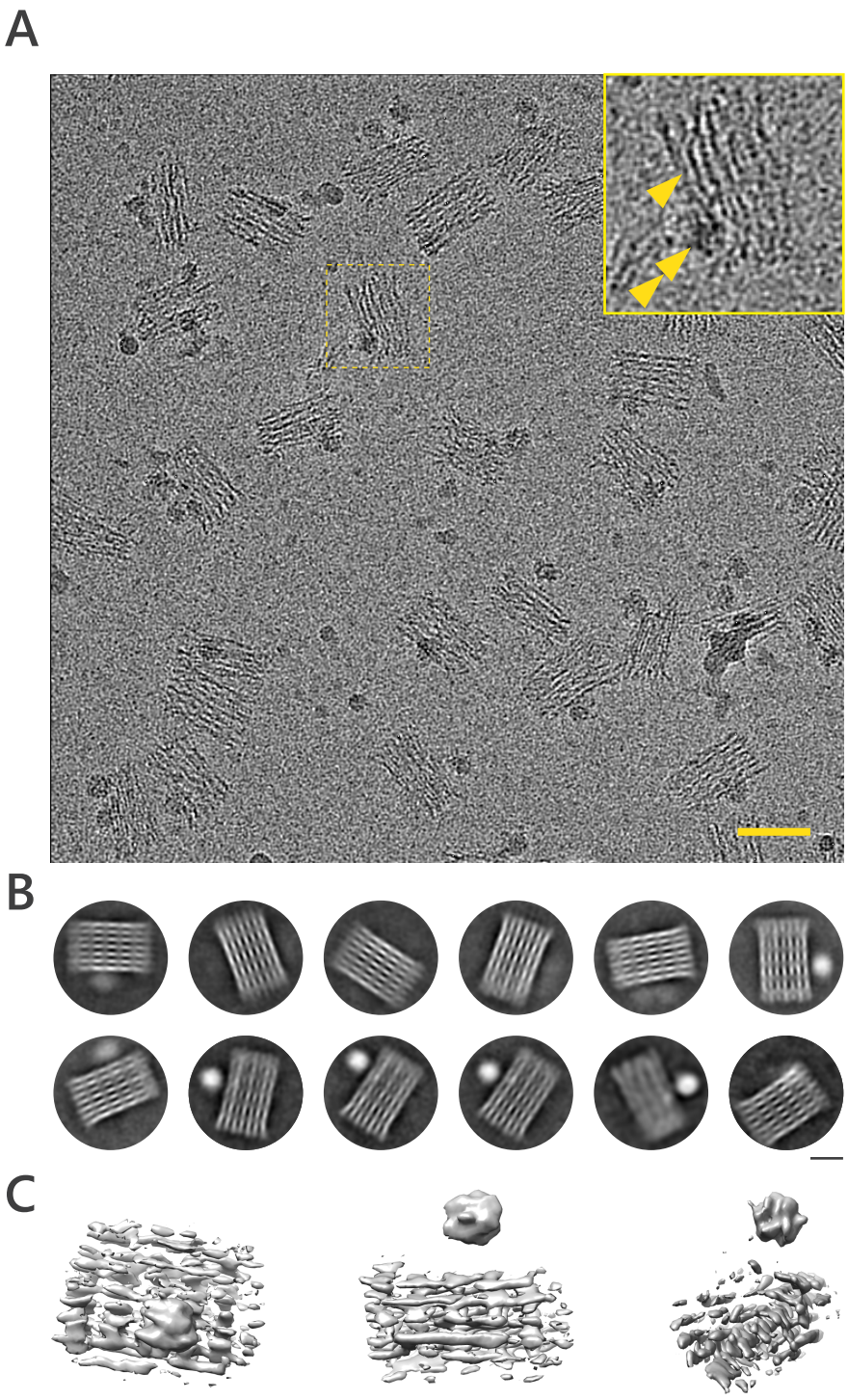

Fig. 39 | SPA of the ribosome-bound 42HB brick purified by SDG centrifugation

(A) An image of a grid with a thin carbon layer on which the purified ribosome-bound 42HB brick was applied. The mixture of SA-labeled 42HB brick and biotin-labeled ribosomes was purified by SDG centrifugation and concentrated by PEG precipitation. Scale bar, 50 nm. Inset, a zoomed view of the particle indicated with a dashed square. Single and double arrowheads denote a possible 42HB brick and a ribosome, respectively. (B) Representative 2D Class averages of 42HB bricks with and without the density of a ribosome. Scale bar, 20 nm. (C) A reconstructed 3D density map of ribosome-bound 42HB bricks. The map shows densities of a bundle and a globule, possibly corresponding to a 42HB brick and a ribosome, respectively.

brick and a ribosome was formed and collected by SDG centrifugation. SPA focused only on ribosomes was also performed, revealing that ribosomes in the sample after SDG centrifugation lacked the 30S subunit, while the 50S subunit was anchored to the 42HB brick via L20 (Fig. 40). For comparison, unpurified ribosomes mixed with the 42HB brick were observed using cryo-EM (Fig. 41A). SPA revealed the presence of 70S ribosomes in the unpurified sample (Fig. 42), as well as ribosome-bound 42HB bricks similar to those in the SDG centrifugation-purified sample (Fig. 41, B, and C). This suggests that 30S subunits dissociated during SDG concentration or grid construction. Taken together, the DNA origami-based purification system can capture a molecule through direct binding to the DNA carrier.

Purification of DNA origami-bound ribosomes from *E. coli* lysate

The DNA origami-based capturing method was then applied to a more complicated system, *E. coli* lysate. Lysate containing SNAP-tagged ribosomes was obtained from *E. coli*, in which SNAP-tagged L20 was expressed and was supposed to be incorporated into 50S subunits of ribosomes. The lysate was incubated for 60 min at RT with BG-biotin to biotinylate SNAP-tagged ribosomes via the SNAP-tag (Fig. 43A). The incubation process could work as a run-off procedure, where translating ribosomes were released from mRNAs. Agarose gel electrophoresis showed mobility shifts of SA-labeled 42HB bricks in a BG-biotin-dependent manner (Fig. 43, B and C). The average number of ribosomes captured by a 42HB brick, having two SAs, was < 1. This is probably because free SNAP proteins, such as the ribosome-unincorporated SNAP-tagged L20 and truncated SNAP-tag proteins, could also bind to SA but showed less mobility shifts of 42HB bricks than those of ribosomes. Moreover, the binding ratio peaked with a SA/BG-biotin molar ratio of 1:4 since an excess amount of BG-biotin occupied the binding pocket of SA.

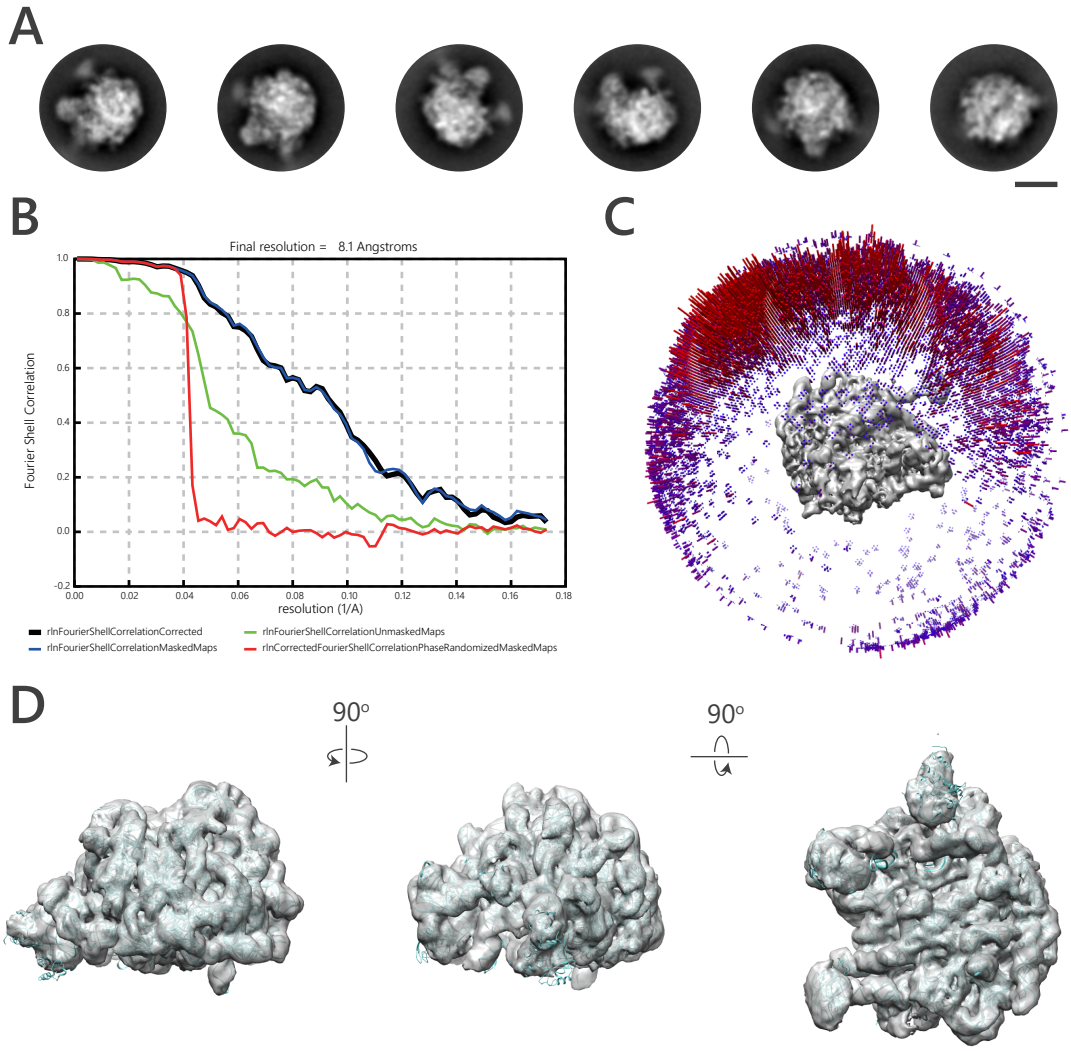

Fig. 40 | The 50S ribosome was reconstructed from the ribosome-bound 42HB brick purified by SDG centrifugation

(A) Representative 2D Class averages. Particles were picked using reference 2D Class averages of 70S ribosomes and 2D-classified using Relion. Scale bar, 10 nm. (B) FSC plot showing a global resolution of 8.1 Å. Results were obtained from 6,992 selected particles extracted from 460 images. (C) 3D histogram showing orientation distribution of particles. (D) Reconstructed 3D density map (semi-transparent gray) superimposed with a model of the 50S ribosome previously reported (PDB, 6WNT; cyan).

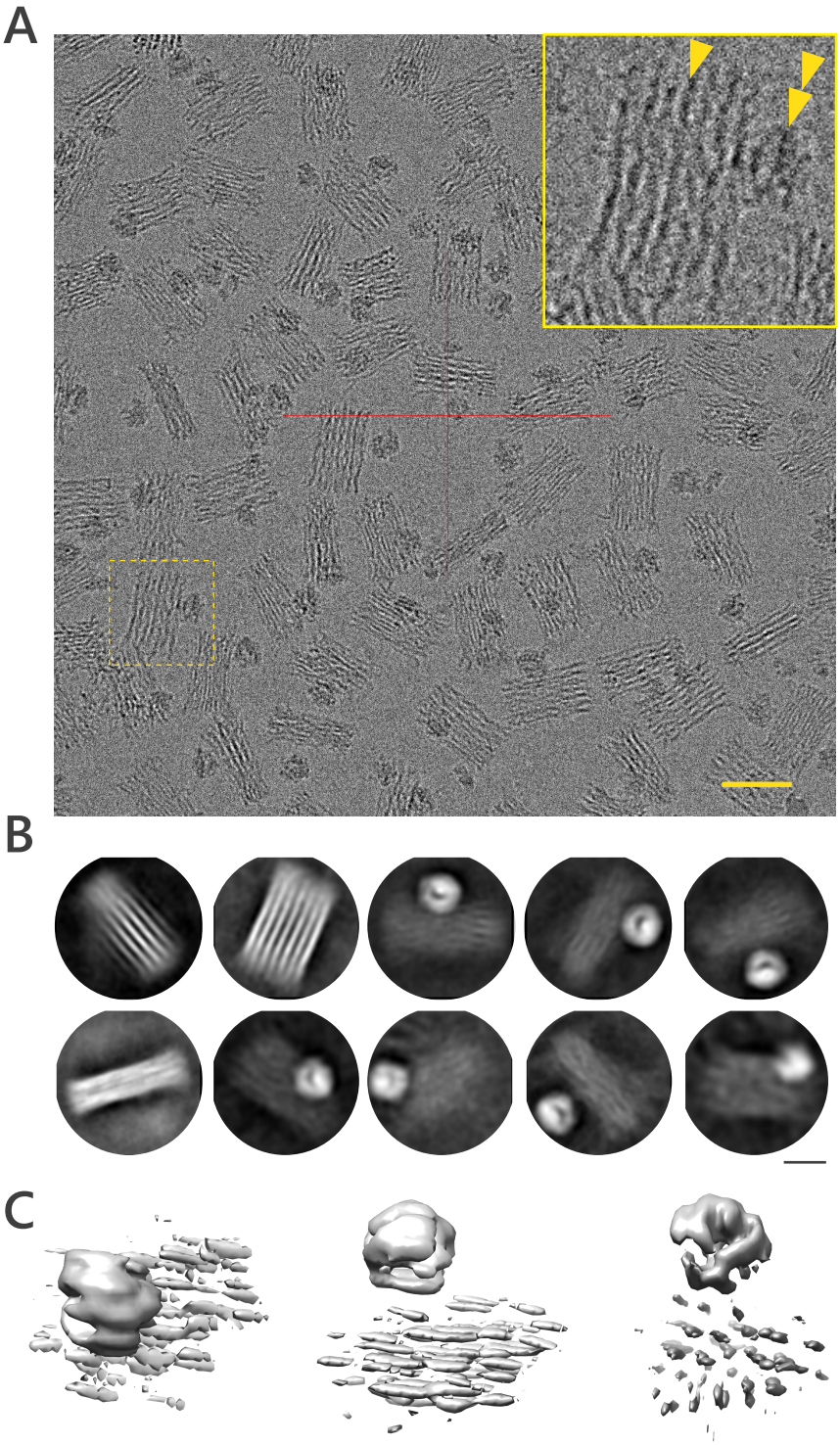

Fig. 41 | A possible ribosome-bound 42HB brick was reconstituted from the unpurified mixture of the 42HB brick and ribosomes

(A) An image of a grid with a thin carbon layer on which the mixture of the SA-labeled 42HB brick and biotin-labeled ribosomes was applied. SA-labeled 42HB brick was incubated with the equimolar biotin-labeled ribosomes for 10 h on ice and then loaded on the grid without any purification. Scale bar, 50 nm. Inset, a zoomed view of the particle indicated with a dashed square. Single and double arrowheads denote a possible 42HB brick and a ribosome, respectively. (B) Representative 2D Class averages of 42HB bricks with and without the density of the ribosome. Scale bar, 20 nm. (C) A reconstructed the 3D density map of the ribosome-bound 42HB brick. The map shows densities of a bundle and a globule, possibly corresponding to a 42HB brick and a ribosome, respectively.

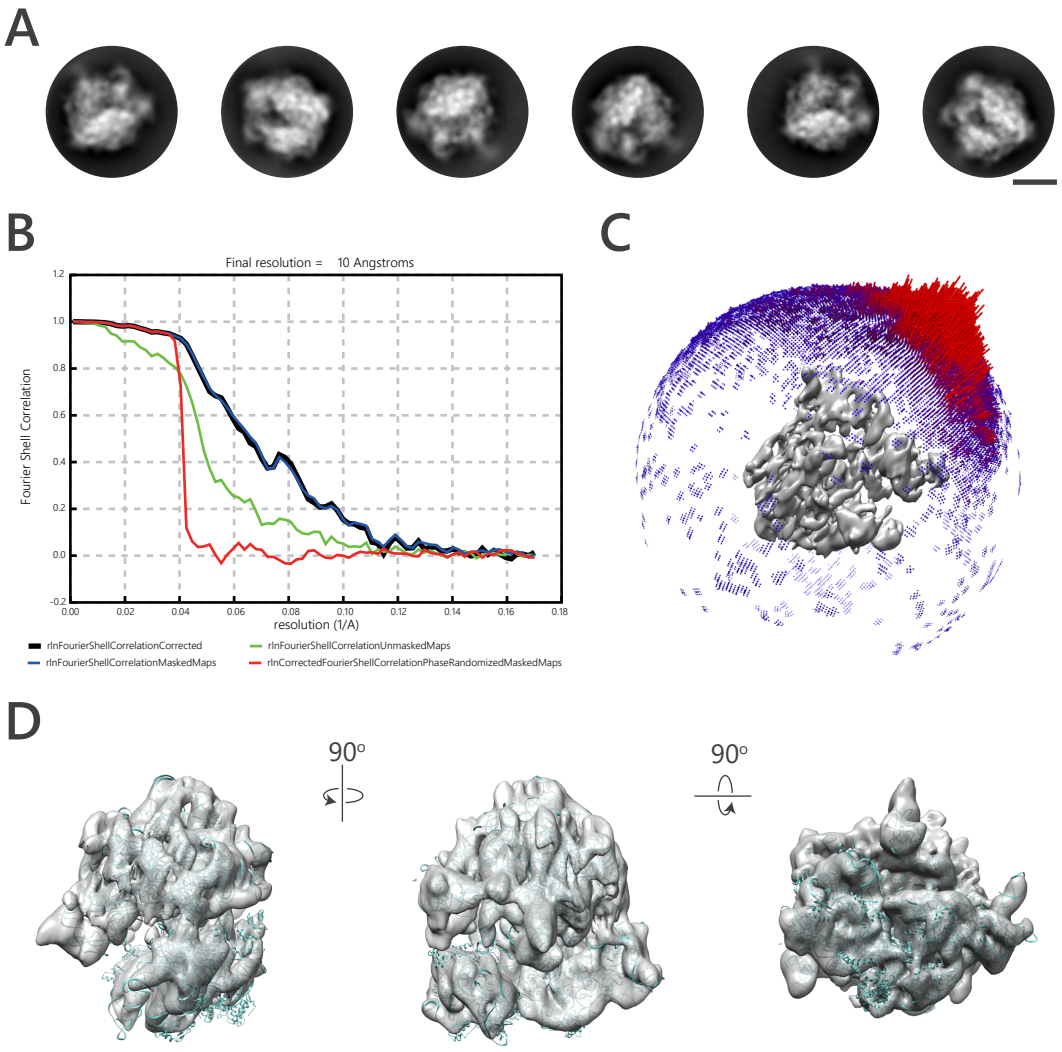

Fig. 42 | The 70S ribosome was reconstituted from the unpurified mixture of the 42HB brick and ribosomes

(A) Representative 2D Class averages. Particles were picked with reference 2D Class averages of 70S ribosomes and 2D-classified using Relion. Scale bar, 10 nm. (B) FSC plot showing a global resolution of 10 Å. Results were obtained from 13,219 selected particles extracted from 828 images. (C) 3D histogram showing orientation distribution of particles. (D) Reconstructed 3D density map (semi-transparent gray) superimposed with a model of the 70S ribosome previously reported (PDB, 4V4A; cyan).

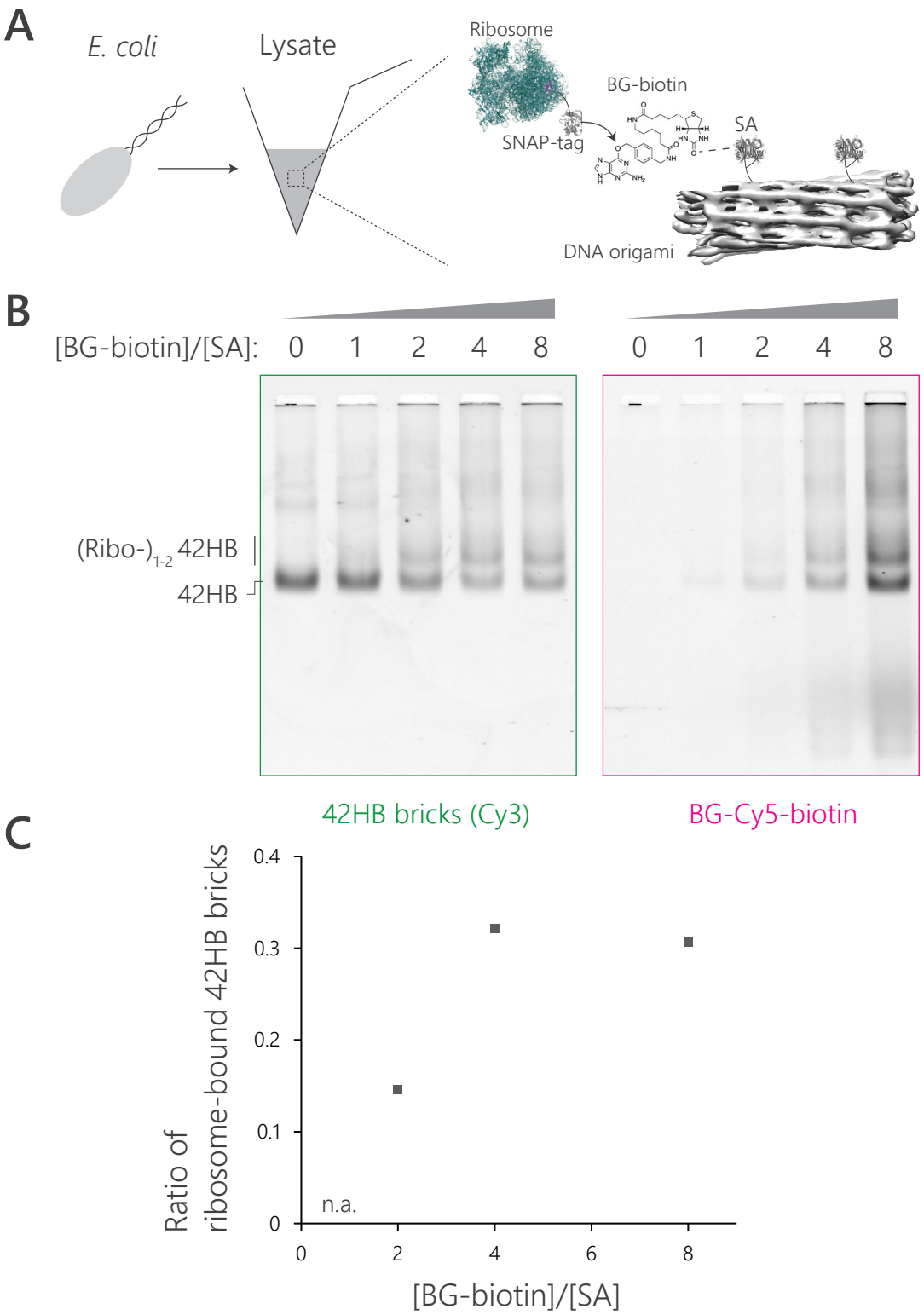

Fig. 43 | BG-biotin-dependent binding of SNAP-tagged ribosomes in *E. coli* lysate to the SA-labeled 42HB brick

(A) Schematic of ribosome assembly in *E. coli* lysate. An *E. coli* strain which expresses SNAP-tagged L20 was used to prepare a cell lysate containing SNAP-tagged ribosomes. Ribosomes in the cell lysate were biotinylated and bound to SA-labeled 42HB bricks. (B) Images of 2.0% agarose gel showing mobility shifts of the SA-labeled 42HB brick possibly bound to SNAP-tagged ribosomes in *E. coli* lysate. Cell lysate was prepared from *E. coli* expressing SNAP-tagged L20. The SNAP-tagged L20 was pre-biotinylated with different concentrations of BG-biotin (which contains 5% BG-Cy5-biotin) and then incubated with the Cy3-labeled 42HB brick containing two SA molecules. The amount of BG-biotin is shown as a molar ratio to SA. 42HB, the 42HB brick; Ribo, possible ribosomes. (C) Quantification of an image in (B). The vertical axis shows fractions of the 42HB brick with shifted mobility (bound to more than one ribosome), estimated from fluorescence density of Cy3. n.a., not applicable. Excess amounts of free BG-biotin and unassembled SNAP-tagged L20 and truncated SNAP-tag proteins in the lysate occupy the binding pocket of SA and obstruct ribosomal assembly onto the SA-labeled 42HB brick.

E. coli lysate mixed with the 42HB brick was undergone SDG centrifugation. The 42HB brick and complexes were obtained in fractions with low absorbances at 280 nm, suggesting low level of contamination by other components from the lysate (Fig. 44A). Similar to the experiment with purified ribosomes, mobility shift of the 42HB brick was observed in some fractions, suggesting binding of ribosomes to the 42HB brick in these fractions (Fig. 44B). Multimers were also obtained in later fractions. These samples were concentrated and observed with cryo-EM.

The possible complexes of a 42HB brick and a ribosome purified from the lysate were visualized using cryo-EM (Fig. 45). SPA showed several class averages regarding ribosomes (Fig. 46, A and B). Surprisingly, a density map of the 70S ribosome was majorly reconstructed (Fig. 46, C-E), which is in sharp contrast to the reconstitution of the 50S ribosome subunit using purified ribosomes. The reconstructed density map had no densities corresponding to tRNA or mRNA, showing an empty 70S ribosome (Fig. 46F).

The density of POI particles on a micrograph is important for SPA, which raises the necessity to capture POI efficiently with high purity. To improve the efficiency of ribosomal assembly to the 42HB brick, the number of SA on the 42HB brick was increased, which improved the binding ratio of ribosomes to the 42HB brick (Fig. 47). Therefore, the 42HB brick with eight SA molecules was used to capture SNAP-tagged ribosomes in cell lysate and then purified by SDG centrifugation (Fig. 48). Cryo-EM measurements visualized the purified, ribosome-bound 42HB brick and possibly dissociated ribosomes (Fig. 49). The 42HB brick had a few globular densities in the vicinity (Fig. 49B), suggesting the binding of more than two ribosomes to it. Two-dimensional class averages likely relating to ribosomes were majorly obtained by 2D classification (Fig. 50, A and B). Finally, the structure of the 70S ribosome was reconstructed with a global resolution of 6 Å from 23,288 selected particles extracted from 666

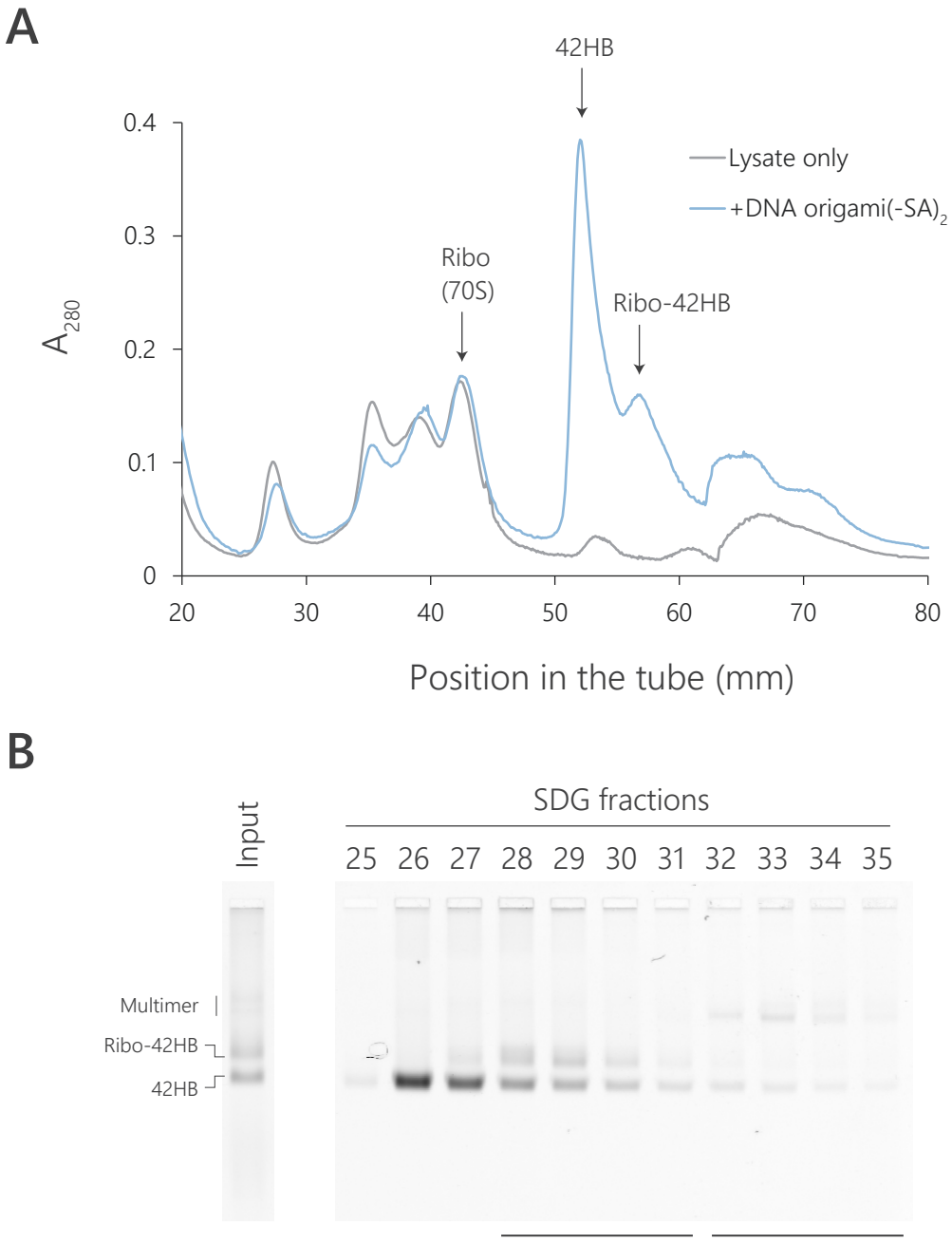

Fig. 44 | SDG centrifugation of the 42HB brick with *E. coli* lysate containing SNAP-tagged ribosomes

(A) SDG profiles of *E. coli* lysate only and of the SA-labeled 42HB brick incubated with the lysate. *E. coli* lysate containing SNAP-tagged L20 subunit was pre-biotinylated with BG-biotin/BG-Cy5-biotin, mixed with 7.2 pmol 42HB brick with two SAs [42HB(-SA)$_2$] at a SA/biotin molar ratio of 1:4, and then applied on 10–40% sucrose gradient. (B) An image of 2.0% agarose gel showing possible ribosome-bound 42HB bricks in SDG fractions. The fluorescence of BG-Cy5-biotin was detected. Fractions containing the 42HB brick (Cy3 fluorescence) were applied on the gel. Fractions used for cryo-EM measurements are annotated with solid lines. 42HB, the 42HB brick; Ribo, possible ribosomes.

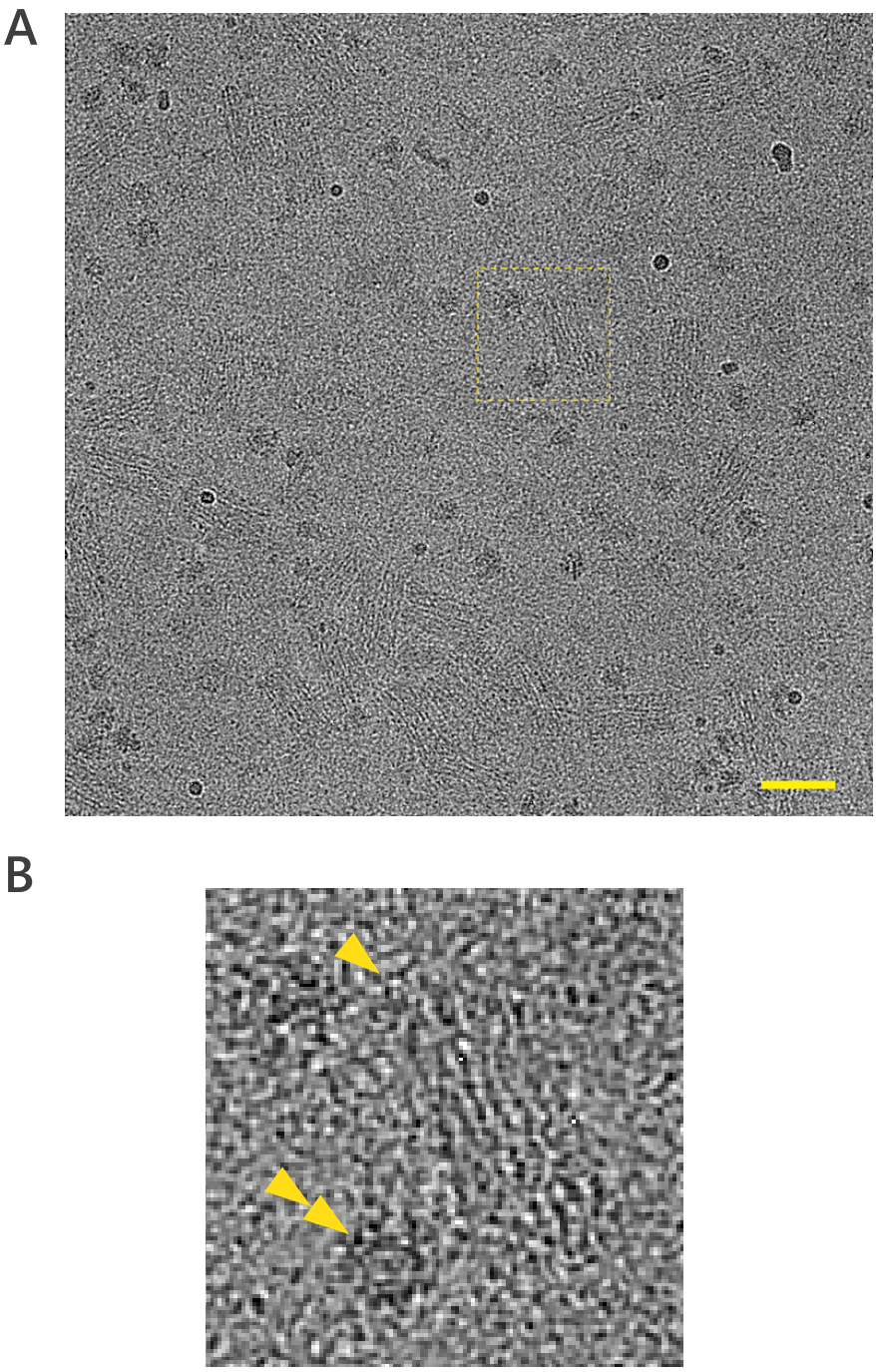

Fig. 45 | Possible 42HB bricks and ribosomes were observed from the 42HB brick purified from *E. coli* lysate

(A) An image of a grid with a thin carbon layer. The 42HB(-SA)$_2$ brick was incubated with biotinylated *E. coli* lysate. After purification by SDG centrifugation, the concentrated sample was applied on the grid. Scale bar, 50 nm. (B) A zoomed view of a particle indicated with the dashed square in (A). Single and double arrowheads denote a possible 42HB brick and a ribosome, respectively.

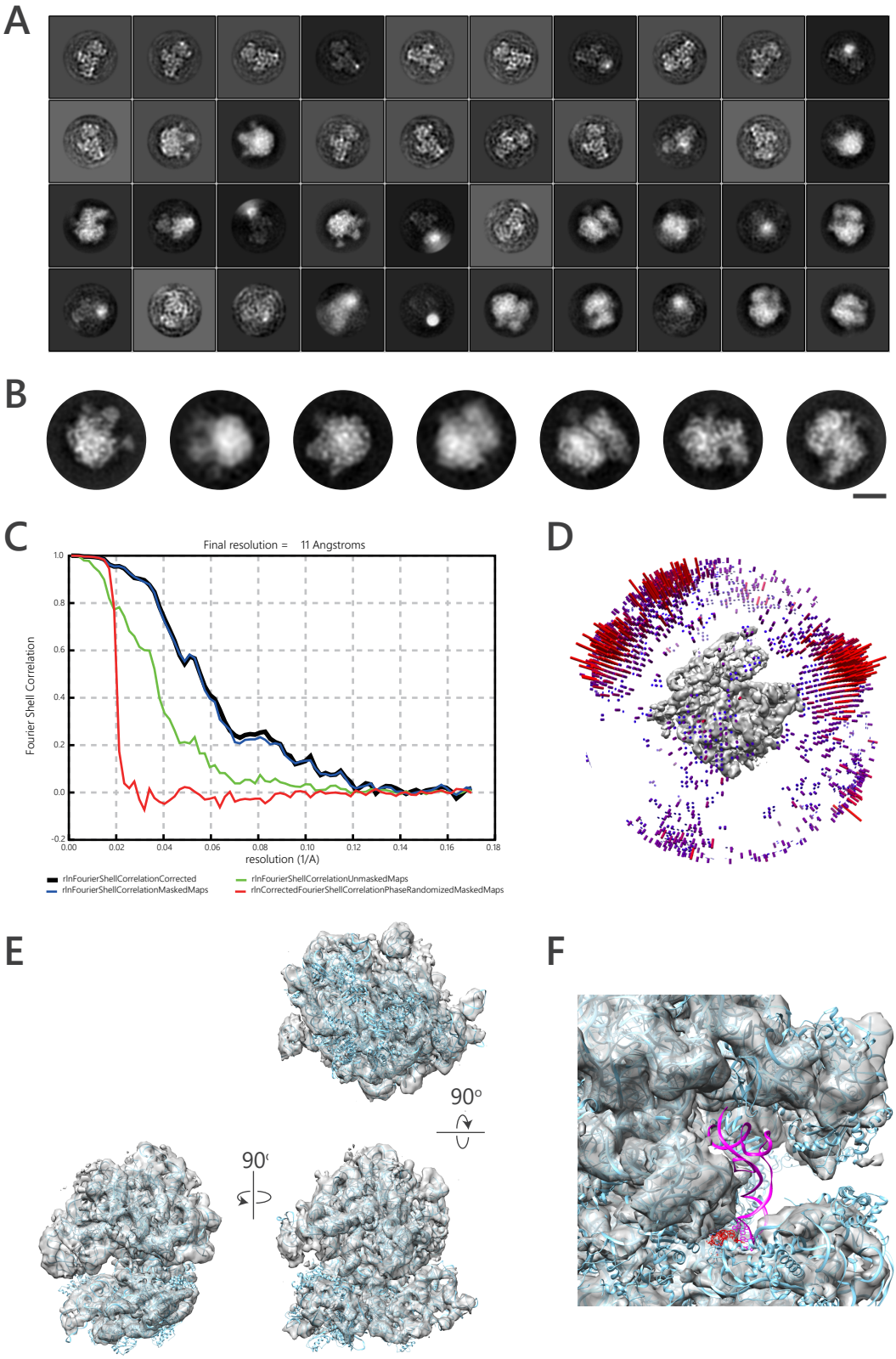

Fig. 46 | The 70S ribosome was reconstructed from the ribosome-bound 42HB brick purified from *E. coli* lysate

(A) Representative 2D Class averages obtained from dataset of ribosome-bound 42HB(-SA)$_2$ purified from *E. coli* lysate. Particles were picked using reference 2D Class averages of 70S ribosomes. (B) Representative, selected 2D Class averages showing clear ribosome structures. Scale bar, 10 nm. (C) FSC plot showing a global resolution of 11 Å. Results were obtained from 1,685 selected particles extracted from 594 images. (D) 3D histogram illustrating orientation distribution of particles. (E) Reconstructed 3D density map (semi-transparent gray) superimposed with a model of the 70S ribosome previously reported (PDB, 4V4A; cyan). (F) An image highlighting the tRNA-binding pocket of the reconstructed ribosome density map (transparent), which was superimposed with the P-site of the 70S ribosome containing mRNA and tRNA (PDB, 6O9K). red, mRNA; magenta, tRNA; cyan, others in 6O9K.

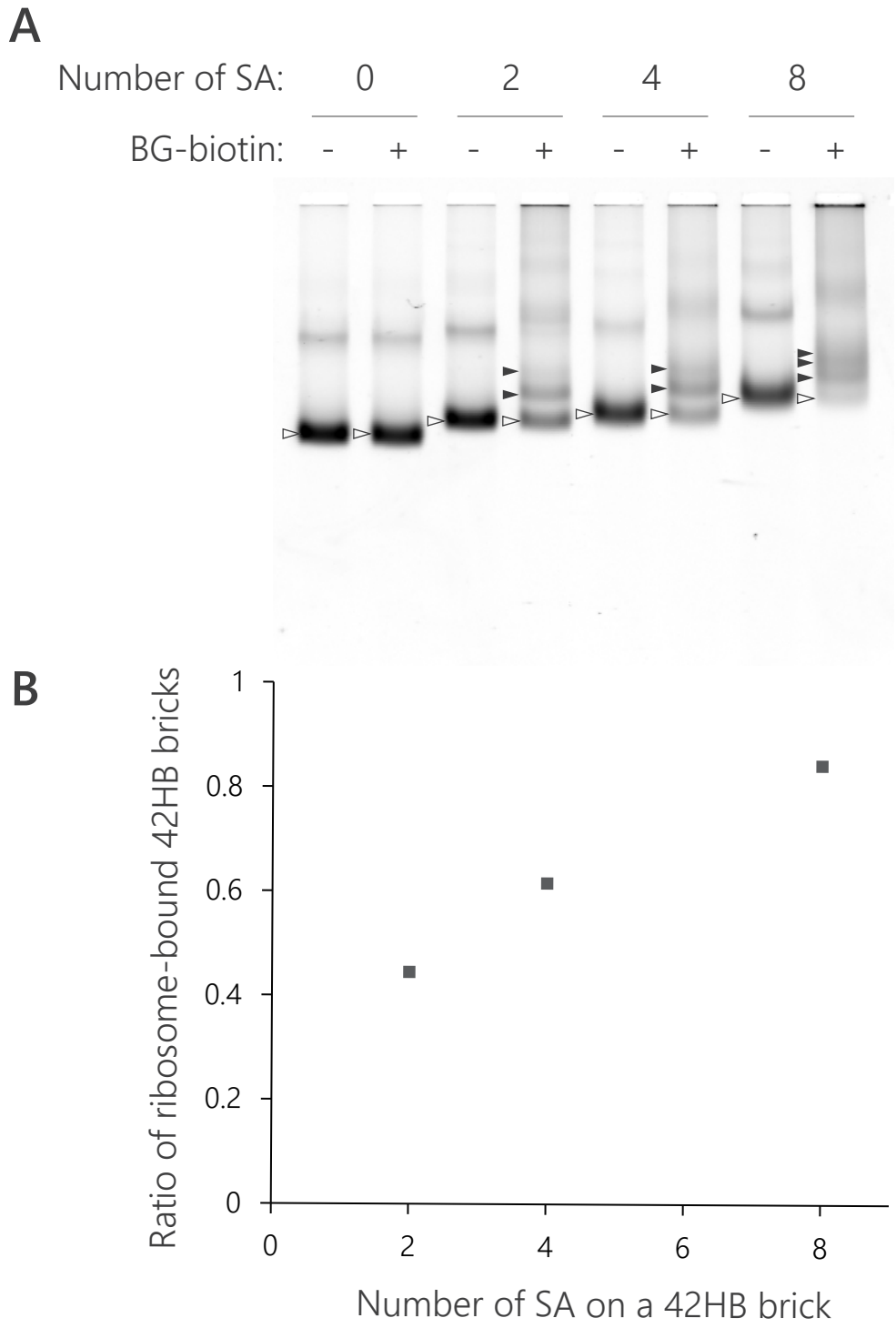

Fig. 47 | SNAP-tagged ribosomes in *E. coli* lysate bound to SA-labeled 42HB bricks depending on the number of SA

(A) Images of 2.0% agarose gel showing mobility shifts of 42HB bricks with different numbers of SA molecules. Cy3-labeled 42HB bricks were detected by fluorescence. *E. coli* lysate containing SNAP-tagged L20 (50S ribosome) was pre-incubated with or without BG-biotin/BG-Cy5-biotin mixture and further incubated with Cy3-labeled 42HB bricks occupied with zero, two, four, or eight molecules of SA at a SA/biotin molar ratio of 1:4. Open and filled arrowheads denote free 42HB bricks and 42HB bricks bound to more than one molecule of the ribosome, respectively. The mobility of 42HB brick depends on the number of SA(s). (B) Quantification of the binding ratio. The vertical axis shows fractions of the 42HB brick with shifted mobility (bound to more than one ribosome).

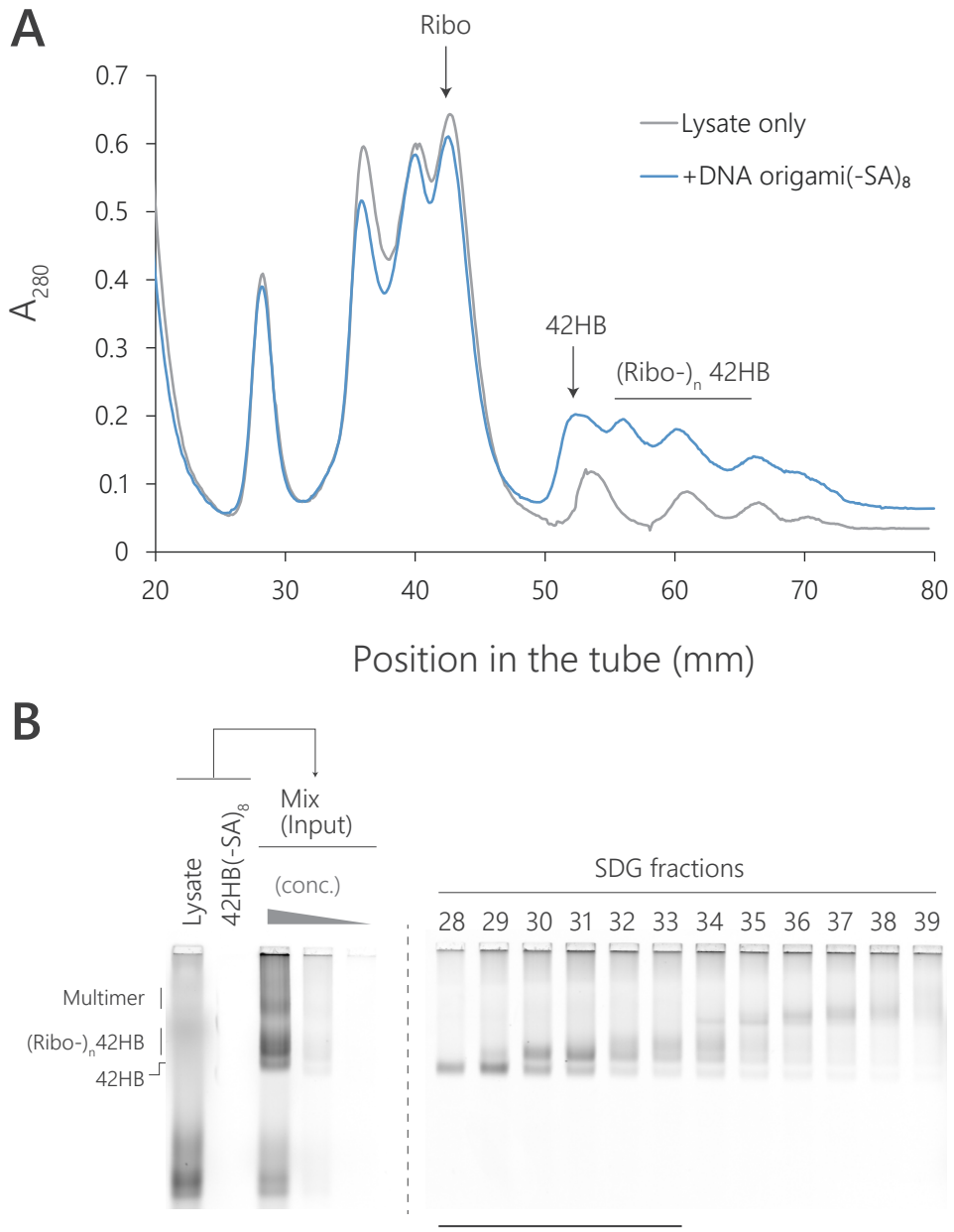

Fig. 48 | SDG centrifugation of the 42HB(-SA)$_8$ brick with *E. coli* lysate containing SNAP-tagged ribosomes

(A) SDG profiles of *E. coli* lysate only and of the 42HB brick with 8 SAs [42HB(-SA)$_8$] incubated with the lysate. *E. coli* lysate containing SNAP-tagged L20 subunit was pre-biotinylated with BG-biotin/BG-Cy5-biotin mixture. The lysate was mixed with 6.8 pmol 42HB(-SA)$_8$ brick at a SA/biotin molar ratio of 1:4, and then applied on 10–40% sucrose gradient. (B) An image of 2.0% agarose gel showing 42HB bricks bound to more than one ribosome. The fluorescence of BG-Cy5-biotin was detected. Fractions containing 42HB (Cy3 fluorescence) were applied on the gel. Fractions used for cryo-EM measurements are indicated with solid lines. 42HB, the 42HB brick; Ribo, possible ribosomes.

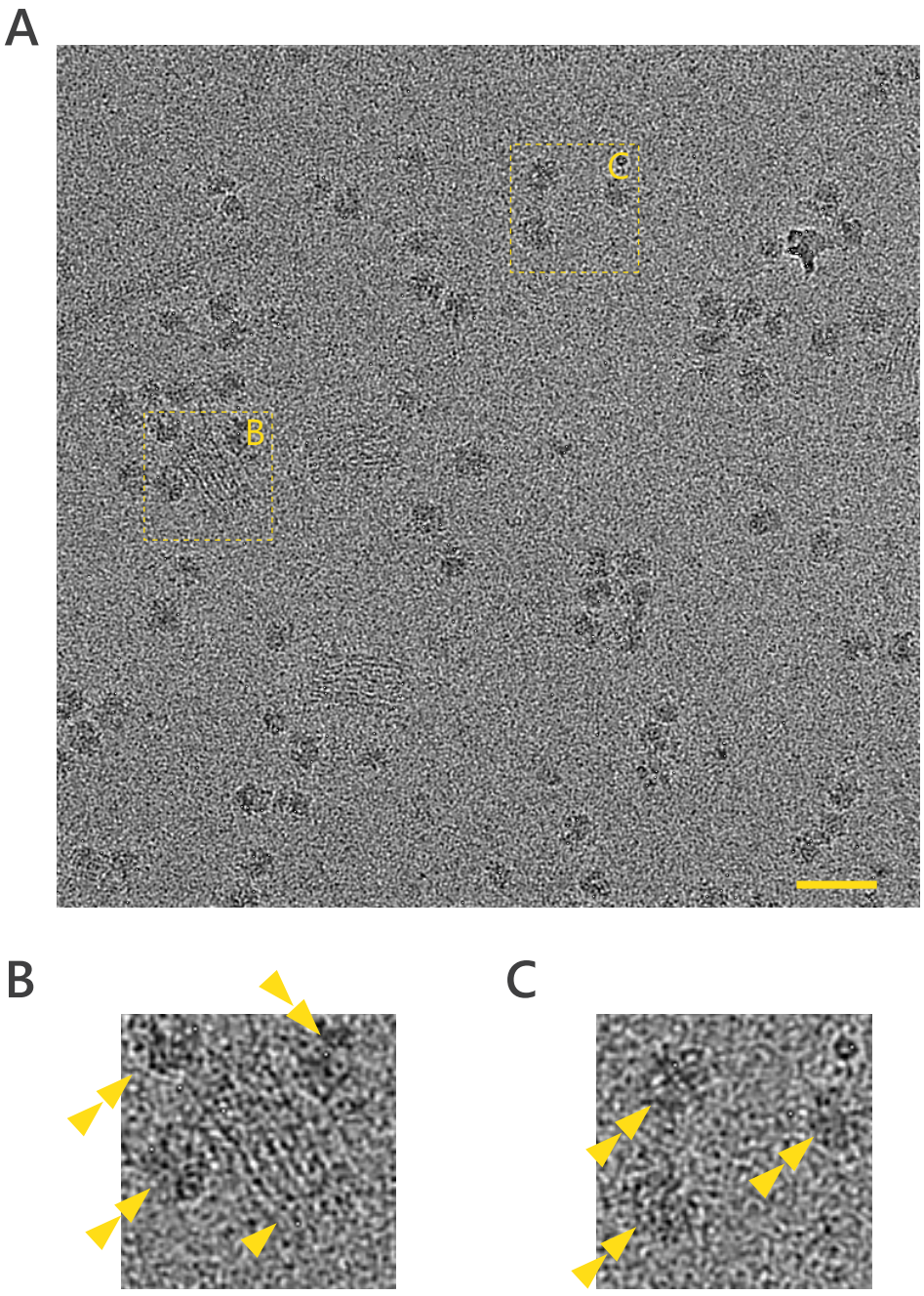

Fig. 49 | The mixture of ribosome-bound 42HB bricks and ribosomes were observed in the *E. coli* lysate sample purified by the 42HB(-SA)$_8$ brick

(A) An image of a grid with a thin carbon layer. The 42HB(-SA)$_8$ brick was incubated with biotinylated *E. coli* lysate. After purification by SDG centrifugation, the concentrated sample was applied on the grid. Scale bar, 50 nm. (B and C) Zoomed views of a possible 42HB brick (B) and dissociated, free ribosomes (C), indicated with dashed squares in (A). Single and double arrowheads denote a possible 42HB brick and a ribosome, respectively.

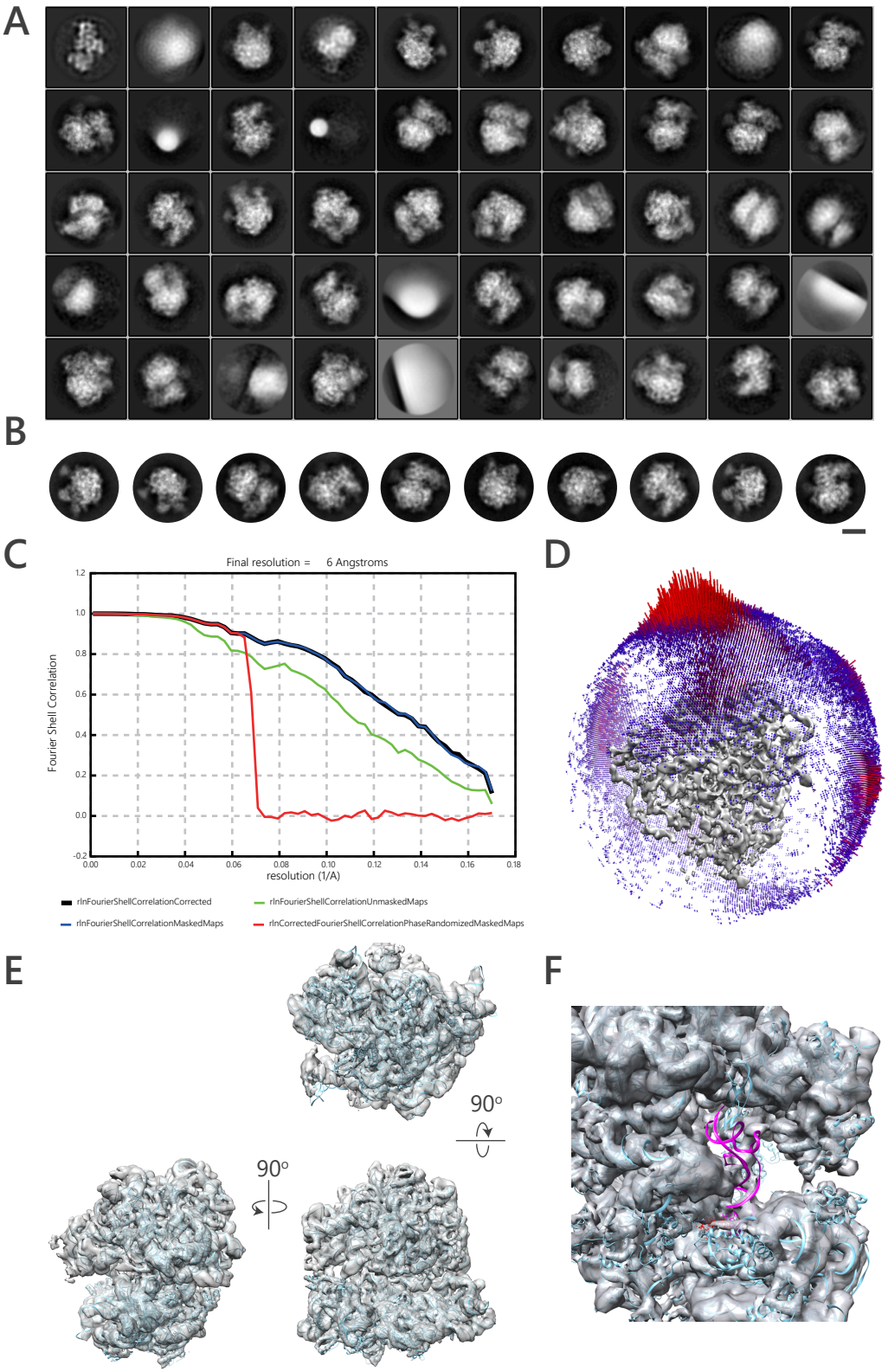

Fig. 50 | The 70S ribosome was reconstructed from *E. coli* lysate purified with the 42HB(-SA)$_8$ brick

(A) Representative 2D Class averages. Particles were picked with reference 2D Class averages of 70S ribosomes from images relating to ribosome-bound 42HB(-SA)$_8$ bricks purified from *E. coli* lysate. (B) Representative, selected 2D Class averages showing clear ribosome structures. Scale bar, 10 nm. (C) FSC plot showing a global resolution of 6 Å. Results obtained from 23,288 selected particles extracted from 666 images. (D) 3D histogram illustrating the orientation distribution of particles. (E) Reconstructed 3D density map (semi-transparent gray) superimposed with a model of the 70S ribosome previously reported (PDB, 4V4A; cyan). (F) An image highlighting the tRNA-binding pocket of the reconstructed ribosome density map (transparent), which was superimposed with the P-site of the 70S ribosome containing mRNA and tRNA (PDB, 6O9K). red, mRNA; magenta, tRNA; cyan, others in 6O9K.

micrographs (Fig. 50, C-E), indicating increase in the number of selected particles per a micrograph from 3 (two SA) to 35 (eight SA) (Supplementary Table 8). The map contained a clear mRNA and modest tRNA density (Fig. 50F), suggesting a translating form of the ribosome that was possibly formed within cells. These results indicate that the capturing system I established in this section can be utilized to purify and visualize a SNAP-tagged macromolecule from *E. coli* lysate.

II-4. Discussion

In this part, I introduce an experimental system, that was used to capture a model macromolecule, the ribosome, in an *E. coli* lysate, and provide a cryo-EM-based analysis of the structure of the captured macromolecule. Purification via SDG centrifugation was used to successfully separate ribosome-bound DNA origami nanoparticles from free, unbound ribosomes. To the best of my knowledge, this is the first demonstration of a native POI, that was pre-existing in an isolate, being captured via DNA origami nanoparticles and its structure begin reconstructed at semi-high resolutions (6–11 Å). Some studies have previously analyzed the structures of POIs that were integrated with DONs immediately after mixing and without purification (Aissaoui et al., 2021; Aksel et al., 2021; Dong et al., 2018; Martin et al., 2016). On the other hand, Mei et al. isolated the protein, thrombin, from a cell lysate by binding it to a DON using microchip isotachophoresis; however, the purified thrombin was one that had been used to supplement the cell lysate and not one that had pre-existed in the cell lysate (Mei et al., 2013). The SDG-based purification system established by the current study used a DON to isolate a native POI that had been expressed in an *E. coli* lysate. As a result, the structure of the 70S ribosome derived from the cell lysate could be reconstructed. However, this reconstruction was different from reconstruction of a 50S ribosome obtained from purified ribosomes using the

same purification procedure (Fig. 46 vs. Fig. 40), where it appears that the ribosome structures reflecting their native form in cells were visualized.

Ability to manage the numbers and layouts of multiple binder modules on a nanostructure is one of the most useful advantages of DNA origami technology. A pioneering study have shown that the ability of a DON to bind a protein, such as thrombin, depends on the layout of its two binder modules (Rinker et al., 2008). Another study has quantitatively shown that the layout of a ligand on a DON may affect the affinity between that ligand and a receptor (Bila et al., 2022). The results in part I also highlighted the controllability of molecular layouts on DONs. Although this study used a simple SA-biotin binding system, the fact that a POI can be successfully purified using a DNA origami carrier indicates the possibility of achieving multivalent purification via the use of spatially controlled binder modules on DONs.

Further improvement is needed before the current system can be applied to a wide variety of POIs and/or multivalent purification procedures. Firstly, prior knowledge of the expression level of the POI in the cell lysate is critical for its capture particularly because the SA-biotin binding system requires over 100 nM target molecules for assembly in the cell lysate of 1 mg/mL protein. The use of multivalent binding which improves affinity between DONs and POIs usually addresses this issue. However, since multivalent binding needs modestly fast dissociation constants to achieve equilibrium, SA-biotin has to be replaced with other binder modules, such as antibodies, in order to ensure multivalent purification. My current objective is to overcome the afore mentioned technical issues which are associated with affinity and multivalent binding. Thirdly, the low throughput of SDG centrifugation needs to be addressed. Only a maximum of 6 samples can be simultaneously centrifuged using a typical ultracentrifuge rotor, a process which takes 3 h for ultracentrifugation and another approximately 0.2 h per sample for fraction collection. Although this is not a critical disadvantage, since cryo-EM

measurement itself is a rate-limiting process, it has to be addressed when applying DNA origami-based purification. Actually, all known advantageous characteristics of ribosomes were utilized in this study; for example, ribosomes are absorbed on carbon layers on grids, which functions as a type of ribosome “purification” process. This shows that ribosome-associated complexes, such as translation complexes and the expressome, are good targets for application of this experimental system. In summary, the DON-based system will provide a fundamental platform to prepare ribosome-related super-complexes for structural analysis.

General Discussion and Conclusions

Many studies have shown that DNA origami provides an ideal scaffold that can be utilized to create nanostructures in terms of precise spatial control and functionalization (Dey et al., 2021; Endo et al., 2013; Hong et al., 2017); hence, some studies have used the advantages conferred by spatial controllability in DONs to evaluate the structures and functions of POIs. Difficulties in POI-assembly and purification of DON-POI complexes pose major challenges to the application of *in-vitro* analyses. In this study, I have proposed experimental systems that may help solve the following technical challenges: (i) efficient assembly of POIs on a DON using poly-lysine (part I); and (ii) purification of DON-POI complexes via SDG centrifugation (part II). Both these are technical improvements aimed at avoiding the effect of free unbound proteins, and thus may play an important role in analysis of DON-assembled POIs. A combination of these two independent systems may especially be useful for assembling and purifying DON-POI complexes. In addition, the findings pertaining to kinesin-based transporters described in part I reveal the advantages associated with DNA origami nanotechnology as well as the controllability of the number and layout of assembled POIs (Figs. 20, 23, 26, 28, and 30). Minimal non-specific interaction with POIs is another strength of DONs. Unexpected binding between a DON and POI was not detected in both experiments (Figs. 8, 18, and 36) unlike in beads (Fig. 37). These results indicate that DNA origami shows much potential as a technique that can be gainfully utilized in the assembly and purification of POIs.

Both experimental systems that were built combined DNA origami nanotechnology with single-particle imaging approaches; single-molecule fluorescence imaging in part I, and cryo-EM SPA in part II. Despite improvements in the efficiency of POI-purification and assembly, free proteins remain within the samples of DON-POI complexes. The single-particle approaches

made it possible to distinguish DON-bound-POI from other particles as also to specifically analyze complexes of interest (Figs. 17 and 39). High-speed atomic force microscopy used by previous studies (Endo et al., 2010; Fujita et al., 2019; Rinker et al., 2008; Saccà et al., 2010) may also be helpful in regard to these issues. On the other hand, precise biochemical analysis of DON-assembled POIs continues to be affected due to contamination by free POIs, thereby limiting the versality of the DON-POI approach. This issue may be addressed in future studies by combining the two approaches developed in the current study and/or further advanced methods that may be utilized for the assembly and purification of DON-POI complexes.

In conclusion, two experimental systems that can be utilized to evaluate the function and structure of biological macromolecules were established. The first system enables the second system allows the assembly of tag-protein-fused POIs on DONs via high binding kinetics. This system was applied to evaluate the effect of spatial proximity between kinesin proteins at the single-molecule level. The second system allowed purification and cryo-EM-based observation of SNAP-tagged POIs in an *E. coli* lysate, showing a potential application of DONs as purification carriers. In cells, mesoscale super-complexes play an important role in the regulation of biological functions. Determining whether the intermolecular layouts in these super-complexes affect their function, and if so in what manner, may be vital for understanding the underlying molecular mechanisms. Combining DNA origami nanotechnology with single-particle imaging approach enables a broader understanding of intermolecular-layout effects. Experimental systems that may be proposed based on the findings of this study may expectedly provide a fundamental platform via which the effects exerted by the intermolecular layouts of POIs on their structures and functions can be studied in depth.

Acknowledgements

I would like to express my deepest appreciation to Prof. Hisashi Tadakuma for providing an opportunity to study DNA origami nanotechnology and supervising all aspects of my work. His constructive suggestions and discussion have helped me start and complete this study. I also appreciate Prof. Yoshie Harada and Prof. Shun-ichi Sekine regarding parts I and II, respectively, for giving valuable opportunities, comments, and discussion. I would also like to express my gratitude to Dr. Yuko Murayama, Dr. Haruhiko Ehara and Dr. Tatsuo Yanagisawa for suggestions and comments regarding cryo-EM and SPA. Dr. Yuya Miyazono provided prior research and experimental procedures for part I. Prof. Koichi Ito provided *E. coli* strains for the expression of SNAP-tagged ribosomes. Prof. Takuhiro Ito, Dr. Wakana Iwasaki, and Ms. Mari Takahashi had discussion about ribosomes and provided a protocol for SDG centrifugation. Mr. Yuxiang Liu designed and prepared 42HB bricks. Mr. Bingxun Wang prepared BG-Cy5-biotin. I deeply appreciate their contributions to complete the current study. I also appreciate Prof. Keiko Hirose for evaluating DONs for part I and providing new insights on motile complexes. I would like to express my gratitude for Prof. Takahide Kon and Prof. Genji Kurisu for providing constructive comments on this thesis. I would also like to thank all members of Laboratory for Nanobiology (Institute for Protein Research, Osaka University) and Laboratory for Transcription Structural Biology (Center for Biosystems Dynamics Research, RIKEN), for their helpful comments and discussion. This study was supported by a Grant-in-Aid for Japan Society for the Promotion of Science Research Fellows. I would like to thank Editage (www.editage.com) for English language editing.

References

Abdella, R., Talyzina, A., Chen, S., Inouye, C.J., Tjian, R., and He, Y. (2021). Structure of the human Mediator-bound transcription preinitiation complex. Science (80-.). *372*, 52–56.

Abdellatef, S.A., Tadakuma, H., Yan, K., Fujiwara, T., Fukumoto, K., Kondo, Y., Takazaki, H., Boudria, R., Yasunaga, T., Higuchi, H., et al. (2022). Oscillatory movement of a dynein-microtubule complex crosslinked with DNA origami. Elife *11*, 1–20.

Aissaoui, N., Lai-Kee-Him, J., Mills, A., Declerck, N., Morichaud, Z., Brodolin, K., Baconnais, S., Le Cam, E., Charbonnier, J.B., Sounier, R., et al. (2021). Modular Imaging Scaffold for Single-Particle Electron Microscopy. ACS Nano *15*, 4186–4196.

Akitaya, T., Seno, A., Nakai, T., Hazemoto, N., Murata, S., and Yoshikawa, K. (2007). Weak interaction induces an ON/OFF switch, whereas strong interaction causes gradual change: Folding transition of a long duplex DNA chain by poly-L-lysine. Biomacromolecules *8*, 273–278.

Aksel, T., Yu, Z., Cheng, Y., and Douglas, S.M. (2021). Molecular goniometers for single-particle cryo-electron microscopy of DNA-binding proteins. Nat. Biotechnol. *39*, 378–386.

Ally, S., Larson, A.G., Barlan, K., Rice, S.E., and Gelfand, V.I. (2009). Opposite-polarity motors activate one another to trigger cargo transport in live cells. J. Cell Biol. *187*, 1071–1082.

Aoki, T., Tomishige, M., and Ariga, T. (2013). Single molecule FRET observation of kinesin-1's head-tail interaction on microtubule. Biophys. *9*, 149–159.

Beeg, J., Klumpp, S., Dimova, R., Gracià, R.S., Unger, E., and Lipowsky, R. (2008). Transport of beads by several kinesin motors. Biophys. J. *94*, 532–541.

Berger Bioucas, F.E., Damm, C., Peukert, W., Rausch, M.H., Koller, T.M., Giraudet, C., and Fröba, A.P. (2019). Translational and Rotational Diffusion Coefficients of Gold Nanorods Dispersed in Mixtures of Water and Glycerol by Polarized Dynamic Light Scattering. J. Phys. Chem. B *123*, 9491–9502.

Bieling, P., Telley, I.A., Piehler, J., and Surrey, T. (2008). Processive kinesins require loose mechanical coupling for efficient collective motility. EMBO Rep. *9*, 1121–1127.

Bila, H., Paloja, K., Caroprese, V., Kononenko, A., and Bastings, M.M.C. (2022). Multivalent Pattern Recognition through Control of Nano-Spacing in Low-Valency Super-Selective Materials. J. Am. Chem. Soc. *2022*, 21576–21586.

Castro, C.E., Kilchherr, F., Kim, D.N., Shiao, E.L., Wauer, T., Wortmann, P., Bathe, M., and Dietz, H. (2011). A primer to scaffolded DNA origami. Nat. Methods *8*, 221–229.

Chen, X., Yin, X., Li, J., Wu, Z., Qi, Y., Wang, X., Liu, W., and Xu, Y. (2021). Structures of the human

Mediator and Mediator-bound preinitiation complex. Science (80-.). *372*.

Derr, N.D., Goodman, B.S., Jungmann, R., Leschziner, A.E., Shih, W.M., and Reck-Peterson, S.L. (2012). Tug-of-War in Motor Protein Ensembles Revealed with a Programmable DNA Origami Scaffold. Science (80-.). *338*, 662–666.

Dey, S., Fan, C., Gothelf, K. V., Li, J., Lin, C., Liu, L., Liu, N., Nijenhuis, M.A.D., Saccà, B., Simmel, F.C., et al. (2021). DNA origami. Nat. Rev. Methods Prim. 2021 11 *1*, 1–24.

Dong, Y., Chen, S., Zhang, S., Sodroski, J., Yang, Z., Liu, D., and Mao, Y. (2018). Folding DNA into a Lipid-Conjugated Nanobarrel for Controlled Reconstitution of Membrane Proteins. Angew. Chemie *130*, 2094–2098.

Douglas, S.M., Dietz, H., Liedl, T., Högberg, B., Graf, F., and Shih, W.M. (2009). Self-assembly of DNA into nanoscale three-dimensional shapes. Nature *459*, 414–418.

Ehara, H., Yokoyama, T., Shigematsu, H., Yokoyama, S., Shirouzu, M., and Sekine, S.I. (2017). Structure of the complete elongation complex of RNA polymerase II with basal factors. Science (80-.). *357*, 921–924.

Endo, M., Katsuda, Y., Hidaka, K., and Sugiyama, H. (2010). Regulation of DNA methylation using different tensions of double strands constructed in a defined DNA nanostructure. J. Am. Chem. Soc. *132*, 1592–1597.

Endo, M., Yang, Y., and Sugiyama, H. (2013). DNA origami technology for biomaterials applications. Biomater. Sci. *1*, 347–360.

Feller, D., Otten, M., Hildebrandt, M., Krüsmann, M., Bryant, G., and Karg, M. (2021). Translational and rotational diffusion coefficients of gold nanorods functionalized with a high molecular weight, thermoresponsive ligand: a depolarized dynamic light scattering study. Soft Matter *17*, 4019–4026.

Feng, Q., Mickolajczyk, K.J., Chen, G.Y., and Hancock, W.O. (2018). Motor Reattachment Kinetics Play a Dominant Role in Multimotor-Driven Cargo Transport. Biophys. J. *114*, 400–409.

Fujita, K., Ohmachi, M., Ikezaki, K., Yanagida, T., and Iwaki, M. (2019). Direct visualization of human myosin II force generation using DNA origami-based thick filaments. Commun. Biol. *2*.

Furuta, K., Furuta, A., Toyoshima, Y.Y., Amino, M., Oiwa, K., and Kojima, H. (2013). Measuring collective transport by defined numbers of processive and nonprocessive kinesin motors. Proc. Natl. Acad. Sci. *110*, 501–506.

Gan, L., and Jensen, G.J. (2012). Electron tomography of cells. Q. Rev. Biophys. *45*, 27–56.

Gerling, T., Kube, M., Kick, B., and Dietz, H. (2018). Sequence-programmable covalent bonding of designed DNA assemblies. Sci. Adv. *4*, 1–12.

Goddard, T.D., Huang, C.C., Meng, E.C., Pettersen, E.F., Couch, G.S., Morris, J.H., and Ferrin, T.E. (2018). UCSF ChimeraX: Meeting modern challenges in visualization and analysis. Protein Sci. *27*, 14–25.

Goodsell, D.S., Olson, A.J., and Forli, S. (2020). Art and Science of the Cellular Mesoscale. Trends Biochem. Sci. *45*, 472–483.

Hao, Z., Epshtein, V., Kim, K.H., Proshkin, S., Svetlov, V., Kamarthapu, V., Bharati, B., Mironov, A., Walz, T., and Nudler, E. (2021). Pre-termination Transcription Complex: Structure and Function. Mol. Cell 1–12.

Hariadi, R.F., Sommese, R.F., Adhikari, A.S., Taylor, R.E., Sutton, S., Spudich, J.A., and Sivaramakrishnan, S. (2015). Mechanical coordination in motor ensembles revealed using engineered artificial myosin filaments. Nat. Nanotechnol. *10*, 696–700.

Hariadi, R.F., Appukutty, A.J., and Sivaramakrishnan, S. (2016). Engineering Circular Gliding of Actin Filaments Along Myosin-Patterned DNA Nanotube Rings to Study Long-Term Actin-Myosin Behaviors. ACS Nano *10*, 8281–8288.

Hendricks, A.G., Perlson, E., Ross, J.L., Schroeder, H.W., Tokito, M., and Holzbaur, E.L.F. (2010). Motor Coordination via a Tug-of-War Mechanism Drives Bidirectional Vesicle Transport. Curr. Biol. *20*, 697–702.

Hirokawa, N., Niwa, S., and Tanaka, Y. (2010). Molecular motors in neurons: Transport mechanisms and roles in brain function, development, and disease. Neuron *68*, 610–638.

Hong, F., Zhang, F., Liu, Y., and Yan, H. (2017). DNA Origami: Scaffolds for Creating Higher Order Structures.

Howard, J., Hudspeth, A.J., and Vale, R.D. (1989). Movement of microtubules by single kinesin molecules. Nat. 1989 3426246 *342*, 154–158.

Ibusuki, R., Shiraga, M., Furuta, A., Yoshio, M., Kojima, H., Oiwa, K., and Furuta, K. (2020). Collective motility of dynein linear arrays built on DNA nanotubes. Biochem. Biophys. Res. Commun. *523*, 1014–1019.

Ibusuki, R., Morishita, T., Furuta, A., Nakayama, S., Yoshio, M., Kojima, H., Oiwa, K., and Furuta, K. (2022). Programmable molecular transport achieved by engineering protein motors to move on DNA nanotubes. Science (80-.). *375*, 1159–1164.

Koßmann, K.J., Ziegler, C., Angelin, A., Meyer, R., Skoupi, M., Rabe, K.S., and Niemeyer, C.M. (2016). A Rationally Designed Connector for Assembly of Protein-Functionalized DNA Nanostructures. ChemBioChem 1102–1106.

Kozlowski, L.P. (2016). IPC - Isoelectric Point Calculator. Biol. Direct *11*, 55.

Krementsova, E.B., Furuta, K., Oiwa, K., Trybus, K.M., and Ali, M.Y. (2017). Small teams of myosin Vc motors coordinate their stepping for efficient cargo transport on actin bundles. J. Biol. Chem. *292*, 10998–11008.

Kröll, S., Rabe, K.S., and Niemeyer, C.M. (2021). An Orthogonal Covalent Connector System for the Efficient Assembly of Enzyme Cascades on DNA Nanostructures. Small *17*.

Kröll, S., Schneider, L., Wadhwani, P., Rabe, K.S., and Niemeyer, C.M. (2022). Orthogonal protein decoration of DNA nanostructures based on SpyCatcher–SpyTag interaction. Chem. Commun. *58*, 13471–13474.

Kunwar, A., Vershinin, M., Xu, J., and Gross, S.P. (2008). Stepping, Strain Gating, and an Unexpected Force-Velocity Curve for Multiple-Motor-Based Transport. Curr. Biol. *18*, 1173–1183.

Kyrilis, F.L., Semchonok, D.A., Skalidis, I., Tüting, C., Hamdi, F., O'Reilly, F.J., Rappsilber, J., and Kastritis, P.L. (2021). Integrative structure of a 10-megadalton eukaryotic pyruvate dehydrogenase complex from native cell extracts. Cell Rep. *34*.

Lieberman-Aiden, E., Van Berkum, N.L., Williams, L., Imakaev, M., Ragoczy, T., Telling, A., Amit, I., Lajoie, B.R., Sabo, P.J., Dorschner, M.O., et al. (2009). Comprehensive mapping of long-range interactions reveals folding principles of the human genome. Science (80-.). *326*, 289–293.

Liu, C.C., and Schultz, P.G. (2010). Adding New Chemistries to the Genetic Code. Https://Doi.Org/10.1146/Annurev.Biochem.052308.105824 *79*, 413–444.

Liu, Y., Miao, K., Dunham, N.P., Liu, H., Fares, M., Boal, A.K., Li, X., and Zhang, X. (2017). The Cation−π Interaction Enables a Halo-Tag Fluorogenic Probe for Fast No-Wash Live Cell Imaging and Gel-Free Protein Quantification. Biochemistry *56*, 1585–1595.

Martin, T.G., Bharat, T.A.M., Joerger, A.C., Bai, X.C., Praetorius, F., Fersht, A.R., Dietz, H., and Scheres, S.H.W. (2016). Design of a molecular support for cryo-EM structure determination. Proc. Natl. Acad. Sci. U. S. A. *113*, E7456–E7463.

Mastronarde, D.N. (2005). Automated electron microscope tomography using robust prediction of specimen movements. J. Struct. Biol. *152*, 36–51.

Masubuchi, T., Endo, M., Iizuka, R., Iguchi, A., Yoon, D.H., Sekiguchi, T., Qi, H., Iinuma, R., Miyazono, Y., Shoji, S., et al. (2018). Construction of integrated gene logic-chip. Nat. Nanotechnol. *13*, 933–940.

Matsuda, K., Kabir, A.M.R., Akamatsu, N., Saito, A., Ishikawa, S., Matsuyama, T., Ditzer, O., Islam, M.S., Ohya, Y., Sada, K., et al. (2019). Artificial Smooth Muscle Model Composed of Hierarchically

Ordered Microtubule Asters Mediated by DNA Origami Nanostructures. Nano Lett. *19*, 3933–3938.

Mei, Q., Johnson, R.H., Wei, X., Su, F., Liu, Y., Kelbauskas, L., Lindsay, S., Meldrum, D.R., and Yan, H. (2013). On-chip isotachophoresis separation of functional DNA origami capture nanoarrays from cell lysate. Nano Res. *6*, 712–719.

Miyazono, Y. (2017). DNA-蛋白質複合体による キネシンモーター蛋白質の運動機構解明 (Walking mechanism of kinesin motor protein: a DNA-kinesin hybrid nanomachine study). 東京大学 (博士論文).

Miyazono, Y., Hayashi, M., Karagiannis, P., Harada, Y., and Tadakuma, H. (2010). Strain through the neck linker ensures processive runs: a DNA-kinesin hybrid nanomachine study. EMBO J. *29*, 93–106.

Mollwitz, B., Brunk, E., Schmitt, S., Pojer, F., Bannwarth, M., Schiltz, M., Rothlisberger, U., and Johnsson, K. (2012). Directed evolution of the suicide protein O 6-alkylguanine-DNA alkyltransferase for increased reactivity results in an alkylated protein with exceptional stability. Biochemistry *51*, 986–994.

Murayama, Y., Ehara, H., Aoki, M., Goto, M., Yokoyama, T., and Sekine, S. (2023). Structural basis of the transcription termination factor Rho engagement with transcribing RNA polymerase from Thermus thermophilus. Sci. Adv. *9*.

Nakane, T., Kimanius, D., Lindahl, E., and Scheres, S.H.W. (2018). Characterisation of molecular motions in cryo-EM single-particle data by multi-body refinement in RELION. Elife *7*, 1–18.

Nakata, E., Dinh, H., Ngo, T.A., Saimura, M., and Morii, T. (2015). A modular zinc finger adaptor accelerates the covalent linkage of proteins at specific locations on DNA nanoscaffolds. Chem. Commun. *51*, 1016–1019.

Nguyen, T.M., Nakata, E., Saimura, M., Dinh, H., and Morii, T. (2017). Design of Modular Protein Tags for Orthogonal Covalent Bond Formation at Specific DNA Sequences. J. Am. Chem. Soc. *139*, 8487–8496.

Niemeyer, C.M. (2010). Semisynthetic DNA-protein conjugates for biosensing and nanofabrication. Angew. Chemie - Int. Ed. *49*, 1200–1216.

Norris, S.R., Soppina, V., Dizaji, A.S., Schimert, K.I., Sept, D., Cai, D., Sivaramakrishnan, S., and Verhey, K.J. (2014). A method for multiprotein assembly in cells reveals independent action of kinesins in complex. J. Cell Biol. *207*, 393–406.

Peet, D.R., Burroughs, N.J., and Cross, R.A. (2018). Kinesin expands and stabilizes the GDP-microtubule lattice. Nat. Nanotechnol. *13*, 386–391.

Rinker, S., Ke, Y., Liu, Y., Chhabra, R., and Yan, H. (2008). Self-assembled DNA nanostructures for distance-dependent multivalent ligand-protein binding. Nat. Nanotechnol. *3*, 418–422.

Rogers, A.R., Driver, J.W., Constantinou, P.E., Kenneth Jamison, D., and Diehl, M.R. (2009). Negative interference dominates collective transport of kinesin motors in the absence of load. Phys. Chem. Chem. Phys. *11*, 4882–4889.

Rohou, A., and Grigorieff, N. (2015). CTFFIND4: Fast and accurate defocus estimation from electron micrographs. J. Struct. Biol. *192*, 216–221.

Rothemund, P.W.K. (2006). Folding DNA to create nanoscale shapes and patterns. Nature *440*, 297–302.

Roux, K.J., Kim, D.I., Raida, M., and Burke, B. (2012). A promiscuous biotin ligase fusion protein identifies proximal and interacting proteins in mammalian cells. J. Cell Biol. *196*, 801–810.

Saccà, B., Meyer, R., Erkelenz, M., Kiko, K., Arndt, A., Schroeder, H., Rabe, K.S., and Niemeyer, C.M. (2010). Orthogonal protein decoration of DNA origami. Angew. Chemie - Int. Ed. *49*, 9378–9383.

Schmidli, C., Albiez, S., Rima, L., Righetto, R., Mohammed, I., Oliva, P., Kovacik, L., Stahlberg, H., and Braun, T. (2019). Microfluidic protein isolation and sample preparation for high-resolution cryo-EM. Proc. Natl. Acad. Sci. U. S. A. *116*, 15007–15012.

Schneider, C.A., Rasband, W.S., and Eliceiri, K.W. (2012). NIH Image to ImageJ: 25 years of image analysis. Nat. Methods *9*, 671–675.

Schneider, R., Korten, T., Walter, W.J., and Diez, S. (2015). Kinesin-1 motors can circumvent permanent roadblocks by side-shifting to neighboring protofilaments. Biophys. J. *108*, 2249–2257.

Schultz, P. (1988). Cryo-electron microscopy of vitrified specimens. Q. Rev. Biophys. *21*, 129–228.

Seeman, N.C. (1982). Nucleic acid junctions and lattices. J. Theor. Biol. *99*, 237–247.

Seeman, N.C. (2003). DNA in a material world. Nat. 2003 4216921 *421*, 427–431.

Seitz, A., and Surrey, T. (2006). Processive movement of single kinesins on crowded microtubules visualized using quantum dots. EMBO J. *25*, 267–277.

Shen, S., Naganuma, M., Tomari, Y., and Tadakuma, H. (2022). Revisiting the Glass Treatment for Single-Molecule Analysis of ncRNA Function. Methods Mol. Biol. *2509*, 209–231.

Shi, X., Jung, Y., Lin, L.J., Liu, C., Wu, C., Cann, I.K.O., and Ha, T. (2012). Quantitative fluorescence labeling of aldehyde-tagged proteins for single-molecule imaging. Nat. Methods *9*, 499–503.

Shima, T., Morikawa, M., Kaneshiro, J., Kambara, T., Kamimura, S., Yagi, T., Iwamoto, H., Uemura, S., Shigematsu, H., Shirouzu, M., et al. (2018). Kinesin-binding–triggered conformation switching of microtubules contributes to polarized transport. J. Cell Biol. *217*, jcb.201711178.

Shubeita, G.T., Tran, S.L., Xu, J., Vershinin, M., Cermelli, S., Cotton, S.L., Welte, M.A., and Gross, S.P. (2008). Consequences of Motor Copy Number on the Intracellular Transport of Kinesin-1-Driven Lipid

Droplets. Cell *135*, 1098–1107.

Sommese, R.F., Hariadi, R.F., Kim, K., Liu, M., Tyska, M.J., and Sivaramakrishnan, S. (2016). Patterning protein complexes on DNA nanostructures using a GFP nanobody. Protein Sci. *25*, 2089–2094.

Soppina, V., Norris, S.R., Dizaji, A.S., Kortus, M., Veatch, S., Peckham, M., and Verhey, K.J. (2014). Dimerization of mammalian kinesin-3 motors results in superprocessive motion. Proc. Natl. Acad. Sci. U. S. A. *111*, 5562–5567.

Stahl, E., Martin, T.G., Praetorius, F., and Dietz, H. (2014). Facile and scalable preparation of pure and dense DNA origami solutions. Angew. Chemie - Int. Ed. *53*, 12735–12740.

Strauss, M.T., Schueder, F., Haas, D., Nickels, P.C., and Jungmann, R. (2018). Quantifying absolute addressability in DNA origami with molecular resolution. Nat. Commun. 2018 91 *9*, 1–7.

Sun, X., Zhang, A., Baker, B., Sun, L., Howard, A., Buswell, J., Maurel, D., Masharina, A., Johnsson, K., Noren, C.J., et al. (2011). Development of SNAP-tag fluorogenic probes for wash-free fluorescence imaging. ChemBioChem *12*, 2217–2226.

Telley, I.A., Bieling, P., and Surrey, T. (2009). Obstacles on the Microtubule Reduce the Processivity of Kinesin-1 in a Minimal In Vitro System and in Cell Extract. Biophys. J. *96*, 3341–3353.

Thorn, K.S., Ubersax, J.A., and Vale, R.D. (2000). Engineering the processive run length of the kinesin motor. J. Cell Biol. *151*, 1093–1100.

Torisawa, T., Ichikawa, M., Furuta, A., Saito, K., Oiwa, K., Kojima, H., Toyoshima, Y.Y., and Furuta, K. (2014). Autoinhibition and cooperative activation mechanisms of cytoplasmic dynein. Nat. Cell Biol. *16*, 1118–1124.

Uçar, M.C., and Lipowsky, R. (2020). Collective Force Generation by Molecular Motors Is Determined by Strain-Induced Unbinding. Nano Lett. *20*, 669–676.

Vale, R.D. (2003). The molecular motor toolbox for intracellular transport. Cell *112*, 467–480.

Vu, H.T., Zhang, Z., Tehver, R., and Thirumalai, D. (2022). Plus and minus ends of microtubules respond asymmetrically to kinesin binding by a long-range directionally driven allosteric mechanism. Sci. Adv. *8*, 1–14.

Wagenbauer, K.F., Sigl, C., and Dietz, H. (2017). Gigadalton-scale shape-programmable DNA assemblies. Nature *552*, 78–83.

Webster, M.W., Takacs, M., Zhu, C., Vidmar, V., Eduljee, A., Abdelkareem, M., and Weixlbaumer, A. (2020). Structural basis of transcription-translation coupling and collision in bacteria. Science (80-.). *369*, 1355–1359.

Welte, M.A., Gross, S.P., Postner, M., Block, S.M., and Wieschaus, E.F. (1998). Developmental regulation of vesicle transport in Drosophila embryos: Forces and kinetics. Cell *92*, 547–557.

Wilson, M.Z., and Gitai, Z. (2013). Beyond the cytoskeleton: Mesoscale assemblies and their function in spatial organization. Curr. Opin. Microbiol. *16*, 177–183.

Wolberger, C. (2021). How structural biology transformed studies of transcription regulation. J. Biol. Chem. *296*, 100741.

Yan, H., Park, S.H., Finkelstein, G., Reif, J.H., and LaBean, T.H. (2003). DNA-templated self-assembly of protein arrays and highly conductive nanowires. Science (80-.). *301*, 1882–1884.

Zhang, H., Chen, D.-H., Mattoo, R.U.H., Bushnell, D.A., Wang, Y., Yuan, C., Wang, L., Wang, C., Davis, R.E., Nie, Y., et al. (2021). Mediator structure and conformation change. Mol. Cell *0*.

Zheng, S.Q., Palovcak, E., Armache, J.P., Verba, K.A., Cheng, Y., and Agard, D.A. (2017). MotionCor2: Anisotropic correction of beam-induced motion for improved cryo-electron microscopy. Nat. Methods *14*, 331–332.

Zhou, Z.P., Shimizu, Y., Tadakuma, H., Taguchi, H., Ito, K., and Ueda, T. (2011). Single molecule imaging of the trans-translation entry process via anchoring of the tagged ribosome. J. Biochem. *149*, 609–618.

Supplementary Tables

Supplementary Table 1
Supplementary Table 2
Supplementary Table 3
Supplementary Table 4
Supplementary Table 5
Supplementary Table 6
Supplementary Table 7
Supplementary Table 8

Supplementary Table 1 | Sequences of oligonucleotides

Seq Name	Sequence	Usage
KS_F2	CAAGGATCCATGGACAAAGATTGCGAAA	Forward primer complementary to the N-terminal of $SNAP_f$-tag used to introduce Lys-tags by PCR and check the constructs.
SNP_5K_R	TGCTCGAGCTTCTTCTTCTTACCCAGC CCAGGCTTGC	Reverse primer complementary to the C-terminal of $SNAP_f$-tag and containing a 5K sequence used to introduce 5K.
SNP_10K_R	TGCTCGAGCTTCTTCTTCTTCTTCTTC TTCTTCTTACCCAGCCCAGGCTTGC	Reverse primer complementary to the C-terminal of $SNAP_f$-tag and containing a 5K sequence used to introduce 10K.
KH_F2	GGATCCATGGCAGAAATCGGTACTGGC	Forward primer complementary to the N-terminal of HaloTag used to introduce 10K and check the constructs.
Ht_10K_R	TGCTCGAGCTTCTTCTTCTTCTTCTTC TTCTTCTTGCCGGAAATTTCGAGCGTCGAC	Reverse primer complementary to the C-terminal of HaloTag and containing a 10K sequence used to introduce 10K.
SNP_K_CR	GGTGGTGGTGCTCGAGCTTCTTC	Reverse primer for colony PCR used to check insertion of Lys-tags.
T7_R	GCTAGTTATTGCTCAGCGG	Reverse primer used to check insertion of Lys-tag by colony PCR and DNA sequences for all kinesin constructs.
T7_F	TAATACGACTCACTATAGGG	Forward primer used to check DNA sequences for all kinesin constructs.
KIF5A_SEQ549	GATTGATGAAGGGAAATCAAATCG	Forward primer used to check DNA sequences for all kinesin constructs.
KI493_C296A_F3	GGAAACGCCCGGACGACTATG	Forward primer used to check DNA sequences for all kinesin constructs.
KI493_C169A_R	GCGTTCAGTAGCACCCTTGACAAA	Reverse primer used to check DNA sequences for all kinesin constructs.
KI493_C296A R3	CATAGTCGTCCGGGCGTTTCC	Reverse primer used to check DNA sequences for all kinesin constructs.
KI351_R	CGTTTCCATGTTACACTGCTTGATGTTG	Reverse primer used to check DNA sequences for all kinesin constructs.
Ht_136R	GGGATAGGGCGGATGAACTC	Reverse primer used to check DNA sequences for all kinesin constructs.

Supplementary Table 2 | Sequences of kinesin constructs

Name	Sequence
Dimeric kinesin-SNAP$_f$ (0K)	ATGGCGGAGACCAACAACGAATCTAGCATCAAGGTGCTCTGCCGATTCCGGCCCCTGAACCAG GCTGAGATTCTGCGGGGAGACAAGTTCATCCCCATTTTCCAAGGGGACGACAGCGTCGTTATT GGGGGGAAGCCTTATGTTTTTGACCGTGTATTCCCCCCAAACACGACTCAAGAGCAAGTTTATC ATGCAGCTGCCATGCAGATTGTCAAAGATGTCCTTGCTGGCTACAATGGCACCATTTTTGCTTAT GGACAGACATCCTCAGGGAAAACACATACCATGGAGGGAAAGCTGCACGACCCTCAGCTGAT GGGAATCATTCCTCGAATTGCCCGAGACATCTTCAACCACATCTACTCCATGGATGAGAACCTT GAGTTCCACATCAAGGTTTCTTACTTTGAAATTTACCTGGACAAAATTCGTGACCTTCTGGATG TGACCAAGACAAATCTGTCCGTGCACGAGGACAAGAACCGGGTGCCATTTGTCAAGGGTGCT ACTGAACGCTTTGTGTCCAGCCCGGAGGAGATTCTGGATGTGATTGATGAAGGGAAATCAAAT CGTCATGTGGCTGTCACCAACATGAATGAACACAGCTCTCGGAGCCACAGCATCTTCCTCATC AACATCAAGCAGGAGAACATGGAAACGGAGCAGAAGCTCAGTGGGAAGCTGTATCTGGTGGA CCTGGCAGGGAGTGAGAAGGTCAGCAAGACTGGAGCAGAGGGAGCCGTGCTGGACGAGGCA AAGAATATCAACAAGTCACTGTCAGCTCTGGGCAATGTGATCTCCGCACTGGCTGAGGGCACT AAAAGCTATGTTCCATATCGTGACAGCAAAATGACAAGGATTCTCCAGGACTCTCTCGGGGGA AACGCCCGGACGACTATGTTCATCTGTTGCTCACCATCCAGTTATAATGATGCAGAGACCAAGT CCACCCTGATGTTTGGGCAGCGGGCAAAGACCATTAAGAACACTGCCTCAGTAAATTTGGAGT TGACTGCTGAGCAGTGGAAGAAGAAATATGAGAAGGAGAAGGAGAAGACAAAGGCCCAGAA GGAGACGATTGCGAAGCTGGAGGCTGAGCTGAGCCGGTGGCGCAATGGAGAGAATGTGCCTG AGACAGAGCGCCTGGCTGGGGAGGAGGCAGCCCTGGGAGCCGAGCTCGCTGAGGAGACCCC TGTGAATGACAACTCATCCATCGTGGTGCGCATCGCGCCCGAGGAGCGGCAGAAATACGAGGA GGAGATCCGCCGTCTCTATAAGCAGCTTGACGACAAGGATGATGAAATCAACCAACAAAGCCA ACTCATAGAGAAGCTCAAGCAGCAAATGCTGGACCAGGAAGAGCTGCTGGTGTCCACCCGAG GAGACAACGAGAAGGTCCAGCGGGAGCTGAGCCACCTGCAATCAGAGAACGATGCCGCTAA GGATGAGGTGAAGGAAGTGCTGCAGGTCCTGGAGGAGGGATCCATGGACAAAGATTGCGAAA TGAAGCGCACCACCCTGGATAGCCCTCTGGGCAAGCTGGAACTGTCTGGGTGCGAACAGGGC CTGCACCGTATCATCTTCCTGGGCAAAGGAACATCTGCCGCCGACGCCGTGGAAGTGCCTGCC CCAGCCGCCGTGCTGGGCGGACCAGAGCCACTGATGCAGGCCACCGCCTGGCTCAACGCCTA CTTTCACCAGCCTGAGGCCATCGAGGAGTTCCCTGTGCCAGCCCTGCACCACCCAGTGTTCCA GCAGGAGAGCTTTACCCGCCAGGTGCTGTGGAAACTGCTGAAAGTGGTGAAGTTCGGAGAGG TCATCAGCTACAGCCACCTGGCCGCCCTGGCCGGCAATCCCGCCGCCACCGCCGCCGTGAAAA CCGCCCTGAGCGGAAATCCCGTGCCCATTCTGATCCCCTGCCACCGGGTGGTGCAGGGCGACC TGGACGTGGGGGGCTACGAGGGCGGGCTCGCCGTGAAAGAGTGGCTGCTGGCCCACGAGGG CCACAGACTGGGCAAGCCTGGGCTGGGTCTCGAGCACCACCACCACCACCACTGA
Dimeric kinesin-SNAP$_f$-5K	ATGGCGGAGACCAACAACGAATCTAGCATCAAGGTGCTCTGCCGATTCCGGCCCCTGAACCAG GCTGAGATTCTGCGGGGAGACAAGTTCATCCCCATTTTCCAAGGGGACGACAGCGTCGTTATT GGGGGGAAGCCTTATGTTTTTGACCGTGTATTCCCCCCAAACACGACTCAAGAGCAAGTTTATC ATGCAGCTGCCATGCAGATTGTCAAAGATGTCCTTGCTGGCTACAATGGCACCATTTTTGCTTAT GGACAGACATCCTCAGGGAAAACACATACCATGGAGGGAAAGCTGCACGACCCTCAGCTGAT GGGAATCATTCCTCGAATTGCCCGAGACATCTTCAACCACATCTACTCCATGGATGAGAACCTT GAGTTCCACATCAAGGTTTCTTACTTTGAAATTTACCTGGACAAAATTCGTGACCTTCTGGATG TGACCAAGACAAATCTGTCCGTGCACGAGGACAAGAACCGGGTGCCATTTGTCAAGGGTGCT ACTGAACGCTTTGTGTCCAGCCCGGAGGAGATTCTGGATGTGATTGATGAAGGGAAATCAAAT CGTCATGTGGCTGTCACCAACATGAATGAACACAGCTCTCGGAGCCACAGCATCTTCCTCATC AACATCAAGCAGGAGAACATGGAAACGGAGCAGAAGCTCAGTGGGAAGCTGTATCTGGTGGA CCTGGCAGGGAGTGAGAAGGTCAGCAAGACTGGAGCAGAGGGAGCCGTGCTGGACGAGGCA AAGAATATCAACAAGTCACTGTCAGCTCTGGGCAATGTGATCTCCGCACTGGCTGAGGGCACT AAAAGCTATGTTCCATATCGTGACAGCAAAATGACAAGGATTCTCCAGGACTCTCTCGGGGGA AACGCCCGGACGACTATGTTCATCTGTTGCTCACCATCCAGTTATAATGATGCAGAGACCAAGT CCACCCTGATGTTTGGGCAGCGGGCAAAGACCATTAAGAACACTGCCTCAGTAAATTTGGAGT TGACTGCTGAGCAGTGGAAGAAGAAATATGAGAAGGAGAAGGAGAAGACAAAGGCCCAGAA GGAGACGATTGCGAAGCTGGAGGCTGAGCTGAGCCGGTGGCGCAATGGAGAGAATGTGCCTG

	AGACAGAGCGCCTGGCTGGGGAGGAGGCAGCCCTGGGAGCCGAGCTCGCTGAGGAGACCCC TGTGAATGACAACTCATCCATCGTGGTGCGCATCGCGCCCGAGGAGCGGCAGAAATACGAGGA GGAGATCCGCCGTCTCTATAAGCAGCTTGACGACAAGGATGATGAAATCAACCAACAAAGCCA ACTCATAGAGAAGCTCAAGCAGCAAATGCTGGACCAGGAAGAGCTGCTGGTGTCCACCCGAG GAGACAACGAGAAGGTCCAGCGGGAGCTGAGCCACCTGCAATCAGAGAACGATGCCGCTAA GGATGAGGTGAAGGAAGTGCTGCAGGTCCTGGAGGAGGGATCCATGGACAAAGATTGCGAAA TGAAGCGCACCACCCTGGATAGCCCTCTGGGCAAGCTGGAACTGTCTGGGTGCGAACAGGGC CTGCACCGTATCATCTTCCTGGGCAAAGGAACATCTGCCGCCGACGCCGTGGAAGTGCCTGCC CCAGCCGCCGTGCTGGGCGGACCAGAGCCACTGATGCAGGCCACCGCCTGGCTCAACGCCTA CTTTCACCAGCCTGAGGCCATCGAGGAGTTCCCTGTGCCAGCCCTGCACCACCCAGTGTTCCA GCAGGAGAGCTTTACCCGCCAGGTGCTGTGGAAACTGCTGAAAGTGGTGAAGTTCGGAGAGG TCATCAGCTACAGCCACCTGGCCGCCCTGGCCGGCAATCCCGCCGCCACCGCCGCCGTGAAAA CCGCCCTGAGCGGAAATCCCGTGCCCATTCTGATCCCCTGCCACCGGGTGGTGCAGGGCGACC TGGACGTGGGGGGCTACGAGGGCGGGCTCGCCGTGAAAGAGTGGCTGCTGGCCCACGAGGG CCACAGACTGGGCAAGCCTGGGCTGGGTAAGAAGAAGAAGAAGAAGAAGAAGAAGAAGCTCGAGCACCACCACCACC ACCACTGA
Dimeric kinesin-SNAP$_f$-10K	ATGGCGGAGACCAACAACGAATCTAGCATCAAGGTGCTCTGCCGATTCCGGCCCCTGAACCAG GCTGAGATTCTGCGGGGAGACAAGTTCATCCCCATTTTCCAAGGGGACGACAGCGTCGTTATT GGGGGGAAGCCTTATGTTTTTGACCGTGTATTCCCCCCAAACACGACTCAAGAGCAAGTTTATC ATGCAGCTGCCATGCAGATTGTCAAAGATGTCCTTGCTGGCTACAATGGCACCATTTTTGCTTAT GGACAGACATCCTCAGGGAAAACACATACCATGGAGGGAAAGCTGCACGACCCTCAGCTGAT GGGAATCATTCCTCGAATTGCCCGAGACATCTTCAACCACATCTACTCCATGGATGAGAACCTT GAGTTCCACATCAAGGTTTCTTACTTTGAAATTTACCTGGACAAAATTCGTGACCTTCTGGATG TGACCAAGACAAATCTGTCCGTGCACGAGGACAAGAACCGGGTGCCATTTGTCAAGGGTGCT ACTGAACGCTTTGTGTCCAGCCCGGAGGAGATTCTGGATGTGATTGATGAAGGGAAATCAAAT CGTCATGTGGCTGTCACCAACATGAATGAACACAGCTCTCGGAGCCACAGCATCTTCCTCATC AACATCAAGCAGGAGAACATGGAAACGGAGCAGAAGCTCAGTGGGAAGCTGTATCTGGTGGA CCTGGCAGGGAGTGAGAAGGTCAGCAAGACTGGAGCAGAGGGAGCCGTGCTGGACGAGGCA AAGAATATCAACAAGTCACTGTCAGCTCTGGGCAATGTGATCTCCGCACTGGCTGAGGGCACT AAAAGCTATGTTCCATATCGTGACAGCAAAATGACAAGGATTCTCCAGGACTCTCTCGGGGGA AACGCCCGGACGACTATGTTCATCTGTTGCTCACCATCCAGTTATAATGATGCAGAGACCAAGT CCACCCTGATGTTTGGGCAGCGGGCAAAGACCATTAAGAACACTGCCTCAGTAAATTTGGAGT TGACTGCTGAGCAGTGGAAGAAGAAATATGAGAAGGAGAAGGAGAAGACAAAGGCCCAGAA GGAGACGATTGCGAAGCTGGAGGCTGAGCTGAGCCGGTGGCGCAATGGAGAGAATGTGCCTG AGACAGAGCGCCTGGCTGGGGAGGAGGCAGCCCTGGGAGCCGAGCTCGCTGAGGAGACCCC TGTGAATGACAACTCATCCATCGTGGTGCGCATCGCGCCCGAGGAGCGGCAGAAATACGAGGA GGAGATCCGCCGTCTCTATAAGCAGCTTGACGACAAGGATGATGAAATCAACCAACAAAGCCA ACTCATAGAGAAGCTCAAGCAGCAAATGCTGGACCAGGAAGAGCTGCTGGTGTCCACCCGAG GAGACAACGAGAAGGTCCAGCGGGAGCTGAGCCACCTGCAATCAGAGAACGATGCCGCTAA GGATGAGGTGAAGGAAGTGCTGCAGGTCCTGGAGGAGGGATCCATGGACAAAGATTGCGAAA TGAAGCGCACCACCCTGGATAGCCCTCTGGGCAAGCTGGAACTGTCTGGGTGCGAACAGGGC CTGCACCGTATCATCTTCCTGGGCAAAGGAACATCTGCCGCCGACGCCGTGGAAGTGCCTGCC CCAGCCGCCGTGCTGGGCGGACCAGAGCCACTGATGCAGGCCACCGCCTGGCTCAACGCCTA CTTTCACCAGCCTGAGGCCATCGAGGAGTTCCCTGTGCCAGCCCTGCACCACCCAGTGTTCCA GCAGGAGAGCTTTACCCGCCAGGTGCTGTGGAAACTGCTGAAAGTGGTGAAGTTCGGAGAGG TCATCAGCTACAGCCACCTGGCCGCCCTGGCCGGCAATCCCGCCGCCACCGCCGCCGTGAAAA CCGCCCTGAGCGGAAATCCCGTGCCCATTCTGATCCCCTGCCACCGGGTGGTGCAGGGCGACC TGGACGTGGGGGGCTACGAGGGCGGGCTCGCCGTGAAAGAGTGGCTGCTGGCCCACGAGGG CCACAGACTGGGCAAGCCTGGGCTGGGTAAGAAGAAGAAGAAGAAGAAGAAGAAGAAGCTCG AGCACCACCACCACCACCACTGA
Monomeric kinesin-SNAP$_f$ (0K)	ATGGCGGAGACCAACAACGAATCTAGCATCAAGGTGCTCTGCCGATTCCGGCCCCTGAACCAG GCTGAGATTCTGCGGGGAGACAAGTTCATCCCCATTTTCCAAGGGGACGACAGCGTCGTTATT GGGGGGAAGCCTTATGTTTTTGACCGTGTATTCCCCCCAAACACGACTCAAGAGCAAGTTTATC ATGCAGCTGCCATGCAGATTGTCAAAGATGTCCTTGCTGGCTACAATGGCACCATTTTTGCTTAT

	GGACAGACATCCTCAGGGAAAACACATACCATGGAGGGAAAGCTGCACGACCCTCAGCTGAT GGGAATCATTCCTCGAATTGCCCGAGACATCTTCAACCACATCTACTCCATGGATGAGAACCTT GAGTTCCACATCAAGGTTTCTTACTTTGAAATTTACCTGGACAAAATTCGTGACCTTCTGGATG TGACCAAGACAAATCTGTCCGTGCACGAGGACAAGAACCGGGTGCCATTTGTCAAGGGTGCT ACTGAACGCTTTGTGTCCAGCCCGGAGGAGATTCTGGATGTGATTGATGAAGGGAAATCAAAT CGTCATGTGGCTGTCACCAACATGAATGAACACAGCTCTCGGAGCCACAGCATCTTCCTCATC AACATCAAGCAGGAGAACATGGAAACGGAGCAGAAGCTCAGTGGGAAGCTGTATCTGGTGGA CCTGGCAGGGAGTGAGAAGGTCAGCAAGACTGGAGCAGAGGGAGCCGTGCTGGACGAGGCA AAGAATATCAACAAGTCACTGTCAGCTCTGGGCAATGTGATCTCCGCACTGGCTGAGGGCACT AAAAGCTATGTTCCATATCGTGACAGCAAAATGACAAGGATTCTCCAGGACTCTCTCGGGGGA AACGCCCGGACGACTATGTTCATCTGTTGCTCACCATCCAGTTATAATGATGCAGAGACCAAGT CCACCCTGATGTTTGGGCAGCGGGCAAAGACCATTAAGAACACTGCCTCAGTAAATTTGGAGT TGACTGCTGAGCAGTGGAAGAAGAAATATGAGAAGGAGAAGGAGGGATCCATGGACAAAGAT TGCGAAATGAAGCGCACCACCCTGGATAGCCCTCTGGGCAAGCTGGAACTGTCTGGGTGCGA ACAGGGCCTGCACCGTATCATCTTCCTGGGCAAAGGAACATCTGCCGCCGACGCCGTGGAAGT GCCTGCCCCAGCCGCCGTGCTGGGCGGACCAGAGCCACTGATGCAGGCCACCGCCTGGCTCA ACGCCTACTTTCACCAGCCTGAGGCCATCGAGGAGTTCCCTGTGCCAGCCCTGCACCACCCAG TGTTCCAGCAGGAGAGCTTTACCCGCCAGGTGCTGTGGAAACTGCTGAAAGTGGTGAAGTTC GGAGAGGTCATCAGCTACAGCCACCTGGCCGCCCTGGCCGGCAATCCCGCCGCCACCGCCGC CGTGAAAACCGCCCTGAGCGGAAATCCCGTGCCCATTCTGATCCCCTGCCACCGGGTGGTGCA GGGCGACCTGGACGTGGGGGGCTACGAGGGCGGGCTCGCCGTGAAAGAGTGGCTGCTGGCC CACGAGGGCCACAGACTGGGCAAGCCTGGGCTGGGTCTCGAGCACCACCACCACCACCACTG A
Monomeric kinesin-SNAP$_f$-10K	ATGGCGGAGACCAACAACGAATCTAGCATCAAGGTGCTCTGCCGATTCCGGCCCCTGAACCAG GCTGAGATTCTGCGGGGAGACAAGTTCATCCCCATTTTCCAAGGGGACGACAGCGTCGTTATT GGGGGGAAGCCTTATGTTTTTGACCGTGTATTCCCCCCAAACACGACTCAAGAGCAAGTTTATC ATGCAGCTGCCATGCAGATTGTCAAAGATGTCCTTGCTGGCTACAATGGCACCATTTTTGCTTAT GGACAGACATCCTCAGGGAAAACACATACCATGGAGGGAAAGCTGCACGACCCTCAGCTGAT GGGAATCATTCCTCGAATTGCCCGAGACATCTTCAACCACATCTACTCCATGGATGAGAACCTT GAGTTCCACATCAAGGTTTCTTACTTTGAAATTTACCTGGACAAAATTCGTGACCTTCTGGATG TGACCAAGACAAATCTGTCCGTGCACGAGGACAAGAACCGGGTGCCATTTGTCAAGGGTGCT ACTGAACGCTTTGTGTCCAGCCCGGAGGAGATTCTGGATGTGATTGATGAAGGGAAATCAAAT CGTCATGTGGCTGTCACCAACATGAATGAACACAGCTCTCGGAGCCACAGCATCTTCCTCATC AACATCAAGCAGGAGAACATGGAAACGGAGCAGAAGCTCAGTGGGAAGCTGTATCTGGTGGA CCTGGCAGGGAGTGAGAAGGTCAGCAAGACTGGAGCAGAGGGAGCCGTGCTGGACGAGGCA AAGAATATCAACAAGTCACTGTCAGCTCTGGGCAATGTGATCTCCGCACTGGCTGAGGGCACT AAAAGCTATGTTCCATATCGTGACAGCAAAATGACAAGGATTCTCCAGGACTCTCTCGGGGGA AACGCCCGGACGACTATGTTCATCTGTTGCTCACCATCCAGTTATAATGATGCAGAGACCAAGT CCACCCTGATGTTTGGGCAGCGGGCAAAGACCATTAAGAACACTGCCTCAGTAAATTTGGAGT TGACTGCTGAGCAGTGGAAGAAGAAATATGAGAAGGAGAAGGAGGGATCCATGGACAAAGAT TGCGAAATGAAGCGCACCACCCTGGATAGCCCTCTGGGCAAGCTGGAACTGTCTGGGTGCGA ACAGGGCCTGCACCGTATCATCTTCCTGGGCAAAGGAACATCTGCCGCCGACGCCGTGGAAGT GCCTGCCCCAGCCGCCGTGCTGGGCGGACCAGAGCCACTGATGCAGGCCACCGCCTGGCTCA ACGCCTACTTTCACCAGCCTGAGGCCATCGAGGAGTTCCCTGTGCCAGCCCTGCACCACCCAG TGTTCCAGCAGGAGAGCTTTACCCGCCAGGTGCTGTGGAAACTGCTGAAAGTGGTGAAGTTC GGAGAGGTCATCAGCTACAGCCACCTGGCCGCCCTGGCCGGCAATCCCGCCGCCACCGCCGC CGTGAAAACCGCCCTGAGCGGAAATCCCGTGCCCATTCTGATCCCCTGCCACCGGGTGGTGCA GGGCGACCTGGACGTGGGGGGCTACGAGGGCGGGCTCGCCGTGAAAGAGTGGCTGCTGGCC CACGAGGGCCACAGACTGGGCAAGCCTGGGCTGGGTAAGAAGAAGAAGAAGAAGAAGAAGAA GAAGCTCGAGCACCACCACCACCACCACTGA
Dimeric kinesin-Halo (0K)	ATGGCGGAGACCAACAACGAATCTAGCATCAAGGTGCTCTGCCGATTCCGGCCCCTGAACCAG GCTGAGATTCTGCGGGGAGACAAGTTCATCCCCATTTTCCAAGGGGACGACAGCGTCGTTATT GGGGGGAAGCCTTATGTTTTTGACCGTGTATTCCCCCCAAACACGACTCAAGAGCAAGTTTATC ATGCAGCTGCCATGCAGATTGTCAAAGATGTCCTTGCTGGCTACAATGGCACCATTTTTGCTTAT

	GGACAGACATCCTCAGGGAAAACACATACCATGGAGGGAAAGCTGCACGACCCTCAGCTGAT GGGAATCATTCCTCGAATTGCCCGAGACATCTTCAACCACATCTACTCCATGGATGAGAACCTT GAGTTCCACATCAAGGTTTCTTACTTTGAAATTTACCTGGACAAAATTCGTGACCTTCTGGATG TGACCAAGACAAATCTGTCCGTGCACGAGGACAAGAACCGGGTGCCATTTGTCAAGGGTGCT ACTGAACGCTTTGTGTCCAGCCCGGAGGAGATTCTGGATGTGATTGATGAAGGGAAATCAAAT CGTCATGTGGCTGTCACCAACATGAATGAACACAGCTCTCGGAGCCACAGCATCTTCCTCATC AACATCAAGCAGGAGAACATGGAAACGGAGCAGAAGCTCAGTGGGAAGCTGTATCTGGTGGA CCTGGCAGGGAGTGAGAAGGTCAGCAAGACTGGAGCAGAGGGAGCCGTGCTGGACGAGGCA AAGAATATCAACAAGTCACTGTCAGCTCTGGGCAATGTGATCTCCGCACTGGCTGAGGGCACT AAAAGCTATGTTCCATATCGTGACAGCAAAATGACAAGGATTCTCCAGGACTCTCTCGGGGGA AACGCCCGGACGACTATGTTCATCTGTTGCTCACCATCCAGTTATAATGATGCAGAGACCAAGT CCACCCTGATGTTTGGGCAGCGGGCAAAGACCATTAAGAACACTGCCTCAGTAAATTTGGAGT TGACTGCTGAGCAGTGGAAGAAGAAATATGAGAAGGAGAAGGAGAAGACAAAGGCCCAGAA GGAGACGATTGCGAAGCTGGAGGCTGAGCTGAGCCGGTGGCGCAATGGAGAGAATGTGCCTG AGACAGAGCGCCTGGCTGGGGAGGAGGCAGCCCTGGGAGCCGAGCTCGCTGAGGAGACCCC TGTGAATGACAACTCATCCATCGTGGTGCGCATCGCGCCCGAGGAGCGGCAGAAATACGAGGA GGAGATCCGCCGTCTCTATAAGCAGCTTGACGACAAGGATGATGAAATCAACCAACAAAGCCA ACTCATAGAGAAGCTCAAGCAGCAAATGCTGGACCAGGAAGAGCTGCTGGTGTCCACCCGAG GAGACAACGAGAAGGTCCAGCGGGAGCTGAGCCACCTGCAATCAGAGAACGATGCCGCTAA GGATGAGGTGAAGGAAGTGCTGCAGGTCCTGGAGGAGGGATCCATGGCAGAAATCGGTACTG GCTTTCCATTCGACCCCCATTATGTGGAAGTCCTGGGCGAGCGCATGCACTACGTCGATGTTGG TCCGCGCGATGGCACCCCTGTGCTGTTCCTGCACGGTAACCCGACCTCCTCCTACGTGTGGCG CAACATCATCCCGCATGTTGCACCGACCCATCGCTGCATTGCTCCAGACCTGATCGGTATGGGC AAATCCGACAAACCAGACCTGGGTTATTTCTTCGACGACCACGTCCGCTTCATGGATGCCTTCA TCGAAGCCCTGGGTCTGGAAGAGGTCGTCCTGGTCATTCACGACTGGGGCTCCGCTCTGGGTT TCCACTGGGCCAAGCGCAATCCAGAGCGCGTCAAAGGTATTGCATTTATGGAGTTCATCCGCC CTATCCCGACCTGGGACGAATGGCCAGAATTTGCCCGCGAGACCTTCCAGGCCTTCCGCACCA CCGACGTCGGCCGCAAGCTGATCATCGATCAGAACGTTTTTATCGAGGGTACGCTGCCGATGG GTGTCGTCCGCCCGCTGACTGAAGTCGAGATGGACCATTACCGCGAGCCGTTCCTGAATCCTG TTGACCGCGAGCCACTGTGGCGCTTCCCAAACGAGCTGCCAATCGCCGGTGAGCCAGCGAAC ATCGTCGCGCTGGTCGAAGAATACATGGACTGGCTGCACCAGTCCCCTGTCCCGAAGCTGCTG TTCTGGGGCACCCCAGGCGTTCTGATCCCACCGGCCGAAGCCGCTCGCCTGGCCAAAAGCCT GCCTAACTGCAAGGCTGTGGACATCGGCCCGGGTCTGAATCTGCTGCAAGAAGACAACCCGG ACCTGATCGGCAGCGAGATCGCGCGCTGGCTGTCGACGCTCGAAATTTCCGGCCTCGAGCACC ACCACCACCACCACTGA
Dimeric kinesin-Halo-10K	ATGGCGGAGACCAACAACGAATCTAGCATCAAGGTGCTCTGCCGATTCCGGCCCCTGAACCAG GCTGAGATTCTGCGGGGAGACAAGTTCATCCCCATTTTCCAAGGGGACGACAGCGTCGTTATT GGGGGGAAGCCTTATGTTTTTGACCGTGTATTCCCCCCAAACACGACTCAAGAGCAAGTTTATC ATGCAGCTGCCATGCAGATTGTCAAAGATGTCCTTGCTGGCTACAATGGCACCATTTTTGCTTAT GGACAGACATCCTCAGGGAAAACACATACCATGGAGGGAAAGCTGCACGACCCTCAGCTGAT GGGAATCATTCCTCGAATTGCCCGAGACATCTTCAACCACATCTACTCCATGGATGAGAACCTT GAGTTCCACATCAAGGTTTCTTACTTTGAAATTTACCTGGACAAAATTCGTGACCTTCTGGATG TGACCAAGACAAATCTGTCCGTGCACGAGGACAAGAACCGGGTGCCATTTGTCAAGGGTGCT ACTGAACGCTTTGTGTCCAGCCCGGAGGAGATTCTGGATGTGATTGATGAAGGGAAATCAAAT CGTCATGTGGCTGTCACCAACATGAATGAACACAGCTCTCGGAGCCACAGCATCTTCCTCATC AACATCAAGCAGGAGAACATGGAAACGGAGCAGAAGCTCAGTGGGAAGCTGTATCTGGTGGA CCTGGCAGGGAGTGAGAAGGTCAGCAAGACTGGAGCAGAGGGAGCCGTGCTGGACGAGGCA AAGAATATCAACAAGTCACTGTCAGCTCTGGGCAATGTGATCTCCGCACTGGCTGAGGGCACT AAAAGCTATGTTCCATATCGTGACAGCAAAATGACAAGGATTCTCCAGGACTCTCTCGGGGGA AACGCCCGGACGACTATGTTCATCTGTTGCTCACCATCCAGTTATAATGATGCAGAGACCAAGT CCACCCTGATGTTTGGGCAGCGGGCAAAGACCATTAAGAACACTGCCTCAGTAAATTTGGAGT TGACTGCTGAGCAGTGGAAGAAGAAATATGAGAAGGAGAAGGAGAAGACAAAGGCCCAGAA GGAGACGATTGCGAAGCTGGAGGCTGAGCTGAGCCGGTGGCGCAATGGAGAGAATGTGCCTG AGACAGAGCGCCTGGCTGGGGAGGAGGCAGCCCTGGGAGCCGAGCTCGCTGAGGAGACCCC

TGTGAATGACAACTCATCCATCGTGGTGCGCATCGCGCCCGAGGAGCGGCAGAAATACGAGGA
GGAGATCCGCCGTCTCTATAAGCAGCTTGACGACAAGGATGATGAAATCAACCAACAAAGCCA
ACTCATAGAGAAGCTCAAGCAGCAAATGCTGGACCAGGAAGAGCTGCTGGTGTCCACCCGAG
GAGACAACGAGAAGGTCCAGCGGGAGCTGAGCCACCTGCAATCAGAGAACGATGCCGCTAA
GGATGAGGTGAAGGAAGTGCTGCAGGTCCTGGAGGAGGGATCCATGGCAGAAATCGGTACTG
GCTTTCCATTCGACCCCCATTATGTGGAAGTCCTGGGCGAGCGCATGCACTACGTCGATGTTGG
TCCGCGCGATGGCACCCCTGTGCTGTTCCTGCACGGTAACCCGACCTCCTCCTACGTGTGGCG
CAACATCATCCCGCATGTTGCACCGACCCATCGCTGCATTGCTCCAGACCTGATCGGTATGGGC
AAATCCGACAAACCAGACCTGGGTTATTTCTTCGACGACCACGTCCGCTTCATGGATGCCTTCA
TCGAAGCCCTGGGTCTGGAAGAGGTCGTCCTGGTCATTCACGACTGGGGCTCCGCTCTGGGTT
TCCACTGGGCCAAGCGCAATCCAGAGCGCGTCAAAGGTATTGCATTTATGGAGTTCATCCGCC
CTATCCCGACCTGGGACGAATGGCCAGAATTTGCCCGCGAGACCTTCCAGGCCTTCCGCACCA
CCGACGTCGGCCGCAAGCTGATCATCGATCAGAACGTTTTTATCGAGGGTACGCTGCCGATGG
GTGTCGTCCGCCCGCTGACTGAAGTCGAGATGGACCATTACCGCGAGCCGTTCCTGAATCCTG
TTGACCGCGAGCCACTGTGGCGCTTCCCAAACGAGCTGCCAATCGCCGGTGAGCCAGCGAAC
ATCGTCGCGCTGGTCGAAGAATACATGGACTGGCTGCACCAGTCCCCTGTCCCGAAGCTGCTG
TTCTGGGGCACCCCAGGCGTTCTGATCCCACCGGCCGAAGCCGCTCGCCTGGCCAAAAGCCT
GCCTAACTGCAAGGCTGTGGACATCGGCCCGGGTCTGAATCTGCTGCAAGAAGACAACCCGG
ACCTGATCGGCAGCGAGATCGCGCGCTGGCTGTCGACGCTCGAAATTTCCGGCAAGAAGAAGA
AGAAGAAGAAGAAGAAGAAGCTCGAGCACCACCACCACCACCACTGA

Gray, kinesin; underlined, self-ligating protein tag (SNAPf -tag or HaloTag); bold, Lys-tags (5K or 10K).

Supplementary Table 3 | Sequences of staples for 30HB rods

Seq Name	Sequence
Rod_001_5T2	ttttGGGCGATGGCCGTCTATCAtttt
Rod_002	CCAACGTTTTCCTGGATCCCCGGGTACCTTCGCGTCTGAGGCTTGCAtttt
Rod_003	AAAGAACGTGGACTCAAATCAAGTTTTTAATAACAGAACAATCAGTTGG
Rod_004	CACTATTCCGCTCAGCCTGCAGGTCGACGCCAGCTTTCATCA
Rod_005_5T1	ttttGTAATCATGGTCATAGCTGCAAAGGGCGCCACC
Rod_006	AGGAATCGGTTAAATCATCCTGTATCTAGAGTGTGAAATTGTTAT
Rod_007_5T2	ttttCATCAAAAATAAGAGCTCGAATTCttttt
Rod_008	CTGGCCTGCTCATTTTTTAACAGAGCATCAAATCA
Rod_009_5T2	ttttCAATAAAGCCTCCAATAGGAACGCttttt
Rod_010_5T1	AAAGCTACAAGGCAAAGAATTTTATAGTAAAAATCAGGTCTTTAtttt
Rod_011_5T2	ttttCCCTGACTAAGCAAAATTAAGttttt
Rod_012	TCGCATTAAATTTTTGTTGTACCAAAAACATACATCCAATAAATCATAC
Rod_013	ATTGCATAAACGAGAATGACCATAAATCCAGAAGCAAAGCGG
Rod_014_5T2	ttttCATTCAGTGAATAAGGACGTAACAAAGCTGCTttttt
Rod_015_5T1	CTTGCCCCGCAATAGAGGCGTGGCTTATCCGGTATTCttttt
Rod_016	TGACGAGAAACACCGGATATTTGCGGGAGATATAT
Rod_017	GTAGTAAGTTCAGACAAAAAGATTAAGAAGCATTATATGACCAAAT
Rod_018	CACCGGACCGCTTTCATTACC
Rod_019_5T2	ttttGGGAGTTAAAGGACCAGAGGCATGATACACCGGAATCAtttt
Rod_020	TCGTCACTTCATAAACGCAGTTAAGGCGATCATATGCGTTAT
Rod_021	CCTCAGCTCTTGACAAGAACCAGAACGAACCAGAACGACTTG
Rod_022	TTTAGGACAAATCAACAGTTGGCTGGTACTCAGGACTCAGAATCGGTCG
Rod_023	AATCAATATCTGGTATTACCGCGGAATAGCCACCAGCCCACGCATAACC
Rod_024_5T2	ttttCCTCAGAACCGAAAAACCCACTACGTGAACAGAAGAACTCAAtttt
Rod_025	CCGCCACCCTCAGAGGTGTATCCACCCTTTGAATA
Rod_026_5T2	ttttCCGCCTCCCTCATACCGCCACttttt
Rod_027_5T1	GGTTTAGGAGCCGCCGCGCAGAGGCGttttt
Rod_028	GGAAACCCCTTATTTCAAAATAGAACCGCACCGTA
Rod_029_5T1	ttttGAAGGTTATCTAAAATATCACAAAATCACCCTC
Rod_030_5T2	ttttCCAAAAGAACTGCCACCACCGGAAttttt
Rod_031	GCACTAACAACTAAGATTGCTCAGAGCCCCATCTT
Rod_032_5T2	ttttTAAGAACGCATAACGGAATACttttt
Rod_033_5T1	ttttAATTATTCATTTCAATTACAGAATAATAAGACTGAGGAAA
Rod_034	AAAGAAGATGATGATGATAAAATGTTAGCAAAGTT
Rod_035_5T1	ttttTAATTACTAGAAAAAGCCTTATAGAATTTAGCGAACCTCC
Rod_036	CCCAATACGGGAGGTTTTGAAAGCCGAACAAACGTGCGTTTG
Rod_037	CCTAATTTACGAGCTACCGACGGGTTATTAATTAAAGAACCTATCATTT
Rod_038	GCAAGCAAATCAGAGTTTAGTTTAAATACTGAGCACCAAGTT
Rod_039_5T2	ttttACTATCGGCCTTAAAGGAATTGAGttttt
Rod_040	ATATCCATCACTTGCCTGAGTCATCACC

Rod_041	ACCACCCTATAGCCCCAGCCACTTCTTTGATTAGTTGGGGTC
Rod_042	AAGAGTCGAGGTGCCGTAAAGAGCAATATTGCAAC
Rod_043	ACATTAACTTGCATCAATTCCACACAACTTGGAAC
Rod_044	TAGGCTGGAGGGTAAGTTGCGAGCCCAAAGTGTTGTTCCAGT
Rod_045	ACGCAACCCGAAAACGACCGGAAGCATAAAGAGGGTTG
Rod_046	CCGAGATTGTAAAGAGTCACGACGTTGTTCGGATTTACCGAT
Rod_047	ATACGAGCGGCCAGTGCCAAGATGTGAGTGACAACGACAGCA
Rod_048	CCGACAACGAGTAATTAATATTTTGTTACTGTAAT
Rod_049	GGTTTAACCCCCTCCGAAAGACTTCAAAATCAATTCGGGAGAAGCCTTT
Rod_050	AGCTTGACTCCGTGCAAATATTTAAATTGTAA
Rod_051	CTACAGAACAGACCATTTCAAGCTGAAAAGGTGGC
Rod_052	TCGGAACGCTGACCACTTTTGCTACTAATAGTAGTGGAAGCC
Rod_053	TATCGCGAATATTCATTGAATTTTCAAC
Rod_054	AAATGCTTTAAACAATTGGGCAGAGTAAAGCGAAAAACCATC
Rod_055	TTCATCATTGAGATAGCAGATGCCTTAA
Rod_056	AGGCGCATTTAATCAAGCCCTCTATTTTCCGTTTTTATTTTCGCCAACG
Rod_057	GCAACGGGGCATTTGGCAACATGACCTACTCAACAGTAGGGCAAGCAAG
Rod_058	CCCTCATTTTCAGGATATAAGTCAGAGCTAACGGA
Rod_059	AACCTCAAATATCAAGGAAAAAGGGTTGGATAGCA
Rod_060	TAGGAACTAAGTGCCCACCAGCTTTTACACATTTAACAATTTCATCTTC
Rod_061	ATCTAAAGCATCACACCTACAAGGCGGACCATGTA
Rod_062	AGAACCACGTCGAGACGCTCAAAATTAACCGTTGTCACTAAA
Rod_063	CTTATTAAGAAAATAAATACCCTTACCAGTATAAA
Rod_064	AACCCTCGAGCCGTCAATAGAGAAACAACGCCACCTAGCCCC
Rod_065	ATCGTAGATCAAGATTAGTTGTTTTAAGTAAAGGTTCGGTCA
Rod_066	CTTGCTGTTTGAGGATTTAGAACAGTACAGCCGCCTTTCATC
Rod_067	TATAAAACTTACCGATTGTGACGTCATATTTTAATTCGAGCTGGCGCGA
Rod_068	ATCAAGAAAACAAATGGTTTGACATACAAAAAGTA
Rod_069	GCACCCAGCTACAATAGCTATGAAACGCAGCGCGT
Rod_070	GAATCATTACCGCGACAAATTGACCGTGAACAAACTTCGCCTTAGATTA
Rod_071	AATTTAAATTAATTATCGGGATAATACA
Rod_072	TCGGAACCCTAAAGATCACGCTGGAAAT
Rod_073	GCCAGCACAGTACCTTTTGACAAAAGAGTCTGTCCGGAGCCC
Rod_074	GAATAGCCCGATTTAGAGCTTACCGAGTGCTCAAT
Rod_075	CGCAAGGGTATAAGGGAACAATTTTCCCCCTGGGGTGCCTAAATCAAAA
Rod_076	ACTTTGATTTCATGGCTTGCTCCAGTACAAAATCCCTTATAA
Rod_077	CCAGTAATGGTTAAGTTGCTAACTCACATTAAATCGGC
Rod_078	GTTCCGAATTGCGTGTGCTGCAAGGCGAGATAGGT
Rod_079	TGAGTGAGGGTAACGCCAGGGACGGCGGTGAATTT
Rod_080	TTCGAGGATTGACCAAAACAGGAAGATTATAAAAA
Rod_081	GTATCGGCACGTTGTTGATAATCAGAAAAGCC
Rod_082	TTTTAAGTAGCGTCGAACCAGACCGGAATTTAGCTAACCCTCATATATT
Rod_083	TTAAATGTGGTCAATAACCTGGCAAACTATGTTTAGACTGGAAACTGGC

Rod_084	AAGACTTAAGAGGATTTTTAGATATTTTCATTTGGTCAAAGC
Rod_085	CAATACTGCGGAATATTACCTACGGTGTGGCTTTGCTTAAACCCGTAAC
Rod_086	CAGATGATATGCGAATAGCAATTTTATC
Rod_087	CTGACCATCATTATATAAGAGCGCTAAC
Rod_088	ACTCGTATTAAATCTTGCGTAATTGGCCCGACAGATTCCATTAACCGAA
Rod_089	AGGACTAAGACTGTAAAGACAATTTTAGAGAATCGCCATATT
Rod_090	TTTATCAAGGAAGTATCAAGTTATTTTGCGAGAAAGCCAACATGTAATT
Rod_091	ACTGAGTTTTTGCTTTGACAGATGAATA
Rod_092	AGAGCCAGCAGCAACGTCTGAAGCGGGGTTCGTCA
Rod_093	AAACTACGAAGGATTCAGACGGATTTTCAGTACATAAATCAAAAGAACG
Rod_094	GCCTGCAACAGTGCATTGGCACTCAAGAAACGCCT
Rod_095	AGGCAGGTAGGATTAATGGATTAATCAGTGAGGCCGACGGGG
Rod_096	ATGAAAAGACTTTACAAACAAACGTCAGGAGGTTGTAGCGTC
Rod_097	AGTACCGCTGAATCTTACCAACAAGAAAATAAGTTTTGCCTT
Rod_098	TCACAATCCCAATAACCAGTCTAGTAAACCAACAGGTCAGGATCGCAAA
Rod_099	ATTACCTTTTTTAACAAATATCCACGGACAATGAA
Rod_100	CACTCATCGAGAACTTAATTGTTAATTTCATTTGATACAGTAAGTATTA
Rod_101	CGGGTATTAAACCATAACAACACTTTTTTGGAAACAGGTTTATTCGACA
Rod_102	CCAAGAAGAGCGTCTTTCCAGAGTTAAGCAATAGATCAGTAG
Rod_103	AAAGCCGGCGAACGGTTTTTATATTTACCACGCTG
Rod_104	TTGATATGAGACTCGATTCACGAATCCTGAGAAGTTGGCGAG
Rod_105	GATGGTGAAAGGAAGGGAAGATACGCCACAGTCAC
Rod_106	CAATGCCACCCCGGGTGTAGAGGGGGATTGCGCTCACTGCCCCCTGTTT
Rod_107	CAGCAGGCGAAAATGCTTTCCGCCAGCTGGCGAAATGGGCGC
Rod_108	GTAAAGAACTAGCACCGTGCACTATTACAGTCGGGAAACCTGTTTGCCC
Rod_109	AAAACGATTCACGTAAAGTTTGCGGTCCACGCTGG
Rod_110	AAAGGCCTCGATGAGGGACGACGATCGGAGCTGCATTAATGAGCAGCAA
Rod_111	GAGAGTTATCGGCCACTGTTGGGAAGGGCGACAGTATCGGCC
Rod_112	TCGTGCCTGCGGGCCTCTTCGTCTGCCA
Rod_113	CTCCAAAATCGTAATGTCAATCATATGTTGAGTAA
Rod_114	TGAAAATGTTTGAGACGGTAATCGTAAATTCAAAA
Rod_115	TATGGTTACCCACAAAAAATCAAGTTTTGTACCTTTAATTGCAGTTTGA
Rod_116	ACAAAAGAGCGCTAGAACTAAAGCGAGAGATAAGAGGTCATTATTCTGC
Rod_117	CTGGAGCAAACAAGAGAAGGAGACAGTCAAATACAGTTGATTCCCA
Rod_118	CGTAATGGCAGACGTGTGTAGCCATTAGATACATTTTAGAGA
Rod_119	CCAACCTGTTACTTGGGTGAGGAACGAGTAGATTTTCCTTTT
Rod_120	TTTGCGGATGGCTTAGAGCTTCCATATACACCATCAATATGA
Rod_121	GCCAGAGGGGGTAAAGGACGTATAAGGGAAACGGGTTTAATTGTAGCAT
Rod_122	GGCTTTTGCAAAAGTACGTTAACGAGGCCCACTACAAAAAGGTCATAGT
Rod_123	ATAAAAACCAAAATCGGAACAGCTCCAT
Rod_124	GATTGAGAACAAAGTACAGGTGACGACG
Rod_125	GTCAATCTGGGAAGAGAATTGAGCCTAA
Rod_126	AGCCGGAATAAAACATATCAGAATAAAC

Rod_127	AAAAGAAGAAATCCGCGACCTACATTATTCAGAGGTCCCAAT
Rod_128	AGGAGCCTAAAATAACCGTAAAAATTCACCAATCGAGGCATTTTCGAGC
Rod_129	CTCCAAAGAAGGCAAATGAAAGCCAAAGTATGTAAAAGAGAATATAAAG
Rod_130	TAATTTTAAGAGGCAGCAAGGTTCAACCTTAGGTTAAAAGGTAAAGTAA
Rod_131	AAAAATACCGAACGACCCTTCTGCCCCCTTTCCAGCGAATAA
Rod_132	TCCACAGAGAGGCTTCACAAACAGAAATGAGTGAATAACCTTTGCAAAT
Rod_133	GAGGCGGTCAGTATACGACCAAGTATTAACAGCCC
Rod_134	TAGCGTATTCTGAATTAAAGCCAAAATTTAAATCGTCGCTATATAACTA
Rod_135	AGCAGAAGATAAAAATTCTGGCCTATTAACGATCT
Rod_136	TGTCGTCTGCCTATCAGTCTCAAGGGTTTTTTCCCTTAGAATCTCCGGC
Rod_137	ATCCTCAACATGAAGTAATAATTAGACAGGAACGGAAGCGAA
Rod_138	GAAAGCGTTCGGAACCAACAGAGGAGGCCGATTAAGGGCGCT
Rod_139	TAACACCCGAACGTTATTAATCGTAAAACAAATAATAGCAGC
Rod_140	CGGCTGTTTTGCCAGTTACAAAGAGATATACCAGCCCATCGA
Rod_141	CAGAGGTGTTTGAGTAACATTACCATATCAGAATGCGTCACC
Rod_142	ATGTAGAAGCCATATTATTTAGTAATTGGGCGACACCGGAAA
Rod_143	AACCACCTGCGGAACAAAGAAATAATGGTGAATTTTACCATT
Rod_144	CTTTCCTTATCATTTAGGCAGCAAGACATATATGTAAAGAAACTTTGCC
Rod_145	AACCAATCAATAATCAGTAATATGCTGAGCTTCTGATTTGCATTTAAAA
Rod_146	ATCCCATCCAAATAAGAAACGCACCCTGGGAGGGAGCACCAT
Rod_147	AGGAGCGGGCGCTAAGGGATTAAGGGAC
Rod_148	GGCAAGTGTAGCGGGCTAAACAGATAGA
Rod_149	ACCGTTCCAGTTAATGACCTGGAATCAGAGCGGGATCACGCT
Rod_150	CCGCCTGGCCCTGAGCGCGTAACCACCACTCGTTAAAAGCGT
Rod_151	CCCTTCAGGCGGTTATTCGCCATTCAGGGATCGCA
Rod_152	TTTGTATGACCCCCGAATAGAGTATGGGCTGATTG
Rod_153	CCGTTCTGCTATCACAGCTTTAAGCGCCTGCGTATTGGGCGCGCAACAG
Rod_154	GAGACGGCAGGGTGCCGGAAACCAGGCACCGGCAC
Rod_155_5T2	ttttTTCACCAGTGGGCGCGTAttttt
Rod_156	TCAGGAACTGCGCAAACGCGCGGGGAGA
Rod_157	AAGGAACCTCCAGCGGTCATTGCCTGAGAGT
Rod_158_5T1	ttttAACAGTTTCAGCCGCTTCTAGAGATCTACAAAGAGCTGAT
Rod_159	TATTGACGAGAATTGTTGAGATATCATAGAATATAATGCTGTACGGTGT
Rod_160_5T1	ttttAAACAAAGTACAAAATTAATATGCAACTAAAGT
Rod_161	CATCTTTCATCGCCTATTCAACTGGAAGTTTCATTAATTGCT
Rod_162	AGCTCAAAGTAAGAGCAACACTTTAGGA
Rod_163_5T2	ttttATAGTGAATTTAAAAGGTGACAGGGAATTCAACGAGGCATCATGTTTTAttttt
Rod_164	ACCCTCGTTTACCAAGAAAGATTGTGTCTACACTAGGAATTGACGTTAG
Rod_165_5T2	ttttCGCCAAAAGGAATTACTAATGCAGATACATAAttttt
Rod_166	TGATAAATTCATCAAACTGAAATTTTTTACAAGAA
Rod_167	ACGGAGAATACCACAGCGCATATGAAAA
Rod_168_5T2	ttttATGGCAATTCATATACAGGCCATTTGATACCAAGCGCGttttt
Rod_169	AACTAAAAAACACTACCAGTAAGGTAAAACTACCTCAGACGACGACAAT

Rod_170_5T1	GGAGTGAAGCGATTGGAATTAATTCATTTCAAAATATGTTCAGCTAATGCAGAAttttt
Rod_171	TAAATGAGTATAAACAGTAAGGATTATAAACATAGCGATAGCCTGAGAG
Rod_172	TAGCCCTAAAACATAAGAATAAGTGCCCATTTTCT
Rod_173_5T1	ATTTTGCGTGCCTTTTTGATGCAATATAAAGACGCTGAGAAGAGTCAttttt
Rod_174_5T2	**tttttTTAGTCTTTAATGCGCTATTTTTGGGGTCATAAACAACTTTCttttt**
Rod_175_5T1	tttttATAAGTTTTAACGAATGGCATGGTTGCTTTGACCGCTACA
Rod_176	CATGGCTGAGTAACCGTGGCATATAACGTGCTTTCCACCCGCCGCGCTT
Rod_177_5T2	ttttCACCGACTTGAGAGTGTACTGGTAttttt
Rod_178	CGCCATTGAAGGAGCGGAATTTTGTTTGCGTCATACAAAATC
Rod_179	GTCCTGAGTTTAACGTCAAAATAGACGGGGAAATTGAGCCAG
Rod_180_5T2	ttttAATAACATAAAAAATTATCACCGTttttt
Rod_181_5T2	ttttCGCGCCTGTTTATAGCAGCCTTTACAGAGAGttttt
Rod_182	AAATAATTTCTGTCTTTTAACCCTTGAACTTCTGAACCACCA
Rod_183	TCAACAATAGATAAAAACAACCATAGGTTTAGATTATCCTGAATCATCA
Rod_184_5T1	AATGCGCGAGCACGCAGACAAGAACTGATATTCCTGATTATCAGATGttttt

Underlined (117), ligand (BG or CH)-conjugated; bold (174), fluorescence dye-conjugated. This information was kindly provided by Prof. Hisashi Tadakuma.

Supplementary Table 4 | Sequences of modified staples for 30HB rods

Seq Name	Sequence
Rod_117_5NC12	[BGC12]ttttttCTGGAGCAAACAAGAGAAGGAGACAGTCAAATACAGTTGATTCCCA
Rod_174_Cy5	[Cy5]ttttttTTAGTCTTTAATGCGCTATTTTTGGGGTCATAAACAACTTTC

This information was kindly provided by Prof. Hisashi Tadakuma.

Supplementary Table 5 | Sequences of staples for 28HB rods

Seq Name	Sequence
Rod3_001_3T	CTGTCGTGCCAGCTGCGGTCGCTGCGCCCACGTCGCCTGAGCAGCAAAtttt
Rod3_002	TGCTGAACGCCACGCTGATTCACAATGACATTGGGCGCGGGAAAC
Rod3_003	AAACCAAATGTCGAAAGAAACAAAAGGGAGTTAAAGGCCGTTCCAGTC
Rod3_004_4T	ACGTCAATTTGCGTAACAACCATAGGCTTGCGTACAACGGAGATTTGTAtttt
Rod3_005_4Tv2	ttttAAAAGAAGAAAGCGAACCAGACCGGATAAATTATATGATACTGTAGCCATAAGAAA
Rod3_006	CGAGCTTCTTTTGCCAGAGGGGGCCAAGCGCTCCGCGACGCGCCGAC
Rod3_007_4Tv2	ttttTCATTTCAATTATCTGAGAGCAGGTCAGACCATCAAATGCCGACCAATAGGAACGCCA
Rod3_008_4T	ttttCTCCGGCTTAGGTTGCAAGTACCTTTCATCGAATCCAAAGCTTTCA
Rod3_009	TCAACATTTTTTTTAGAGAGGGTAGCTATTTTTTTAATTGAGTACCTGACGATAA
Rod3_010	TCCTTTTGAAAGGGTGTCTACAAATTAAATTTTTGTTAAATCAGCTCAAAATGTGA
Rod3_011	CGGAGACAATTACCGCTATCAAAAAACTATATGTTACAAAATCGCGC
Rod3_012_4T	ttttAACTCCAAACTACCTTGTTTTTATGCACTCATAAAATAGCAGCCTTTA
Rod3_013	CAGAGAGTTTATCCCTAGGAATCGTCAAATCGATTAGA
Rod3_014_4Tv2	CTACGTGAACCATCACCTACATTCATTGGCAGAGAGCCATAAATTGATAGCGAGAGGCTtttt
Rod3_015_4T2v2	ttttAGAGGCGGAGGGCGAAATTATTTATTGACGCTATCTAAAGCATCACCTAGAGGCGAattattttt
Rod3_016	CAGGGTGGTTTTTCTCACTATTACGACCAGTCAGGAAAA
Rod3_017	AAAGAAGAGCAACAGTCTCAAATAACGCTCATGGAAATACCCAAATCGGACTCCA
Rod3_018	CAGTCACAAAGAACGTAAGTTTTTTGGGGTCGAGGTGCCGCATTGCAA
Rod3_019	AGAACGGGTATTAAACGGTTATATTCATAGGCCTGAGCA
Rod3_020	TTGAGAGAAGAAAGGCGCGAGTAATAAACAGCCATATTAAATAACAT
Rod3_021	GCGCTCACTGCCCGCTCTTTTGCCGATAGTTCTGCTCCAACCGCCT
Rod3_022	ATATCTGGGGCGGTCAGGACATTCTTAAACAGGTGAGACGATTGCGTT
Rod3_023	GGGATCGTACCCCCAGCGATTATATAATAGTAACCAGACTTAATTGC
Rod3_024	ATCATAACAGCCGGAACATCTTTGCACCCTCA
Rod3_025_5L	GCAGCGAATCACATTAGGCAACAGCTGATTGCTTGAGTGAGAGATAG
Rod3_026	AATCAGATAAGATTCAATAAGAGGCCCGAAAGAGACTGGATAGCGTCCAAAACACT
Rod3_027	AATAAAAGGTATTAACTGTTACTTCCTCGTTTAAATGTTTACTTCAAATATCGCG
Rod3_028	ACAACCCGTCGGATTCAATTCGCAGGCTATCA
Rod3_029_5L	GGTCATTGAGAGGAAGTCATTTTTGCGGATGG
Rod3_030	GAGTGTAAACGTTAATATTTTGTTAA
Rod3_031	TCCGTGGGTGTAGGTAATAGAAGGATTAAGACGCAAGACATAACGGATTCGCCTGA
Rod3_032	GCAACACTAAAATTAAAGAGGTGATCAGTTGGCAATATTACCGCCAGC
Rod3_033	CGAGGCGCTGAATTTCTGGCCAACTTGTTCCATAAATCGGAACCCTAA
Rod3_034	TAAAGCACGTTTGGAACAAGAGTCTTTCACCACTTGATAC
Rod3_035	TGATGAAAAATACCAAGTAAATGCTGATGCAATTCCTTATAGCAAGCAGTTACAAA
Rod3_036	CAATAATCGGCTGTCTATCCAATCGCTGAGAAAAGAAAAC
Rod3_037	AGTGAATTGCCCAATCATTCCAAAAAACAGGGAAGCGCATTAGACGATTTGCCA
Rod3_038	TCAAACCCTCAATCATTGCTTTGCAAACATCGAGTCAAT
Rod3_039	AACAAACGTCTTTCCAGAGCCTAGGAGAATT
Rod3_040_3L	AATGAGTGAGCTAACAGACAGCATCGGA

Rod3_041	AGGAATTGCGAACCACCTGACCTGGGTTTATCGCCTGGCCGGGTGCCT
Rod3_042	AGGGAACCCGAAAGAGAGGGTAGCAACGGCTAAAGCCTG
Rod3_043	ACGGCAAAAGAATACACTAATACTGCTAGTAAGA
Rod3_044	AGAACGCGTTAAATGCCTTAATTGAAGCGGATTCATAAATATTCATTGACCTAAAA
Rod3_045_3L	GGAATCGTGCATCAAAAAGATTACCTGAGAGTCTG
Rod3_046	GCGGATTGACCGTAATATTTAAATCAAACAAGAGAATCGAAGAAGCA
Rod3_047	AAATTTTTAATCGTAAAACAGGAAGATTGTATAAGCAAATGGGATAG
Rod3_048	ATAGCGACTTAGAGAATGCCTGAGTAATG
Rod3_049	CATATATTAGGCGTTTAGAATCCAATATATTGTAACAGTACCTTTTA
Rod3_050	CTGAATATACGCCAAATTACCTTTACCGAAAGGAAGGAAACTATCGGCCTTGC
Rod3_051	AGGGAGCTGGTAATAAACCCTTCAGCAGAACAATCATAACGAGGCA
Rod3_052	CATCCTAATTTACGACTTTTTCATTGAAAACTCATTTGAAAGGAATT
Rod3_053	GAACTGACATTGTATCAAAGCGTATCAAAAGATAGAGCTTGACGGGGA
Rod3_054	TTTCGAGGAGACGGTGATAAAACTTACATTAGAAACAA
Rod3_055	CCCCGATTATAGCCCGAGATAGGGCCTTCACCAGCTTGC
Rod3_056	CTGAGAGAGTTGCAGCTTATAAAAGAATACGAAGAACTC
Rod3_057	TCCAGAACAAATCAACAGTTGAACATCGGGTAACAATT
Rod3_058	TAGCTTAGCTTATCCGAAACCAATAACTGAACACCCTGAACAAAGTCCCAACGCT
Rod3_059	AAGAACGCGAGAAAAGCATGTAGGTATTCTAAACGAGCG
Rod3_060	AGAACCCTGTCACGTTTTTATCCTGAATCTTAAGAGGGTA
Rod3_061	CGGAAGCATAAAGTGTACAGAGGCAGCCTTTACAACTTTGATTAAAAA
Rod3_062	TAGGAGCAGCCCTAAAACAATATTAAAAGGCTCCACGCTGATACGAGC
Rod3_063	ACATTCAACAGATGAACGTAATGCCTAAAGACTTTTTCATCACACAAC
Rod3_064	TTTGAGGACACTACGAAGGCACCAAATCCCCCGATACATAAATGCTGT
Rod3_065	CTTGCGGGAAGGATAAATGTTTTAGTCTTTACTTTAAACAGTTCAGAATAAAATA
Rod3_066	GGTGTAGATGGGCGCAGCCCCAAAAACTAGCATGTCAATAAAATCAG
Rod3_067	CTAATGCATCAAATGCCCTGACTATTATAGTCTGAACGGT
Rod3_068	AACGGCGGTTGATAATCAGAAAATCGTAACCTCAACGC
Rod3_069	TTATCTAAAATATCTTGTCAGATGGAAACAGTTTAATTAAAGCTCAAC
Rod3_070	AATATGCAGGAATACCCAATATAAACTGATACTAACAACAATAACATCACTTGC
Rod3_071	AAGCCGGCCTGAGTAGTGGCACAGACATCGCCAAAGAGGA
Rod3_072	CGGTGTACTCCAAAATTTGAATGTGGTTCCCGAGAAAGGAAGGGA
Rod3_073	GAACGTGGGAAATCGGCAAAATCCCAAGCGGTCCAAAAGG
Rod3_074	GTTTGCCCCAGCAGGCGAAAACACTTTCACGTTTCGTGTGTTCAGCA
Rod3_075	TTTTAATGAATATACATTAGTTAATTTCATCTAAGAAAAACCTCCCGAGCTACAAT
Rod3_076	TAGATAAGTCCTGAACTCTGACCTCGTCGCTAACATAAAT
Rod3_077	TTTTCCCTTTAGCGAATAATATCCATTGAGCGCTAATATCAGAGAGATTGCACCCA
Rod3_078	AGGTTTTGCTGTAAATAAATTTAGATTTTCAGGTTTAAC
Rod3_079	CCTTTATTGTGCATCTGATTAGTTGCTATTTAACCCACA
Rod3_080	ATCCGCTCACAATTCGAGGAAGTTGAAAATCAGACCAGAATGCGCG
Rod3_081	AGAAAGCGTACTTCTTGTCTTGATGATACAGGAATAATTTCCTCAGAAAATTGTT
Rod3_082	AATCGTTACCTGTGTGACCGCCACCCTCAGAGGTTTAGTAGGTAATAA
Rod3_083	CATCAGTTATGGTCTCGTCGCTGGCAGCCTCCTCATAAAC

Rod3_084	AAAGATTGCTGGCTGATCCCTTACACTGCATTAAACGGGAACGAGA
Rod3_085	TACGGTGTGGGAGAAGCCCATAACCTCACCGGAAACAATCCAAACGCG
Rod3_086	ACTTTTGCCTGGAAGTGTCCGTTTTTTCACCATAAATCACATATGTA
Rod3_087	CCAATAATATTCATATGGTTTCAAGCCAGTTTGAGGGGAGCCACGGG
Rod3_088	GTTGATTCCCAAAAACGTACAGCGTGCCAAGCTTTCAGAGGTGGAGCC
Rod3_089	CGACGACACCTGTAATGACAAAAGGCATTTTCATAAATAAGCACGTAAAACAGAAA
Rod3_090	TTCATTCCACAGGTAGCCATCTTTGTAAGCGTATAATACATTAACCGTTGTAGCAA
Rod3_091	GAGATTTAACTAAAGCTTGCTTAAGCCTTAATCAACAAAGAATTGAGTTAAGC
Rod3_092	TCAATAGCATACATGGCTTTTTGCGCATAG
Rod3_093	ACCTTCATTTGCGAATAGTGTACTCCGCCACCGGGCGCTAGGGCGCTG
Rod3_094	AAAGGAGCCTCAGAACCGCTCCTGTTTGATGGGCTATTA
Rod3_095	TGTGAGTGTTGCGTAATGGTTTGAAATACCGGCCTGTTTAATACCAGCGCCAAA
Rod3_096	TGATTAGTTAATAGATTAGAGCCGTAAAGAAAAATTTATTAGCGTTTG
Rod3_097	GCTAATGCAGAACGCACCGTGTGGGTCATAGCCCCCAAC
Rod3_098	ATTATGACGTATCGGCTCACAATCAATAGAAAAAGAGCAA
Rod3_099	ATGGTCATAGCTGTTTACGGCATCTAAAGGAACAAGAGTACCGTTCCA
Rod3_100	TATTAGACGCAGTCTCGGGGTCAGAATAGAAACTCATTTTTCGTAATC
Rod3_101	CGGAACCACGAACTAAAGAACCATGGGTAGGTTACCTGCAGCCAGCTCGAAT
Rod3_102	AGATGCCGAAGGTTTCTTTGCTCGGGCCAGAGACATTATT
Rod3_103	AAACGATGCATAACGGAACGTGCGGCTGGTAGGATATTCGAGTGAGTGCCTTG
Rod3_104	ACGGAACACACATCCTCTGATTGCCGTTCCGGGGCGAAAC
Rod3_105	CCATGTTTACCAGTCGTAAAGTTGCGAACGTTAATAAA
Rod3_106	TTATTTTGCTCAGGAAGATCGCACACGGCCAG
Rod3_107	TGTGAGAGCCCAGTCACGACGTTGTAAAACG
Rod3_108	TCCAGCCAGCTAAATCGGGAAGGTTTTAGCGGGAATCATAGGGTTAGAACCTAC
Rod3_109	ATATAACATTTCATCGGGCGACATCATGTTCAGAAACAATGAAATAGC
Rod3_110	AATAGCTAAATAAGTTTGAGGGAGGTTGTACCAATTCT
Rod3_111	GCAAGTGTCTGTCCATGTTTTAACTGAATTTAATCTTGAC
Rod3_112	AGCGGTCACACCGTACTCAGGAGCCACCACCGGAACAAC
Rod3_113	CAGGGATAGCAAGCCCCCCGGAATAGTAACAGGTGAGGCC
Rod3_114	AGGTGTATCGCTGCGCGTAACCACCACACCCTATAATCA
Rod3_115	TCATAATCAATTATTTGGCGTTAAATAAGAATATAAACAATCAACCGA
Rod3_116	AGAGCCACTGGAAAGCTTTACAAAACCGAGTAAAAGAGT
Rod3_117	CACGCAAATTTGAGGATTTAGAAGCATATCAAAAAATCACTAGCGCGT
Rod3_118	TGTCCAGACGACGACAAAACACCTCAGACTG
Rod3_119	AGCATAAAGCTTTCCGCGCAAAGACACCACGGTCTTACC
Rod3_120	ATCCCCGGGTACCGAGCGGTGCCG
Rod3_121	TATTAAATATAAATCCTAAACAGTAAACAACTACCCATGTAGTTGAGG
Rod3_122	GTGCCCCGTCACTGTTGCCCTGCCGGACTTGAATCTACG
Rod3_123_3L	GACGTTGGTAACAAAGTGAGCCGGCTGCATCA
Rod3_124	GACGATCCCTCCTCACACCGTAACACTGAGTTAAGTGCCGCCTGCCTACGCCAGAA
Rod3_125	TAGAACGTCTTTAGTGATGAAGGCCGGAATT
Rod3_126_3L	AAAAGAAAGCACCGCTTCTGGTGAGGGTTTTATAGACTT

Rod3_127	TCTCCGTGAAGCCGCACAGGCGGCCAGCGTGGTGCTGGTCTTGCGGTACTGCTCAT
Rod3_128	CTCAAGGCGATTAAGTTGGGTAACGCCCCGGAAAC
Rod3_129	CAATTCGACAACTCGACTTCTGACCGCCTCCCAGAATCATAGTTTGAAGCCTCAG
Rod3_130	CAAAATTATAAAGGTGCCGTAATCTATCATATTGATTGTTTGGATTAT
Rod3_131	AGTAGATTAGTTTGCCAAATATTGAGTAATTCGAAGCCCTTTTTAAGA
Rod3_132	AAAGTAAGCAACATATTTATTCATAGCAATAACCATTAGA
Rod3_133	TACATTTCCCAGTCAGCGCCACCCACAAACAACCTTTGCCTCCTGAGAAGTGTTTT
Rod3_134	TGCCCGTATCATTAAAATCAACGGAAGAAA
Rod3_135	TTTCAGCGATTACCCAAGCCAGAA
Rod3_136	GCCGCGCTGTTGATATAAGTATAGAATAGGATTCAACAG
Rod3_137	ATTTTGCTTAATGCCCTCGAGAGGTAATGCGCCGCTACAG
Rod3_138	CACCGGAAATAATGGAAATTACTAGAAAAAGCAAGGTAAACGGAAA
Rod3_139	TATAAAGTACCGACAACTGTTTAGAGTAGCGACTCAGAGC
Rod3_140	AGAATTAGCAGGCAAAACATACATAAAGGTGGCAGATAGC
Rod3_141_3L	CTTCGCGTCCGTGAGCAGCGCAGTGTCAC
Rod3_142	TAAAAGTTGTCAGACGCCTATTAAGTAAATAGTACAAAGCCTGTT
Rod3_143	TCAGAGCCGATTTTAATGCCCTGACGCACTCAGCGCCTGTGCACTCTGGCACGCGT
Rod3_144	TGCATCCGCCGGGCGCGGTGGTCAGCTCATTATA
Rod3_145	CGACATAACAAGAATGCCAACGGGGCGCTTTCGAGAAAC
Rod3_146_3L	GAACTGGCAGCAACCGAAAAATCCCGTAAAAAGTGAAGGGATAG
Rod3_147	TCACGGAAAAAGAGACGTGTACATGCTATATTCCTTATGC
Rod3_148	AGAAAATGCGCCATTCGCCATTCGTGCTGC
Rod3_149	AGTAGCATAGCGGATCTACGCCAGCTGGCGAAAGGGGGAT
Rod3_150	AGGCTGCGAATAAATCCCATTTGGAACGTCACATAAAGCCATCAGATGATGGCAA
Rod3_151	CGAACGTTATTAATTTTTCATCAAGCCACCCACCATCGATCAATAACAAGGCAA
Rod3_152	GCAAATGGTAGCAGCAAATTATCATAAGAGAACGAACAAAGTTACCAG
Rod3_153	AAGGAAAGCAAACGTGACTTGAGATACAGGCCTGTTTA
Rod3_154	GGCGCGTAAACGGTATTTCGGAAATTGGCCTTAAGGCT
Rod3_155	TGTATGGGTCAGTGAATGATATTC
Rod3_156	CTATGGTCAGTACCAGGCGGATTCGTCACCGAATTTTC
Rod3_157	CAGACGTTTTCTGAAAGTTTTGCTTGCTTTGACGAGCACG
Rod3_158	CTACAACGCCTGTAGTTAGCGGGCATGAAAGCCGATTAA
Rod3_159	TCAGAACCTATAATCCGCGTTATACAAATTCGCCAGTAACCGTCACC
Rod3_160	ACCACCCTTGAGGCAGTGAGTAACAGGGATTTTAGACAGG
Rod3_161	GCAGAGGCATTTTCGATTACCAGTCAATGAA
Rod3_162	TAACATCCCAACTGTATTACGCAGTATGTTACCGAGGAA
Rod3_163_4T	ttatCCGGGGGTTTCTGCCATGGTGCTCGTCTTTCACCAGAACAGGAGGT
Rod3_164_4T	ACCACCACTCAACTTTAATTGGGCTCCAGCATAATGCGGCGGGCCGtttt
Rod3_165_3T2T	tttTGATTAAAAATCACCCTAATAGTGCTGAAAATTTGCCGCCGCCATCCCACGCAACtt
Rod3_166	AATCATTGTCGGTGGTAGCAGTTGGGCGGTTGCAGAAAC
Rod3_167_4T	TTCGCTATAAACTTAAATTTCTtttt
Rod3_168_4T	CAACATGTAGCCAGCAGACTCCTTTGGGAAGGGCGATCGGtttt
Rod3_169_4T	TTCATTTGAGGCCGGAGAATTAGAATTTAGACGCAATAATAACGGAATACCCAtttt

Rod3_170	ATTATCATTTTGCGGCATCATATCCACCAGACATTAGCAGGGCGCGA
Rod3_171	AGTTTTGTGCGGCCAGCAGCGGGGTCATTGCACAGCACCGTGAATTA
Rod3_172	TATAACGTACAGGAGGTATTAAGAGCATTGACGAGTAGTA
Rod3_173_4T	ttttGGAGCTAAGCTTTCCTAAGAGAAGGATTAGGACATTCCAC
Rod3_174_3TT	ttttAGGAGCGGAATTATAACAAAGACGCCGCCAGGCTGAGACGATCTAAAGACAGCCt
Rod3_175	CAGAGCCGTCCTGATTAACGCTCAACAGTAGG
Rod3_176_4T_Cy5	**ttttCCATATTTAACAACGCGCTTAATTACCATTAC**
Rod3_177_add_4T2	ttttATATATTCATTAATGAATCGGttttCCAACGCGCGGGG
Rod3_178_add_4T3	ttttGCGTCAATTCtttttttTTCTAGCTGAAtttt
Rod3_179_add_4T2	TCAAAAATTGGCCTTCTTCAACCGttttAGCAAGCCTTTtttt
Rod3_180_add_4T3	ttttTCACATAACCGttttTGAAATGGAAACCGTCTATCAtttt
Rod3_181_add_4T2	CGATTTTTTGTTTttttAACGTCAAAAATGCGAGAACAtttt
Rod3_182_add_4T2	CAATCGTCtttttttGGGCGATGGCCCA

Underlined, BG-conjugated; bold (176), fluorescence dye-conjugated. This information was kindly provided by Prof. Hisashi Tadakuma.

Supplementary Table 6 | Sequences of modified staples for 28HB rods

Pos	Name	Sequence ("*" denotes the modification such as NH2 or C6dT)
1	Rod3_025_5L-NdT3_T30	*T*T*ttttttttttttttttttttttttttttttGCAGCGAATCACATTAGGCAACAGCTGATTGCTTG AGTGAGAGATAG
2	Rod3_029_5L-NdT3_T30	*T*T*ttttttttttttttttttttttttttttttGGTCATTGAGAGGAAGTCATTTTTGCGGATGG
3	Rod3_040_3L-NdT3_T30	AATGAGTGAGCTAACAGACAGCATCGGAttttttttttttttttttttttttttttt*T*T*
4	Rod3_045_3L-NdT3_T30	GGAATCGTGCATCAAAAAGATTACCTGAGAGTCTGttttttttttttttttttttttttttttt*T*T*
5	Rod3_123_3L-NdT3_T30	GACGTTGGTAACAAAGTGAGCCGGCTGCATCAttttttttttttttttttttttttttttt*T*T*
6	Rod3_126_3L-NdT3_T30	AAAAGAAAGCACCGCTTCTGGTGAGGGTTTTATAGACTTttttttttttttttttttttttttttttt *T*T*
7	Rod3_141_3L-NdT3_T30	CTTCGCGTCCGTGAGCAGCGCAGTGTCACttttttttttttttttttttttttttttt*T*T*
8	Rod3_146_3L-NdT3_T30	GAACTGGCAGCAACCGAAAAATCCCGTAAAAAGTGAAGGGATAGttttttttttttttt tttttttttttttt*T*T*
Cy3	Rod3_176_4T_ Cy3	*ttttCCATATTTAACAACGCGCTTAATTACCATTAC

This information was kindly provided by Prof. Hisashi Tadakuma.

Supplementary Table 7 | Sequences of modified staples for 42HB bricks

ID *1	Staple # *2	Sequence	Coordinate *3	Position	# of dB *4			
					1	2	4	8
1	5	[5'dB]TTTTTAACTTTGTATCACCGTA	4[149]	Top Back				○
2	7	[5'dB]TTTTCAGCGGAGTGAGTTAATCTCCTTAAGACAGTTTTAGACTCCT	0[56]	Top Front				○
3	31	[5'dB]TTCAGGCTGCTTGCCAGGGTTTTCCCAGTCTTGAACGTTATT	29[89]	Left Bottom				○
4	32	[5'dB]TTCACTGCCCGCTTTCCATTCTGAAAGT	37[56]	Bottom Front			○	○
5	50	[5'dB]TGAACGTGGCGAGAAAGGATTACGCTGCTTCATATTCTTTCAACAGTTATAACCTTTCATAGCGT	41[150]	Bottom Back				○
6	59	[5'dB]TGGCAAAATTGGAACCGAACTGACCAATTATCACCGGT	5[59]	Left Top			○	○
7	113	[5'dB]TCATAAAGGTGGCAACATTTAGCGTCTTAAAAAGATTAGAATAAT	12[88]	Right Front	○	○	○	○
8	124	[5'dB]TATTTACATTGGCAGATTTTGCGTATTT	36[152]	Right Back		○	○	○

*1, numbers indicated in Fig. 5.

*2, numbers of staples for the 42HB brick (Gerling et al., 2018).

*3, coordinates for “number of helix bundle [number of nucleic acids]” for the 42HB brick (Gerling et al., 2018).

*4, dB-modified staples used for 42HB bricks with 1, 2, 4, or 8 SA.

This information was kindly provided by Yuxiang Liu.

Supplementary Table 8 | Data collection and image processing in cryo-EM SPA

	42HB bricks only	**42HB-SA +ribosomes, SDG-purified**	**42HB-SA +ribosomes, unpurified**	**42HB(-SA)$_2$ +lysate, SDG-purified**	**42HB(-SA)$_8$ +lysate, SDG-purified**
Additional carbon layer on grids	-	+	+	+	+
Number of micrographs	522	460	828	594	666
Reference 2D class averages for auto-picking	created by manual-picking from the dataset	70S *	70S *	70S *	70S *
Initial model	EMD-4354	created from the dataset	created from the dataset	created from the dataset	created from the dataset
Reconstructed density map	42HB brick	50S	70S	70S	70S
Number of selected particles for 3D classification	14,226	6,992	26,301	2,123	30,200
Number of selected particles for 3D auto-refine	9,201	6,992	13,219	1,685	23,288
Number of selected particles per a micrograph	18	15	16	3	35
Map resolution (Å) (FSC threshold = 0.143)	20.9	8.1	10.0 **	10.7	6.0

*, 2D class averages of the 70S ribosome was created by manual-picking ribosome particles from a dataset of purified ribosomes.

**, low resolution of the unpurified sample may be due to biased orientation of particles.